IntechOpen

Geophysics

Edited by Anthony Okiwelu

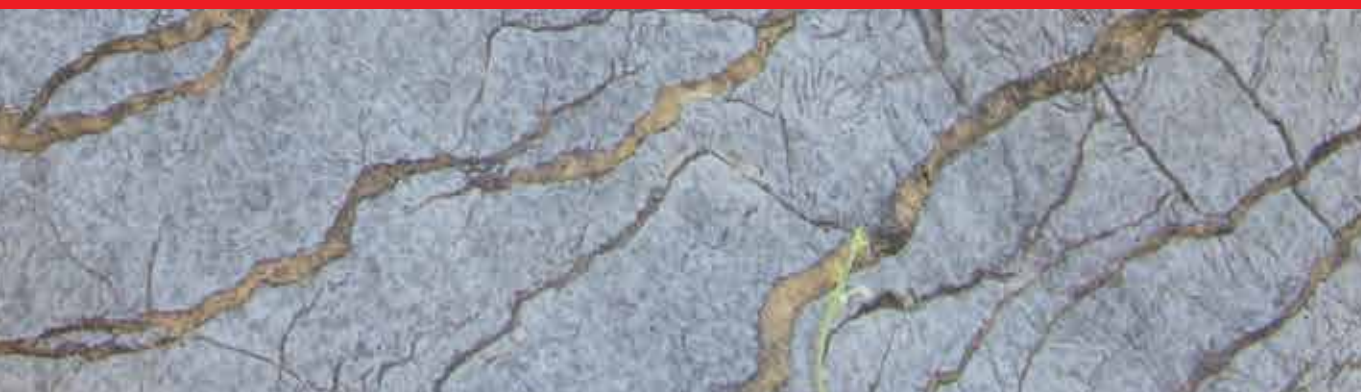

GEOPHYSICS

Edited by **Anthony Okiwelu**

Geophysics
http://dx.doi.org/10.5772/68004
Edited by Anthony Okiwelu

Contributors

Shuang Liu, Xiangyun Hu, Leszek R. Jaroszewicz, Anna Kurzych, Krzysztof Teisseyre, Zbigniew Krajewski, Eneanwan Ekpo, David Eaton, Ronald Weir, Shemer Keydar, Vladimir Shtivelman, Avner Arzi, Omar Delgado-Rodríguez, Vladimir Shevnin, Héctor José Peinado-Guevara, María Ladrón De Guevara Torres, Silvia Garcia, Leonardo Alcántara, Olga Khachay, Yurie Khachay, Alexandr Antipin, Alexis Mojica

Notice

First published in London, United Kingdom, 2018 by IntechOpen
eBook (PDF) Published by IntechOpen, 2019
IntechOpen is the global imprint of INTECHOPEN LIMITED, registered in England and Wales, registration number: 11086078, The Shard, 25th floor, 32 London Bridge Street
London, SE19SG – United Kingdom
Printed in Croatia

British Library Cataloguing-in-Publication Data
A catalogue record for this book is available from the British Library

Additional hard and PDF copies can be obtained from orders@intechopen.com

Geophysics
Edited by Anthony Okiwelu

p. cm.

Print ISBN 978-1-78923-020-8

Online ISBN 978-1-78923-021-5

eBook (PDF) ISBN 978-1-83881-273-7

Meet the author

Dr. Anthony Okiwelu holds a PhD degree in Geophysics from the University of Calabar, Nigeria, and MSc degree in Geophysics and BSc degree in Geology from the Universities of Ibadan and Calabar, respectively. His main research interest is in magnetics, gravimetry, and tectonics. He has also published some papers in geodesy, geopotential field models, and seismic and electrical methods. He is a professor of Geophysics in Geophysics Unit, Physics Department, University of Calabar, Nigeria, where he teaches magnetic prospecting, gravimetry, geomathematics, and Earth Physics. He is an active member of International body, Society of Exploration Geophysicists (SEG), Nigerian Institute of Physics (NIP), and Nigerian Mining and Geoscience Society (NMGS).

Contents

Preface

This book is focused on different aspects of geophysical research, particularly on modern approach in subsurface imaging, tectonics, geohazard, seismicity, and Earth planetary system. Syntheses of results from regional and local studies combined with new techniques of geophysical data acquisition and interpretation from diverse geological provinces are presented.

The first group of chapters is dedicated to seismic and potential field methods. S. Keyder used seismic diffracted (scattered) waves to locate near-surface sources in Israel. Diffracted waves are usually considered as noise in seismic exploration. This imaging technique could be a 3D volume in which prominent diffraction anomalies appear at spatial locations close to the imaged source. The fundamental concept of this study is based on spatial summation of diffracted wave field along diffracted time surfaces, which is defined by source-receiver geometry in 2D or 3D space. This method which reveals localized inhomogeneities has application in engineering, environment, and archeogeophysics. The authors tested this technique with both synthetic and field data. The synthetic examples demonstrated the application of the method to locate both small quasi-isometric source such as small karstic cavity and a linear elongated source such as tunnel/tube. Field examples in this study are from the Dead Sea, Chalky Hills (23km east of Mediterranean Sea), modern operating aqueduct and limestone quarry. The field datasets revealed the depths to the local sources.

R. Leszek and others in their chapter presented the fundamental requirements in the area of rotational seismology. They defined rotation in this context as displacement of rocks, soils, and various objects during earthquake in the focal area and its vicinity. Reversible rotational oscillations in the seismic wave field are called seismic rotations. In seismological perspective, it is an area of a rotational seismology, which deals with all aspects of a rotational ground motion induced by earthquakes, explosions, and ambient vibrations. This field of study is very interesting for researchers from a wide range of geophysical disciplines, including broadband seismology, strong-motion seismology, earthquake physics, seismic hazards, seismotectonics, and geodesy and for physicists using Earth-based observatories for detecting gravitational waves generated by astronomical sources. In addition, it is interesting for researchers of earthquake engineering, where seismic signals of different engineering structures are investigated, to search for their optimal seismic design. This chapter gave vivid illustrations of modern seismometers for the study of rotational seismics and compared the results obtained from optical and mechanical rotational seismometers. It was concluded that technologies based on optical interferometer are the most promising ones.

One of the chapters by Liu and Hu specifically explained how remanent magnetization and self-demagnetization complicate the inversion and interpretation of magnetic anomaly. They used both synthetic data and field data from iron deposit in South Australia to demon-

strate that intensity and direction of internal magnetization can be distorted by remanence. In this study, the primary advantage magnitude of magnetic anomaly inversion is that the magnetization is not assumed to be parallel to the magnetic field. 2D magnetic anomaly was computed in the frequency domain and related to magnetization direction and shape of magnetic sources.

Another chapter by Ekpo and others is very interesting and comprehensive in the sense that the chapter used integrated methods in geophysics. Using regional gravity and magnetic datasets combined with Lithoprobe crustal seismic profile and well data, they investigated basement tectonics and crustal structure in Alberta, western Canada. The Precambrian basement beneath Alberta was formed by amalgamation of disparate domains that were assembled by the plate-tectonic processes of subduction. Basement domains that are the focus of this study occurred between the Snowbird Tectonic Zone (STZ) and Great Slave Lake Shear Zone (GSL_s Z) and have Paleoproterozoic crystallization ages (1.9–2.4 GA). This area is prone to induced seismicity, and brittle faults are poorly imaged by seismic data due to obscuring effects of multiple. Thus, the use of potential-field fabrics was able to establish the tectonic setting of basement domains with additional information provided by magnetic, Bouguer, and isostatic residual anomalies based on 2D modeling constrained by seismic profiles. The main objective of this study is to present new insights arising from geophysical imaging and mapping of representative basement fault structure and how they may lead to the understanding of induced seismicity. To achieve this objective, the authors used the interpretation approach, which involves mapping and identification of basement structures combined with 2D gravity and magnetic modeling for selected profiles. The analyses showed that regional gravity anomaly patterns clearly revealed large-scale crustal features. An example is a Bouguer gravity low that marks the isostatic root beneath the Rocky Mountains, an isostatic gravity high that reflects a flexurally supported topographic load in the Rock Mountain frost ranges of Alberta and NE-SW linear fabrics associated with the Snowbird Tectonic Zone (STZ). The result of this study also demonstrated that magnetic anomaly map can provide a method for delimiting the extent of basement tectonic domain. While the magnetic anomalies predominantly reflect the magnetic susceptibility of the upper basement due to the wavelength differences, the gravity anomalies are primarily sensitive to deeper crustal level.

Two chapters are devoted to geohazard. The chapter based on the optimal geoelectric methodology (OGEOMET) written by O. Delgado-Rodríguez as the lead author integrated geoelectric methods to investigate hydrocarbon-contaminated sites in Mexico. The electromagnetic profiling provided a reliable and fast method that unraveled the configuration of oil-contaminated plume from apparent resistivity map and was used to guide the subsequent electrical resistivity tomography survey. Electrical resistivity tomography (ERT) and electromagnetic profiling (EMP) methods were used for the delimitation of the resistivity anomalies caused by different types of hydrocarbon contaminants and rocks in rural, industrial, and urban sites. Another method used in this study includes the use of petrophysical model. In the laboratory, the behavior of soil resistivity versus water salinity in clean soil samples is measured, and clay content, porosity, and cation exchange capacity (CEC) were determined. The knowledge of these petrophysical parameters was used to define the geoelectric boundary between contaminated and clean zones. This chapter revealed the migration pathways of contaminants and located the sources of contaminants and the

vulnerability of the aquifers in the study areas. One of the highlights of this study is that the OGEOMET reduced the number of drillings and soil samples for chemical analyses.

The next chapter on geohazard based on seismic response in Mexico was written by S. Garcia and L. Alcantara. In this study, they used Hilbert-Huang transform (HHT) as an alternative technique, which has advantage over other methods for extracting data that will be useful for the assessment of potential earthquake and, if integrated with the empirical mode decomposition (EMD) and the Hilbert transform (HT), enables engineers to analyze data from nonlinear and nonstationary processes. The HHT proposed by Huang and others consists of two parts: (i) Empirical Mode Decomposition (EMD), and (ii) Hilbert spectral analysis. Signals to be analyzed are decomposed into a finite number of intrinsic mode functions or IMFs in what is called the EMD process. The Hilbert transform allows the computation of instantaneous frequencies and amplitudes and describes the signal more locally.

The two authors demonstrated that the use of Fourier spectral analysis for studying nonstationary-nonlinear data is not a robust tool for these kinds of analyses since it cannot show the detailed information about the peculiarities of the energy-frequency distribution. By using Hilbert spectra, events in the database will have direct important characteristics such as the arrival time, and the duration of intense phase of the earthquakes can be detected. In addition to the well-defined zone of maximum accelerations, the huge variations of the response frequencies between the beginning (the maximum amplitude cycles) and the end of the event can be clearly detected and quantified. The Hilbert spectral transformation permits the recognition of oscillation modes that would have been masked by Fourier spectral analysis.

Y. Khachay and his colleagues presented the results of a numerical simulation of the thermal evolution of a 3D spherical segment of a protoplanet of an increasing radius, taking into account the accidental falling of bodies and particles. Some new questions were raised such as what is beyond the boundaries of our universe? Is the universe only one? Are there any measurable physical fields and processes that will allow one to detect real objects external to our universe? They employed algorithm for the numerical solution of the problem considering the dissipation of tidal energy in the Earth-Moon system at the stage of planetary accumulation. The study noted that at all stages of the Earth's formation, convective heat and mass transfer are the most important factors in the dynamics of the planet. Their result shows that the temperature of the growing surface sharply decreases as the transparency of the atmosphere increases, due to the increase of the gravitational radius of the protoplanet and the possibility of retaining the silicate content of the cloud. The following conclusions could be derived from this study: (1) As the mass increases, the distance between their centers of mass and the speed of the orbital rotation of the Moon around the Earth change. From the law of conservation of angular momentum, it follows that the tidal interaction as the mass of the central body increases provides the transfer of the orbital angular momentum of the satellite to the central massive body. (2) Due to the continued transfer of the satellite's orbital moment to the central body, its own angular velocity continued to grow. This should lead to an increase in the orbital angular velocity of the satellite and an increase in the radius of its orbit, which is observed up to the present time. (3) The results obtained depend on the parameters, primarily the viscosity versus temperature and pressure, the values of which are known with a high degree of uncertainty.

A. Mojica, in the chapter on electrical resistivity surveying, gave a short description of electrical properties of rocks and basic principles of the geoelectrical resistivity. He used electri-

cal resistivity method to define 1D and 2D electrical models from two datasets acquired in dry and rainy seasons in Panama (Central America). The results obtained enabled him to monitor the percentage changes of calculated resistivity values and define the stratigraphy of the area of study. He also obtained a relationship between electrical resistivity and volumetric water content and correlated this with empirical equation of Archie. Petrophysical analyses show good fits between resistivity and volumetric water content and known parameters for rocks and soils. Mojica used the Res2Dinv inversion software (Geotomo) to estimate the changes in subsurface resistivity values during the period of monitoring. In this software, the initial dataset for the inversion model is used as a reference model in the inversion of the later time-lapse datasets. The result of the electrical sounding tied to the well data at the site showed that the two first layers are linked to weathered and fractured sedimentary rock, while the last layer is linked to hard sedimentary rock. The result of the electrical resistivity imaging and time lapse revealed high negative percentage change, which is linked to increase of water content in subsoil produced by rains that occurred on May 31, 2012, while positive percentage changes in model resistivity are related to inversion artifacts. He concluded that these unrealistic changes can be linked to the removal electrode after the first test or inversion scheme used in the analyses.

Anthony Okiwelu
Department of Physics
University of Calabar, Nigeria

Section 1

Seismic and Potential Field Methods

Chapter 1

Three–Dimensional Seismic Diffraction Imaging for Detecting Near-Surface Inhomogeneities

Shemer Keydar, Vladimir Shtivelman and Avner Arzi

Additional information is available at the end of the chapter

http://dx.doi.org/10.5772/intechopen.74059

Abstract

One of the problems encountered in a variety of near-surface investigations is detecting and mapping localized inhomogeneities. Typical examples of such inhomogeneous sources are cavities, caves and tunnels. Different methods for detecting shallow subsurface sources utilizing seismic waves diffracted by these sources were proposed by many researchers in the last three decades. Most of these methods suggest that every subsurface point is a possible location of a point diffractor. Imaging of the diffractors is based on a spatial summation of the diffracted wavefield along diffraction time surfaces (defined by source-receiver geometry) in 2D or 3D space. The summation is performed with a fixed velocity value estimated from velocity analysis of the diffraction data. In this study, we present a path integral summation approach, where for every subsurface point the wavefield is stacked together along all possible diffraction time surfaces having a common apex at a given time. The result of the imaging is a 3D volume in which prominent diffraction anomalies appear at spatial locations close to the imaged sources. This path integral summation approach has been successfully tested on synthetic data and further applied at several sites with known subsurface sources.

Keywords: near surface, inhomogeneities, diffraction imaging, path integral summation, seismic

1. Introduction

The problem of detecting localized near-surface inhomogeneities is encountered in a variety of applications, such as engineering site investigation, environmental studies, archeology and security problems. Typical examples of such sources of inhomogeneities are cavities, caves and tunnels and other natural and man-made local inhomogeneities.

In the past decades, many attempts have been made to solve the problem using various geophysical methods. The methods in use can be roughly subdivided into two groups. The first group includes low-resolution bulk techniques such as microgravity, geoelectric method and seismic surface wave method. A typical drawback of these methods is their low detectability, limiting them to relatively large sources, that is, such sources whose dimension-to-depth ratio exceeds 1/2 [1–4]. The second group includes the high-resolution ground – penetrating radar (GPR) method. The main drawback of this method is its high sensitivity to electrical conductivity of near-surface material which makes it limited to very shallow depths usually not exceeding a number of meters. Furthermore, our experience shows that the general problem of all the existing techniques is a high degree of ambiguity of data interpretation and, as a result, a high percentage of errors. One of the methods that may prove very effective for this purpose is active seismic, which is widely employed by seismic exploration industry in its extensive and detailed studies of the subsurface. Adaptation of these methods for the purpose of searching for local underground heterogeneities is not an easy task. The primary aim of seismic exploration is to study geological sources of large lateral extent, such as boundaries of geologic formations, oil and gas deposits, etc. To this end, seismic exploration ("reflection seismic") utilizes seismic waves emitted from man-made (active) seismic sources and reflected from the boundaries of interest back to the surface. The methodology, the data acquisition and processing techniques employed by the reflection seismic are largely based on the model of the subsurface consisting of a number of layers divided by smooth curvilinear boundaries with gradual changes of parameters within layers. Virtually, the same model of the subsurface is behind the refraction seismic method, another technology used primarily to study the shallow part of the subsurface (first tens of meters). Clearly, such methods are not directly applicable to a search for local subsurface inhomogeneities of small lateral extent (10–100 m). The amount of energy reflected by such small sources would be very small, and it would be indistinguishable from other geological features of the subsurface. In order to be effective, the search for local inhomogeneities has been employed to image the features of seismic wavefield, which is primarily associated with the presence of local heterogeneity in the subsurface. Such features are known as scattered (diffracted) waves. In a standard seismic prospecting, these waves are usually treated as noise. But for locating local sources these waves provide the most valuable source of information [5–12].

2. Methods for locating subsurface heterogeneities

2.1. Wavefield

Let us look at the resulting wavefield obtained from a typical underground heterogeneity in a typical layered geological environment. The wavefield could be divided into a number of different kinds of waves such as primary and multiple reflected waves, refracted waves and scattered/diffracted waves. The reflected waves originate from the layered boundaries, the refracted waves from boundaries of high contrast while the scattered/diffracted waves are generated by local heterogeneities. The reflected and refracted wavefields would only slightly be affected by the presence of the local heterogeneities. However, since the scattered/diffracted waves are generated by local heterogeneities, they may be used for the imaging of those heterogeneities.

http://dx.doi.org/10.5772/intechopen.74059

2.2. Diffraction imaging

Imaging of the local heterogeneities in 3D space can be performed by a spatial summation of scattered/diffracted waves along the travel-time surfaces of those waves [9].

The summation can be implemented using one of the two approaches. In the first step (conventional approach), target waves are stacked along the time surfaces defined by some "optimal" velocity values. These values are usually estimated by a time-consuming procedure of velocity analysis involving visual examination and interpretation of intermediate seismic images. Recently, an alternative method, a more formal, path integral summation approach, has been proposed [7, 10–12]. Path integral summation is performed by stacking the target waves along all possible time surfaces having a common apex at the given point. This approach does not require any explicit information on velocities since the required multipath summation is performed for all possible velocity values within a wide specified range. Application of the path integral summation to synthetic and real data shows that it can provide reliable images of subsurface objects close to their true spatial locations [9]. However, the spatial resolution of the images obtained by the path integral summation is usually inferior to those obtained using the fixed velocity.

In the subsequent sections, we give a brief description of the main principles of the method and illustrate its application by two synthetic examples. Then, we present four case studies demonstrating how the method can be implemented for detecting various subsurface objects located in different geological environments.

2.3. Theoretical background

The method suggests that every subsurface point is a possible location of a point diffractor. Imaging of the diffractors is based on a spatial summation of the diffracted wavefield along diffraction time surfaces (defined by source-receiver geometry) in 3D space. The result of the imaging is a 3D volume in which prominent diffraction anomalies appear at spatial locations close to the imaged objects. The proposed method proved to be a robust high-resolution technique capable of providing reliable results under various geological conditions in a wide range of depths. The method seems to be especially suitable for detecting relatively small objects.

The proposed method is based on a spatial summation of diffracted waves in 3D space. The principles of the method can be elucidated using a simple scheme represented in **Figure 1**. Assume that a source of seismic energy is located at the point (X_S, Y_S, Z_S) and that there is a diffractor (i.e., a void) at the point (X_D, Y_D, Z_D) within a homogeneous medium with a velocity V. When seismic waves generated by the source reach the diffractor, it starts to operate as a secondary source generating diffracted waves. At a certain time the diffracted wave arrives at a receiver located at the point (X_R, Y_R, Z_R). For the given source-receiver pair and a fixed diffractor position, the arrival time can be represented as a sum of two terms: source-to-diffractor time and diffractor-to-receiver time. In a homogeneous medium, this sum is totally defined by spatial coordinates of the source, receiver and diffractor and the velocity in the medium. Assuming that the source and receiver are located at the surface Z = 0 (i.e., $Z_S = Z_R = 0$), the arrival time of the diffracted wave can be defined as follows [9]:

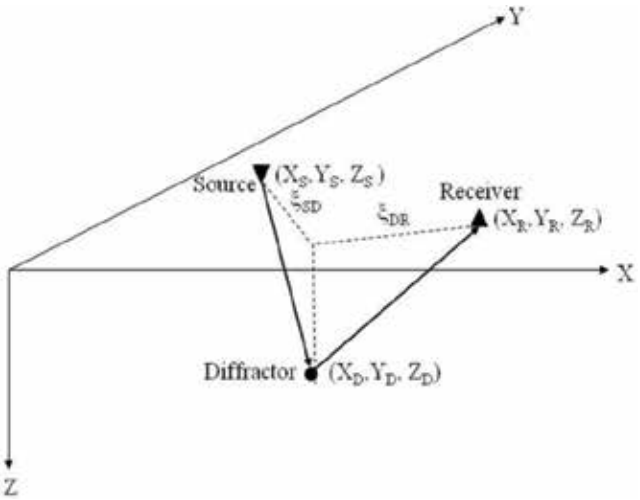

Figure 1. Schematic illustration of basic diffraction geometry.

$$T_{SR} = \sqrt{(\xi_{SD}/V)^2 + T_D{}^2} + \sqrt{(\xi_{DR}/V)^2 + T_D{}^2}, \tag{1}$$

where $\xi_{SD} = \sqrt{(X_D - X_S)^2 + (Y_D - Y_S)^2}$ is the horizontal source-to-diffractor distance; $\xi_{DR} = \sqrt{(X_R - X_D)^2 + (Y_R - Y_D)^2}$ is the horizontal diffractor-to-receiver distance; $T_D = Z_D/V$ is vertical time above the diffractor; and V is the velocity in the medium. The velocity defines the shape of the diffraction time surface, whereas time T_D defines its apex. For a spatial array of receivers, equation (1) defines a diffraction time surface with its apex at time $2T_D$. If the velocity in the medium is known, the diffractor can be imaged by summing seismic energy arriving at different receivers along the time surface defined by equation (1). The principles of the imaging can be formulated as follows:

- A targeted source (a void) acts as a secondary source of waves (diffracted waves).
- Every point in the subsurface is considered as a possible diffractor.
- Seismic data acquisition is performed by a 3D survey involving a large amount of source and receiver points.
- The imaging is based on a spatial summation of diffracted waves arriving at all the receivers from all the sources.
- The summation is performed using Eq. (1) with a fixed velocity value estimated from velocity analysis of the diffraction data.
- Alternatively, it can be done using a path integral summation approach, where for every subsurface point, the wavefield is stacked together along all possible diffraction time surfaces having a common apex at a given time [10].
- The result is a 3D image of the subsurface (a 3D volume) where the diffractor (the void) appears as a distinct anomaly.

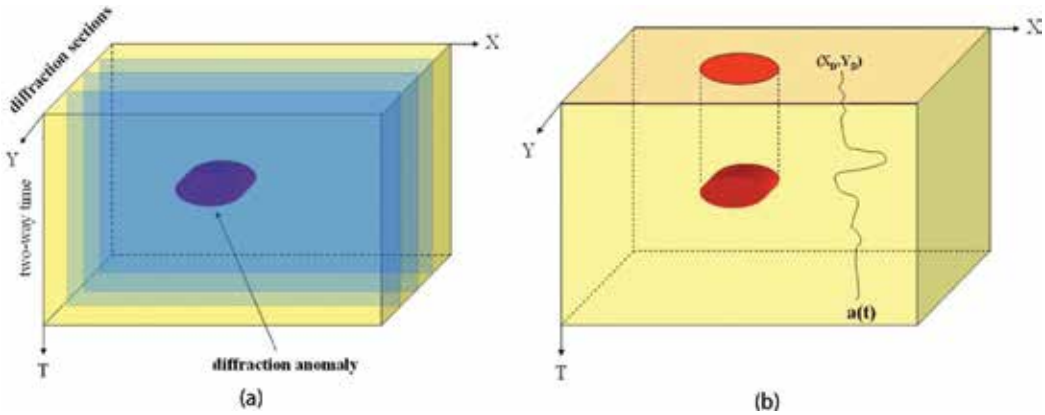

Figure 2. (a) Schematic illustration of a 3D volume and D-sections in X-T plane and (b) schematic illustration of D-map in X-Y plane.

Figure 2a is a schematic illustration of a 3D volume containing a diffraction anomaly obtained by the imaging. Note that the vertical axis is two-way time rather than depth, since the imaging is performed in the time domain. Subsequently, the results of the imaging will be presented in two forms. The first one is obtained by vertical slicing of the 3D volume parallel to the X axis, as illustrated by **Figure 2a**. In this manner, we obtain a set of vertical diffraction sections computed for a number of Y values and represented in the X-T plane (we call them D-sections). The second form is obtained as follows (**Figure 2b**): for every output trace $a(t)$ resulting from the spatial summation of the corresponding input traces, we compute its energy by summing squared values of the trace amplitudes and put the resulting sum at the corresponding trace location (X_D,Y_D) at the surface. In such a manner we obtain a map of trace energy (we will call it D-map) on which the diffraction anomaly is represented by its horizontal projection onto the X-Y plane, as illustrated by **Figure 2b**.

As mentioned above, the imaging can be performed using either a fixed velocity or path integral approach. The path integral imaging was described and applied in our previous work [9]. In this work we applied the fixed velocity imaging (which usually provides a better resolution).

3. Synthetic examples

3.1. Point and linear diffractors

The synthetic examples presented below illustrate application of the method for imaging two kinds of objects: a point diffractor (which can be considered as approximation of a small quasi-isometric source, such as a small karstic cavity) and a linear diffractor (roughly approximating an elongated source, such as a tube or a tunnel).

3.1.1. Point diffractor

The model in the first example includes a point diffractor located at a point with the coordinates X = 40 m, Y = 10 m and Z = 10 m. The medium is assumed to be homogeneous with the velocity of 1000 m/s. The modeling was performed using a simulated acquisition system represented in **Figure 3**. The system included 2 receiver lines with 48 receivers on each line and 5 source lines with 48 source points on each line. The source and receiver spacing along the lines (i.e., in the X direction) was 2.5 m. The distance between the source lines was 5 m and between the receiver lines 20 m, so that the area covered by the system was about 120 m × 20 m. Using this system, synthetic seismograms of diffracted waves were computed for each source position, given the total of 240

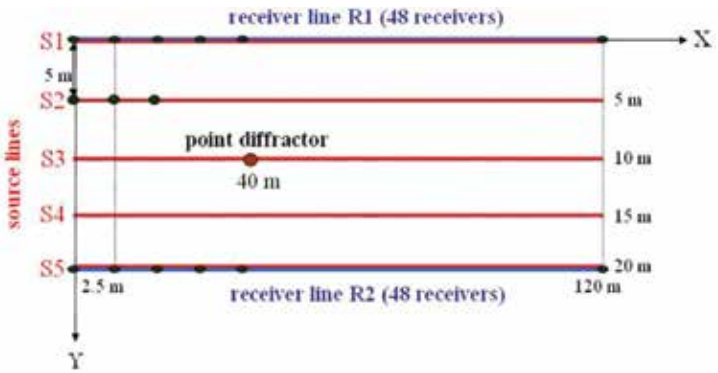

Figure 3. Source-receiver geometry used for a point diffractor modeling (plan view).

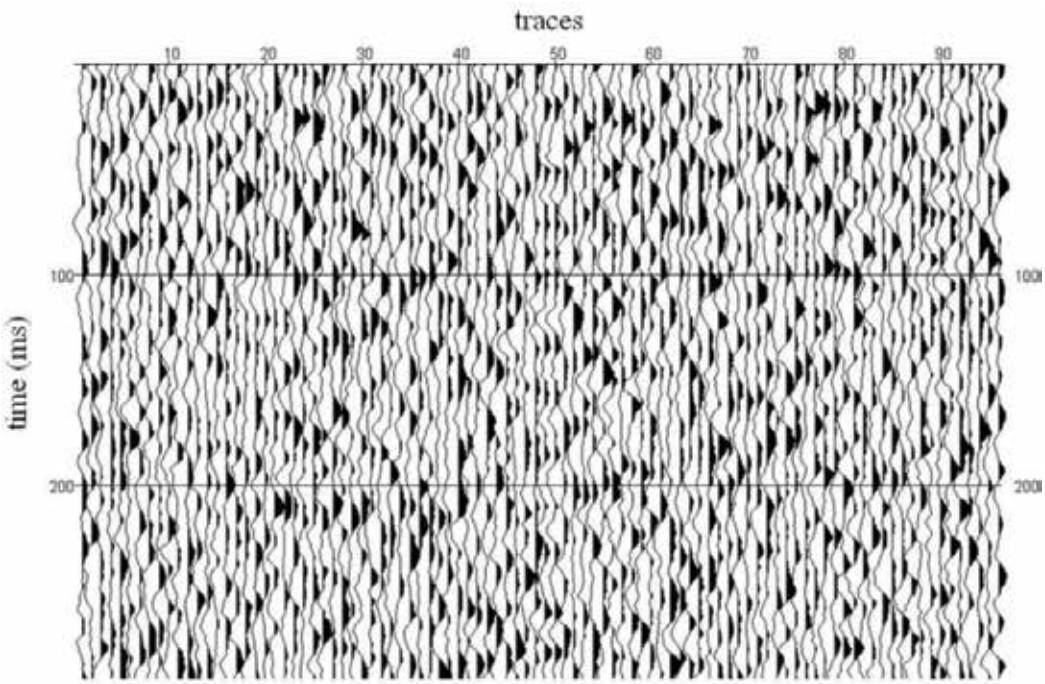

Figure 4. Point diffractor model: an example of a synthetic record.

shot records with 48 traces in each record. Then, a spatially uncorrelated random noise with the average s/n ratio of 0.03 was added to the seismograms. **Figure 4** represents an example of one of the records. Due to the low s/n ratio, no traces of diffracted events were identified on the record.

Figure 5a and **b** represents the results of the point diffractor imaging with the velocity of 1000 m/s. **Figure 5a** shows 5 D-sections computed along the lines defined by the Y values of 0. 5, 10, 15, and 20 m. The sections display a well-defined anomaly whose maximum is located

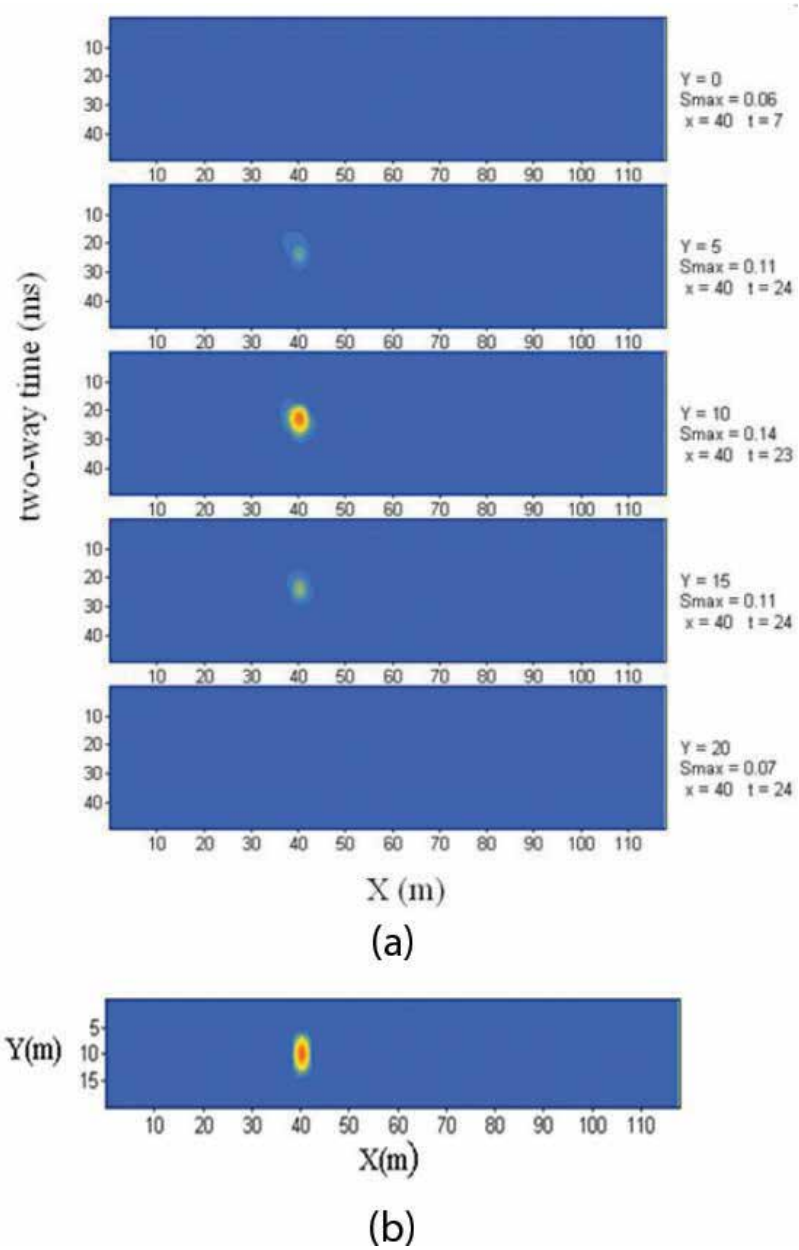

Figure 5. (a) Point diffractor model: D-sections and (b) point diffractor model: D-map.

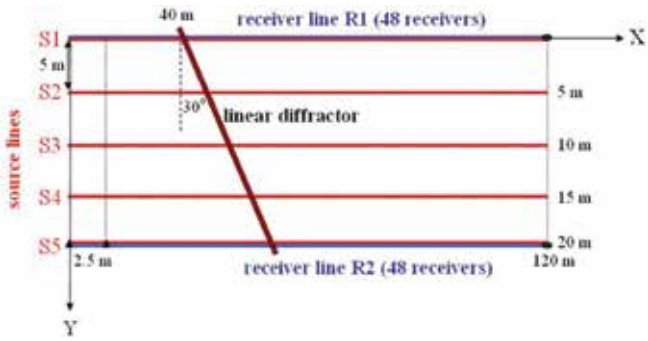

Figure 6. Source-receiver geometry used for linear diffractor imaging (plan view).

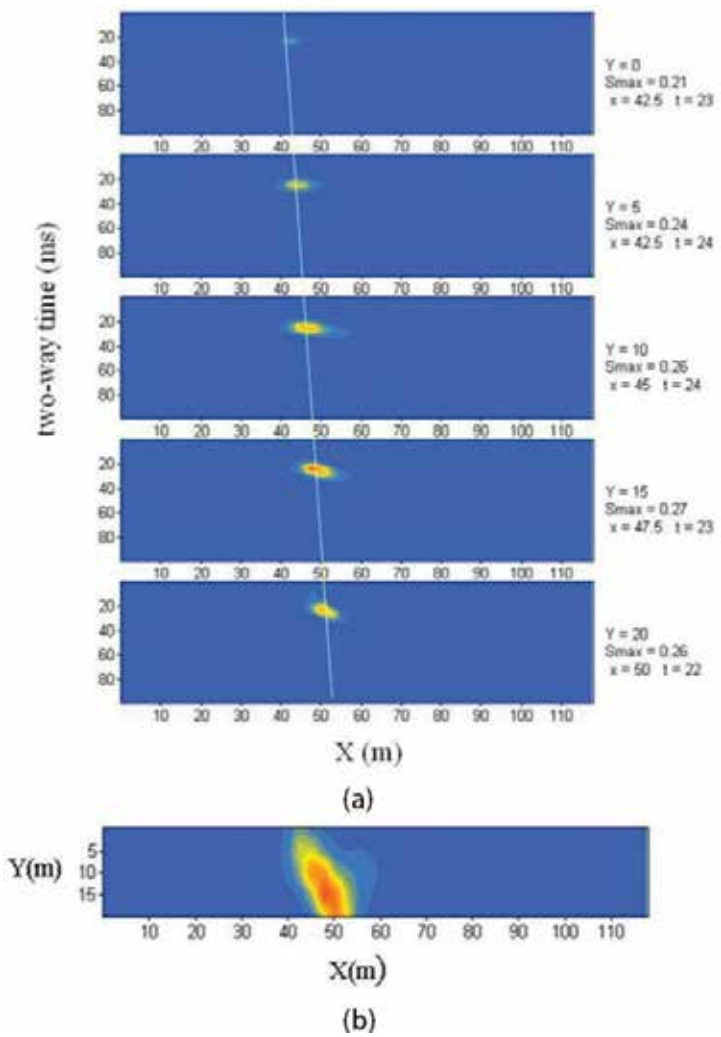

Figure 7. (a) Linear diffractor model: D-sections and (b) linear diffractor model: D-map.

at X = 40 m on the section with Y = 10 m. The amplitude of the anomaly is rapidly attenuated away from its maximum in both the X and Y directions. This can be seen even more clearly on the D-map (**Figure 5b**): the figure shows that the diffraction anomaly is very well localized on the X-Y plane around the imaged point diffractor.

3.1.2. Linear diffractor

The model in the second synthetic example contains a linear diffractor (which can be considered as a set of densely spaced point diffractors). The diffractor crosses the X axis at the distance of 40 m from the origin at the angle of 30° (**Figure 6**). The model parameters and the acquisition system were the same as in the previous example.

The D-sections obtained for this model with the velocity of 1000 m/s (**Figure 7a**) display a well-defined anomaly whose location on the sections varies along the Y axis in accordance with the inclination of the imaged linear diffractor. This is further illustrated by the D-map (**Figure 7b**). The map shows a prolongated quasi-linear anomaly whose location and inclination on the X-Y plane correspond well with the imaged linear diffractor.

4. Case studies

4.1. Dead Sea-Israel

The first case is from a sinkhole site located in the Dead Sea area of Israel. A well drilled at the site revealed a water-filled cavity located in a salt layer within the depth of 22–28 m. The cavity was a target of the diffraction survey carried out at the site. The acquisition system used in the survey was similar to that described in the earlier synthetic examples. Imaging was performed with the velocity of 1200 m/s estimated from the velocity analysis of the data. The resulting D-sections (**Figure 8a**) show a prominent anomaly located in the area close to the well location. The depth of the anomaly was estimated to be about 25 m which is quite close to the depth of the cavity as revealed in the well. The D-map (**Figure 8b**) displays an isometric anomaly implying that the cavity might have a quasi-spherical shape.

4.2. Limestone quarry

The second case is from a limestone quarry where a number of karstic cavities were revealed by drilling shallow boreholes. The depth of the cavities varied between 8 and 23 m. At several sites in the quarry, diffraction surveys were carried out with the aim of detecting the cavities from the surface. We present an example from one of the surveys. The acquisition system used in this case was half as long as the system specified earlier (see **Figure 3**), that is, it included only 24 receivers and 24 source points per line, so that the area covered by the survey was about 60 m × 20 m. The well located near the point (X = 35 m, Y = 10 m) revealed a cavity at the depth of 8 m. Imaging was performed with the velocity of 1500 m/s. The D-sections (**Figure 9a**) show a well-defined anomaly with its maximum located very close to the well location. The amplitude of the anomaly decreases rapidly away from the maximum. The depth of the anomaly was estimated to be about 7 m. Thus, the estimated spatial location of the target

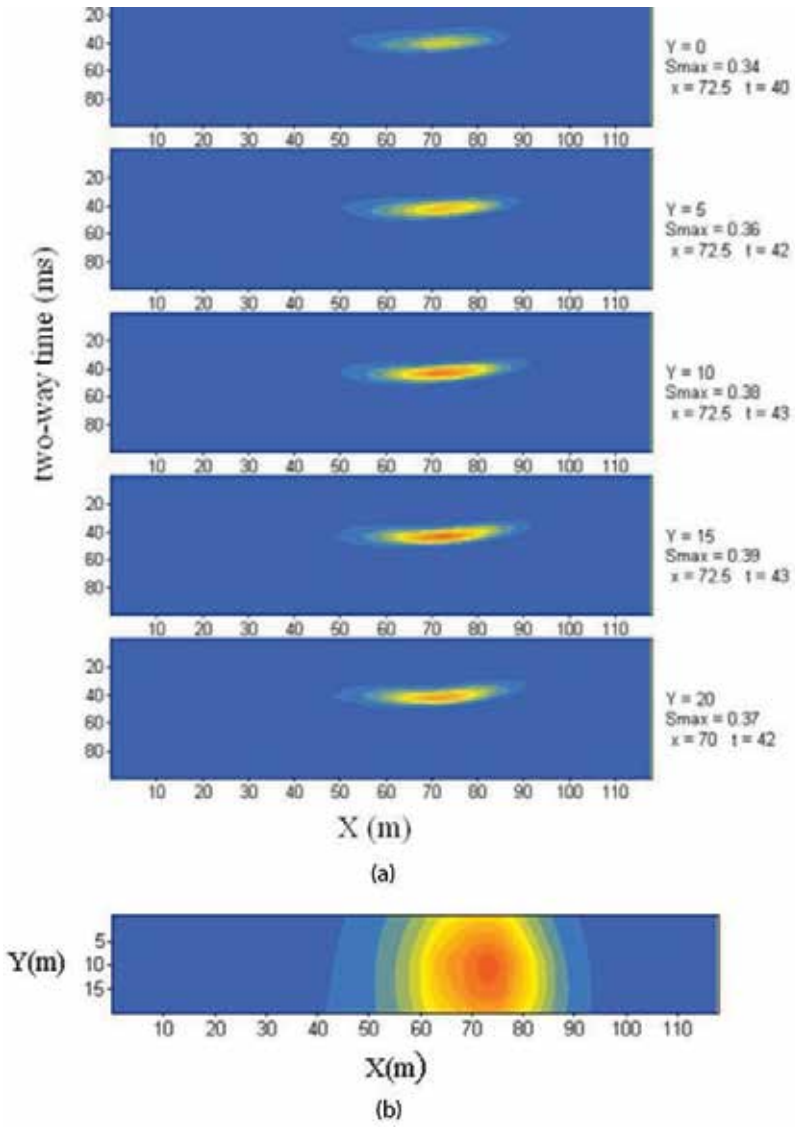

Figure 8. (a) Case 1: D-sections and (b) case 1: D-map.

object is in good agreement with the location of the cavity revealed by drilling. This conclusion is further confirmed by the D-map (**Figure 9b**) that shows an isometric anomaly located in close vicinity around the well.

4.3. Chalky hills

The third case refers to an ancient subsurface aqueduct which has been recently discovered in Chalky hills, some 23 km east of the Mediterranean shore of Israel (**Figure 10a**). The aqueduct was part of a water supply system operating during the Roman and Byzantine

http://dx.doi.org/10.5772/intechopen.74059

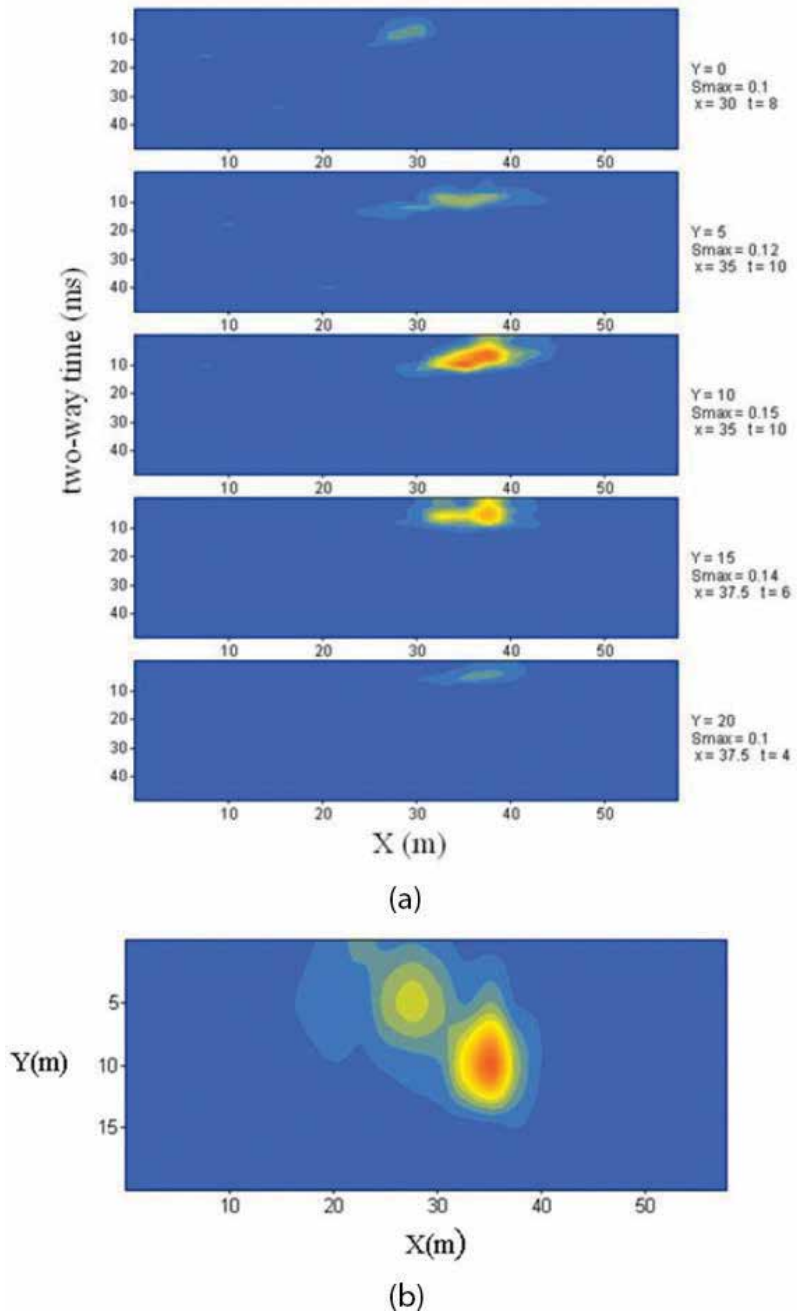

Figure 9. (a) Case 2: D-sections and (b) case 2: D-map.

periods. In the excavated part of the aqueduct, it is about 1.8 m high and 0.8 m wide and its depth from the surface is from 8 to 10 m. A diffraction survey was carried out at the site located above an extension of the aqueduct beyond its excavated part, at the distance

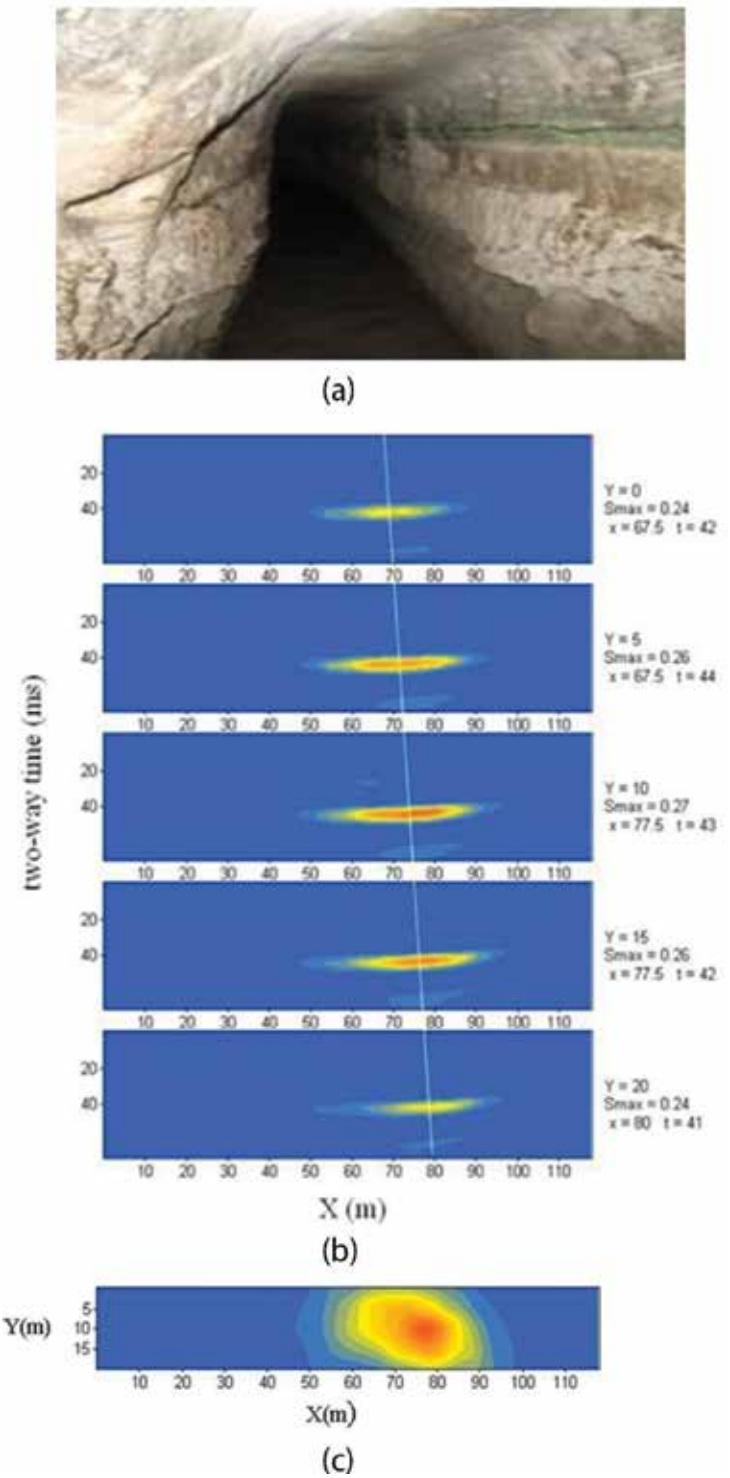

Figure 10. (a) Ancient subsurface aqueduct, (b) case 3: D-sections and (c) case 3: D-map.

http://dx.doi.org/10.5772/intechopen.74059

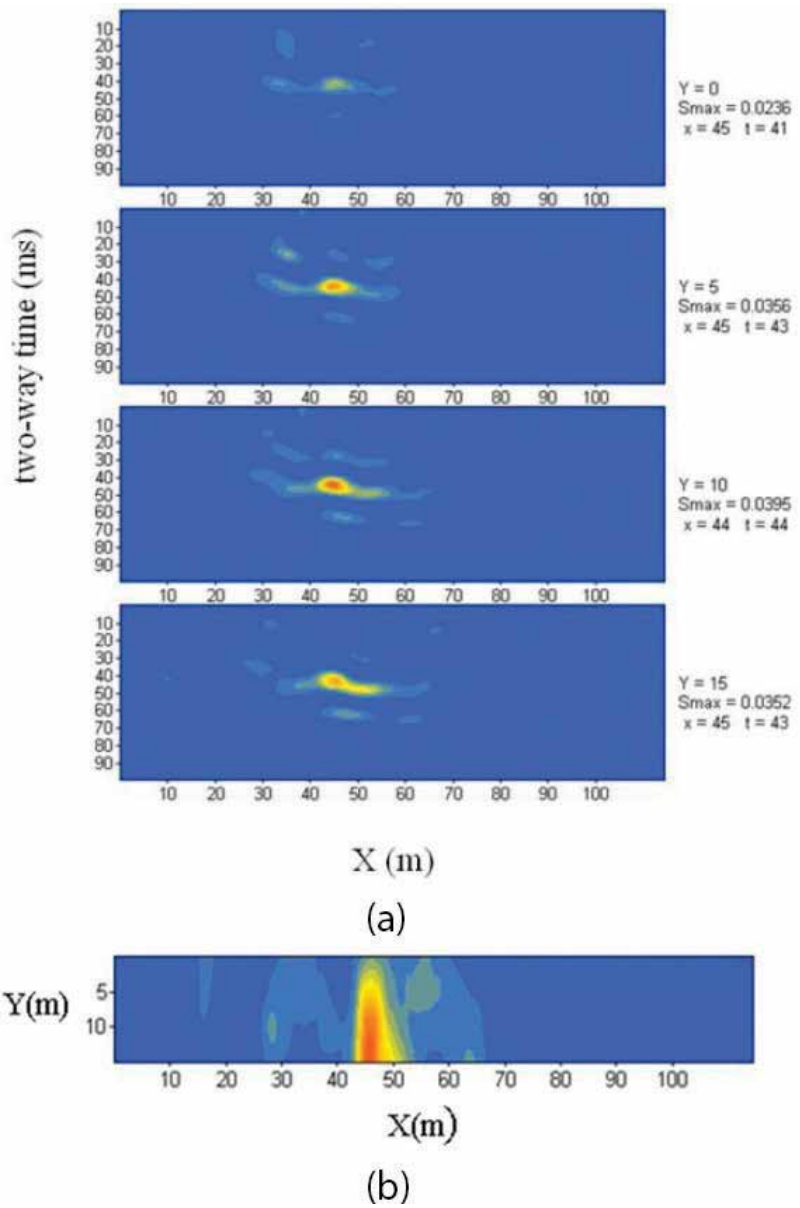

Figure 11. (a) Case 4: D-sections and (b) case 4: D-map.

of about 200 m from the nearest excavated shaft. The acquisition system was similar to that specified in **Figure 3**. The aqueduct was supposed to cross the system at a distance of 80–90 m from the beginning of the lines. Imaging was performed with the velocity of 1200 m/s. The D-sections (**Figure 10b**) show a prominent anomaly located in the area which is close to the estimated extension of the aqueduct. The D-map (**Figure 10c**) displays an elongated anomaly whose inclination on the X-Y plane is in good agreement with the general direction of the aqueduct.

4.4. Modern operating aqueduct

The fourth case is from a site located above a modern operating aqueduct which supplies water to a large part of Israel. The diameter of the aqueduct is 3 m. At the investigated site it is located at the depth of 27 m within the limestone. In this case our target object was quite a small one, since the ratio of its dimension (diameter) to the depth to its center is about 1/10, making it quite challenging.

The diffraction survey carried out at the site used the acquisition system including 2 receiver lines with 24 receivers on each line and 4 source lines with 24 source points on each line. The source spacing was 5 m in both the X and Y directions; the receiver spacing was 5 m in the X direction and 15 m in Y direction. The survey crossed the aqueduct at approximately the right angle at a distance of about 40 m from the beginning of the lines. Imaging was performed with the velocity of 1100 m/s. The D-sections obtained for the data (**Figure 11a**) show a distinct anomaly at X = 45 m. The estimated depth of the anomaly is about 24 m. Thus, the estimated spatial location of the target object corresponds fairly well with the actual location of the aqueduct. This is confirmed by the D-map (**Figure 11b**) which displays a quasi-linear anomaly whose location on the X-Y plane is close to the aqueduct location.

5. Summary

The main points of our work can be summarized as follows: a method for detecting and mapping localized near-surface inhomogeneites was presented.

The method is based on 3D subsurface imaging using spatial summation of diffracted waves along their time surfaces.

The method was successfully tested on synthetic data with a very low s/n ratio.

Application of the method to real data demonstrates that it can provide a reliable detection of relatively small subsurface sources located under different geographical conditions at a wide range of depths.

Acknowledgements

The authors are grateful to the Geophysical Institute of Israel for granting permission to publish the datasets.

Author details

Shemer Keydar[1]*, Vladimir Shtivelman[1] and Avner Arzi[2]

*Address all correspondence to: shemer@gii.co.il

1 Geophysical Institute of Israel, Lod, Israel

2 Geotechnical Consultant, Ramat Gan, Israel

http://dx.doi.org/10.5772/intechopen.74059

References

[1] Debeglia N, Dupont F. Some critical factors for engineering and environmental microgravity investigations. Journal of Applied Geophysics. 2002;**50**(4):435-454

[2] Ezersky M, Goldman M. detection of potentially dangerous subsurface karstic zones using electrical and electromagnetic methods in the Mishor. Rotem Area, Lod: The Geophys. Inst. of Isr; 1999

[3] Shtivelman V. Surface wave secions as a tool for imaging subsurface. European Journal of Environmental and Engineering Geophysics. 2002;**7**:121-138

[4] Militzer W, Rösler H, Lösch R. Theoretical and experimental investigations for cavity research with geoelectrical methods. Geophysical Prospecting. 1979;**27**:640-652

[5] Kanasewich ER, Phadke SM. Imaging discontinuities on seismic sections. Geophysics. 1988;**53**(3):334-345

[6] Keydar S, Pelman D, Ezersky M. Application of seismic diffraction imaging for detecting near-surface inhomogeneities in the Dead Sea area. Journal of Applied Geophysics. 2010;**71**(2-3):47-52

[7] Keydar S, Shtivelman V, Mikenberg M, Moser TJ. 3D prestack time migration by multipath summation. In: 70th European Association of Geoscientists and Engineers Conference and Exhibition 2008: Leveraging Technology. Incorporating SPE EUROPEC 2008. Vol. 5. 2008

[8] Keydar S, Mikenberg M, Shtivelman V, Rochlin I. Imaging shallow linear diffractors by 3D weighted multipath summation. In: 78th EAGE Conference and Exhibition 2016: Efficient Use of Technology—Unlocking Potential. 2016

[9] Shtivelman S, Keydar V. Imaging shallow subsurface inhomogeneities by 3D multipath diffraction summation. First Break. 2005;**23**(January):39-42

[10] Keydar S. Homeomorphic imaging using path integrals. In: 66th EAGE Conference & Exhibition. 2004

[11] Landa E, Fomel S, Moser TJ. Path-integral seismic imaging. Geophysical Prospecting. 2006; **54**(5):491-503

[12] Shtivelman V, Keydar S, Mikenberg M. Imaging near-surface inhomogeneities using weighted multipath summation. Near Surface Geophysics. 2009;**7**(3):171-177

Chapter 2

Measurement of Rotational Events in Regions Prone to Seismicity: A Review

Leszek R. Jaroszewicz, Anna Kurzych,
Krzysztof P. Teisseyre and Zbigniew Krajewski

Additional information is available at the end of the chapter

http://dx.doi.org/10.5772/intechopen.72169

Abstract

On the basis of the explanation of rotational seismology as an area of study, a modern approach to the seismic rotation in various continuum models is summarized. The aim of this chapter is to formulate the fundamental requirements for rotational seismometer. Consequently, a review of all existing technologies of rotational seismometers including mechanical, electrochemical, magnetohydrodynamical, as well as optical type solutions is discussed. The analysis of their parameters that considers technical requirements enforced by rotational seismology has indicated an optical instrument using a Sagnac interferometer as the best solution. Fibre-Optic System for Rotational Events & phenomena Monitoring (FOSREM) with its main parameters and features is described as an example of such solution. Moreover, the example of rotational events recorded in Książ observatory, Poland, using mechanical rotational seismometers and FOSREM is presented. There are data for M = 3.8 earthquake near Jarocin, Poland on the 2012.01.06 at 15:37:56 at a distance of about 200 km from Książ. Although the used devices have totally different designs, the results obtained using FOSREM and the results calculated by mechanical devices show compatibility in rotational signals.

Keywords: theory of rotational events, rotational seismometers, rotational seismic data processing, rotational seismic data acquisition

1. Introduction

Mutual rotation or twisting of monumental blocks around a vertical axis as a result of seismic activity has been observed for nearly 300 years. The distortion of the San Bruno obelisk after the February 5, 1783 Calabria earthquake, intensity XI-XII MCS, is cited as the first illustration of these phenomena [1, 2], and now it is a symbol of seismic rotational effects. Starting with that event, we can find a large number of other examples of observed rotation effects resulting

from historical earthquakes where the description of 12 majors ones (VII-XI MSC) can be found [3]. The shallow, catastrophic 2009 l'Aquila earthquake was a source of more than hundreds of evidenced rotational effects. Its analysis [4] revealed a tectonic dependence of their distribution and the influence of substrate. From the above, positive correlations have been found between rotation effects, damage and soft lithology of the site where buildings are located.

However, the term 'rotation' has several meanings in seismology. Displacement of rocks, soils and various objects during an earthquake in the focal area and its vicinity, and reversible rotational oscillations in the seismic wave field are called 'seismic rotations.' The historical explanation of observed seismic rotations based on mechanical models can be found in [5, 6], whereas Section 2. summarizes their explanations on the basis of continuum models.

Recently, it is believed that rotational signals contain additional information, valuable for studies on wave propagation, and that the rotational ground motion is an important source of excitations in the engineering structures. Therefore, increasing interest in rotational motions' measurement has emerged. From seismological point of view, it is an area of a rotational seismology which according to [7] becomes an emerging field for the study of all aspects of a rotational ground motion induced by earthquakes, explosions, and ambient vibrations. This domain is very interesting for researchers from a wide range of geophysical disciplines, including broadband seismology, strong motion seismology [8], earthquake physics [9, 10], seismic hazards [11], seismotectonics [12], geodesy [13], and for physicists using Earth-based observatories for detecting gravitational waves generated by astronomical sources [14–16]. Additionally, it is interesting for researchers of earthquake engineering, where seismic behavior of different engineering structures is investigated [17] to search for their optimal seismic design [18].

However, rotational seismology needs a new methodology and new instruments for more reliable recordings. A rigorous analysis of existing classical solutions delivered from instruments for seismological investigation [19] shows their limited usefulness for rotational events recording, mainly because of their sensitivity to linear motions, as well. For the abovementioned reason, in Section 3, we have summarized the main types of rotational seismometers that now exist, with comments on their usefulness. This description shows that a new approach taking advantage of the von Laue-Sagnac effect [20] is the most promising one. Finally, in Section 4, recent results regarding rotational events' detection, which are obtained in Poland, based on such approach are presented and discussed.

This chapter presents the description, the principle of operation, and the comparison of main technical parameters regarding requirements of rotational seismology. This will help seismologists and earth scientists involved in seismic studies to choose the best method for analyzing problems related to seismic rotation.

2. Seismic rotation in various continuum models

In all continuum models mentioned in this section, the wave motion, possibly with rotations, comes from the integration of motions and deformations of numerous small bodies, which form the given continuum. Exterior conditions or forces play only a minor role with the exception of a discontinuous surface. There exists a tension between two types of solid material's

mechanical features such as rock mass and soil. In the first case, the continuous material can translate rectilinearly in its body. A mechanical impulse is translated in a medium as the elastic wave in two simultaneous ways: as compressional-dilatational deformations—the longitudinal wave and transverse shape distortions—the transverse wave. In the second case, both the continuous and grainy solid matter can also be translated into rotational motions in which we distinguish a rotation (named also rigid rotation, or simply a turn) and a symmetric-shape distortion—the shear. It should be underlined that in the elastic theory, there is no place for a rigid rotation, as it would introduce a complicated deformation state around the small body which turns. This theory explained so many phenomena; as a result, the idea of rotation was not accepted.

Recently, it becomes clear that the S-waves comprise rotations of axes perpendicular to the wave propagation. For the plane wave, a suitable relation was found by Igel et al. [21] joining this rotation velocity to transverse acceleration and phase velocity. Rotation curves were very similar to signals of a horizontal acceleration divided by twice the phase velocity (all measured in SI units). The relation was confirmed with a simple geometrical consideration of motions [22, 23]. The same results were found also in the seismic near field, where the spherical wave front was taken as a sufficient approximation [24, 25]. This aspect of the measured oscillations leads to one of the reasons to study rotations—the phase velocity may be easily assessed in this way. The same relation is valid for a love-type surface wave. Since measurements usually proceed on the Earth's surface, rotations about horizontal axis, as in Sv and Rayleigh waves, are not amenable to this method. Finally, various reasons can be found for the presence of rotations also in a P-waves' part of a seismic event trace. For instance, it must be noted that in reality, far from ideal conditions, P-waves are not entirely longitudinal, as well as S-waves bear not only shearing deformations.

It must be noted that this geometrical aspect of rotation does not solve all the problems. Microscopic motions and deformations may not be uniform and not have the same sense. Possible modes of their propagation have been formulated within the vast area of micromorphic studies (including micropolar variant of theories) led by mathematicians and physicists [26]. This branch of science is also named the generalized continuum theory. This trend, initiated by Cosserat brothers in 1909 [27], started to flourish decades later with works of Eringen [28], Nowacki [29, 30], and others. In the micromorphic approach, solid material is taken consisting of numerous small (not infinitesimal) bodies, often called shells, which are capable of deformations and rotations. Various modes of passing them from one body to the other have been proposed [31], and this leads to the independent rotational waves' concept [32, 33]. Individual small body in the undeformed state is usually seen as a cube; each of its sides may react not only to a vector of stress but also to their couple. Couple stress denotes a noncentric interaction between small bodies: a pair of forces act on the body's surface and their moment "tries" to distort or rotate the body. This theoretical small body is treated, in some works, as anisotropic layered entity [34].

In some works, joints between small bodies are treated as important elements in the deformation/propagation process. Among the particle-based numerical studies, there are such in which neighboring particles (small bodies) are linked by elastic bonds "…which can transfer elastic forces, both attractive or repulsive" and break if the distance between the pair exceeds a certain threshold. Such model allows shearing, twisting, and bending interactions between two bonded particles. Used in simulating fracturing, this model facilitates realistic results [35].

The contemporary studies on generalized elasticity can be found in the works of Grekova [36] as well as in the works of Neff et al. [37], which finally concluded that the rotations that are treated as antisymmetric motions/deformations should also be presented. Review on the topic has been prepared by Hadjesfandiari and Dargush [38], which concluded that when an elastic wave propagates through the medium considered in accordance with generalized elasticity concepts, its elements undergo angular motions. Despite the fact that the micromorphic approach is more visible in acoustics or in the studies on various materials than in the geophysics, recent [39–41] search for laboratory confirmation of the micromorphic concepts of seismic rotation yielded sound results, as well.

Original theory of rotational components of a seismic field has been developed by Teisseyre. Starting from elastic continuum with defects [42], he constructed a model of rotations and shears' generation and propagation on the base of constitutional bonds between the antisymmetric part of stresses, density of self-rotation nuclei and the stress moments. Finally, a linear continuum theory, incorporating asymmetric (symmetric plus antisymmetric) stress field, as well as shears and rotations, was introduced [43–45]. In this theory, rotation and shear propel each other. Developing stages of abovementioned theories helped to popularize the rotational seismology in the sciences and resulted in the monographs by [9, 10]. Teisseyre works also accomplished field studies with the use of original microarray of sensors [46–49].

Near-field rotation effects were explained by the action of a nonlinear deformational bend-rotation wave [50]. Several studies point to the possibility of rotational soliton waves (pulses) generated during an earthquake in the focal area, then propagating slowly along fault and triggering new events [51].

Beside verifications of theoretical concepts, dynamic measurements of a real earthquake wave field are urgently needed. These should be best done with special devices enabling detection and recording of rotational motions. Such devices generally named the rotational seismometers or seismographs appeared relatively not long ago, and description of their current state is given in the following section.

3. Current state of rotational seismometers

The main thing regarding the practical construction of a rotational seismometer is a proper description of the fundamental parameters required for such sensor. The general scope of such parameters for a rotational seismometer, which is used for recording signals connected with rotational seismic effects was formulated only 5 years ago in 2012 by [52] as the following four requirements: (1) independently; (2) assures portable size as well as stable work under changing ambient conditions (temperature, humidity, vibration, pressure,…); (3) uses independent power supply that assures autonomous work; and (4) protects measuring rotation rate with an amplitude of the order of 10–7 rad/s at a frequency range between 0.01 and 0.1 Hz. Moreover, (1) the device should be completely insensitive to linear motion or has possibility to measure linear and rotational movements, and the similar requirements were also described for an earthquake engineering area of rotational seismology interest; the first three

were the same and only the last one differs in a measuring range containing amplitude up to a few rad/s at a frequency range up to 100 Hz [53].

A formulation of main requirements for rotational seismometers regarding the rotational seismology is useful for a review of available current solutions in this area. Generally, all used devices can be classified as mechanical, acoustical, electrochemical, and optical devices.

The mechanical systems were historically first used, and they can detect rotation in two ways: directly and nondirectly. The directly rotation detecting systems represent modern mechanical rotational sensors based on a highly miniaturized technique named micro electro-mechanical systems (MEMS). Originally, this technique was developed for manufacturing integrated accelerometers for airborne applications. Rotational seismometers in this technique, usually called MEMS gyro, resemble microelectronic systems in terms of size and production methods. MEMS gyros use the Coriolis effect, and each type of these sensors currently uses vibrating proof masses, which generally vibrate at a high frequency. If the sensor rotates in an inertial space, a Coriolis force is induced on the proof mass. The Coriolis effect generates a vibration in an orthogonal plane, and amplitude of the orthogonal motion can be detected. One can distinguish the following technological structures of MEMS gyros [54]: tuning fork gyros (TFG), hemispherical resonating gyro (HRG) or wine glass resonator gyro, vibrating-wheel gyros, and Foucault pendulum gyros. The biggest advantage of these devices is their mass production at low cost with a small form factor. Systron Donner Inertial (USA), using this technology, manufactured a compact, high reliability, solid-state angular rotation sensor named Horizon™ [55]. It uses vibrating quartz tuning tines to sense rate, acting as a Coriolis sensor, coupled to a similar fork as a pickup to produce the rate output signal (**Figure 1**). Aligned with their support fixtures and frames, these paired tines are fabricated from thin wafers of single crystal piezoelectric quartz.

Another company, Gladiator Technologies Inc., offers six models of MEMS gyros, which are very small, portable and of ultra-low power consumption (see **Figure 1c**) [56]. Nevertheless, the products by both abovementioned companies do not fulfill requirements for entirely rotational seismology as shown in the study, and their parameters are listed in **Table 1**. They are suited solutions as an additional device, which can be used for laboratory investigation, mainly for a rotational seismology engineering application (see example [57]).

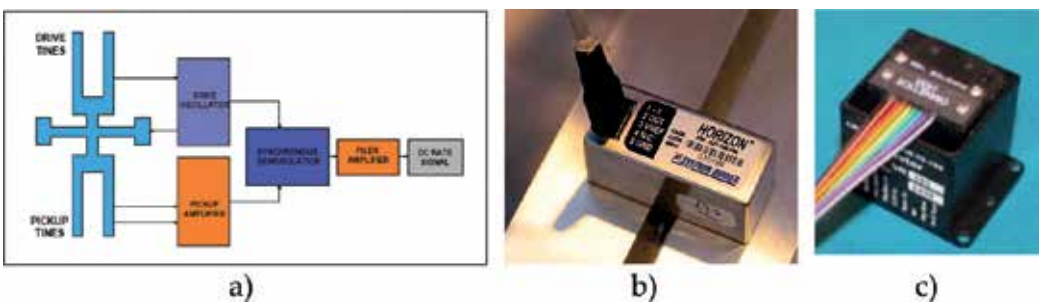

Figure 1. MEMS gyros: (a) scheme of operation, (b) the Horizon™ MEMS angular rate sensor HZ1-100-100, and (c) Gladiator Technologies Inc. model G200D [56].

Parameter	Unit	HZ1–200-100 [55]	G200D [56]
Axial		Uniaxial	Triaxial
Sensitivity[1]	rad/s/√Hz	4.4×10^{-4}	8.7×10^{-5}
Maximum rate	rad/s	3.49	5.23
Frequency band	Hz	>60	Bandwidth 200
Operating temperature	°C	−40 to +71	−40 to +85
Calibration (S.F. dev. from 20/22°C)	%/°C	<0.08	<0.05
Shock survival	g	200	500
Power supply	VDC	8–12	3.1–5.5
Supply current	mA	<20	<300
Power consumption	W	0.24	0.30
Weight	kg	<0.06	<0.031
Dimensions (L × W × H)	mm	58.3 × 25.3 × 25.3	25.4 × 25.4 × 25.4

[1]An output noise for SNR = 1 also defined as a resolution @ 1 Hz in (rad/s).

Table 1. The main parameters of the rotational sensors in the MEMS technology.

The mechanical systems working in an indirect way use defined pairs of classical seismometers. The first of them named Rotaphone based on commercially available geophones arranged in parallel pairs has been mounted on a rigid frame. They have been applied to record seismic events induced by natural sources (weak earthquakes with measured rotation about 10^{-6} rad/s) and anthropogenic sources (blasts with measured rotation about 10^{-3} rad/s) [24, 59–61]. They can be described as a recording system of ground velocity and rotational rate at a point. In order to obtain the rotational rate accurately, special gradients of the ground velocity wave field have to be measured. In 2010, a system named 6DOF (six-degree-of-freedom, see **Figure 2a**) was developed containing eight horizontal and one vertical geophones SM-6 (Sensor Nederland, B.V.), and it was mounted onto a cubic-shaped metal frame. It gives the possibility of recording three Cartesian components of ground velocity and three rotation rate components about Cartesian axes. Finally, the system named Rotaphone-D used 16 (eight horizontal and eight vertical) SM-6 geophones mounted around disc with a separation of the paired geophones of 0.4 m, as shown in **Figure 2b** [58]. The separating distances were chosen to correlate with a specific wavelength of interest. Data from **Table 2** show that Rotaphone is close to fulfilling

Figure 2. Schematic and general view of Rotaphones: (a) 6DOF prototype II [24] and (b) Rotaphone-D [58].

Parameter	Unit	Rotaphone	
		6DOF [24]	D [58]
Frequency range	Hz	2–60[1]	2–80[1]
Sampling frequency	Hz	250	250
Sensitivity[2]	rad/s	2.16×10^{-9}	3.77×10^{-9}
Maximum rate	rad/s	2.87×10^{-1}	3.17×10^{-2}
Dynamic range	dB	120	120
Operating temperature	°C	−20–40	−40–100[3]
Weight	kg	9.5	15.3
Dimensions (L × W × H)	mm	350 × 350 × 430	445[4] × 112
Natural frequency	Hz	4.5	4.5
A/D converter (dynamic)	Type (Bit)	4 × Tedia (28)	1 × EE & S (24)

[1]The instrument generally operates in a high-frequency range (above the natural frequency of the sensors used).
[2]Understood as an expression for the smallest signal that can be resolved ([19] p. 79).
[3]Data for geophone SM-6.
[4]Disc diameter.

Table 2. The main parameters of Rotaphone rotational seismometers.

the requirements for seismological applications. However, their frequency ranges are still too narrow, and they should be treated as short-period systems. The other type of mechanical rotational seismometer operating in an indirect way named TAPS is described later.

The electrochemical rotational seismometers use molecular electronic transfer (MET). One can point out R-1 and R-2 from Eentec (USA) as representative in this group. Sensor construction is based on the electrochemical transducer contained in a channel filled with an electrolytic solution [63]. It includes four fine platinum mesh electrodes separated by microporous spacers (**Figure 3**). The fluid motion is converted into an electrical signal by using the ions' convective diffusion in electrolyte. The rotational seismometer has a toroidal channel filled

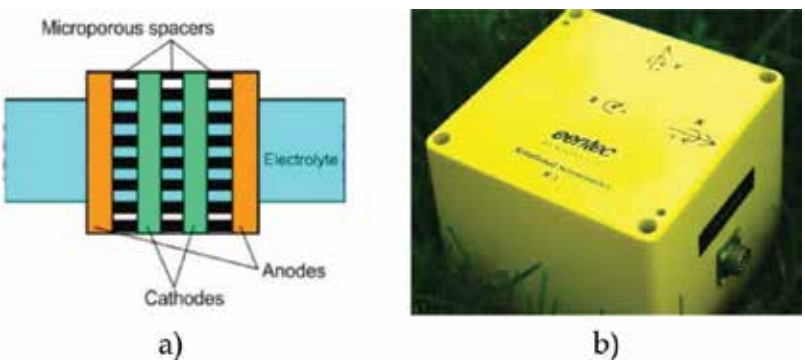

Figure 3. The electrochemical rotational seismometer: (a) schematic diagram of the MET transducer and (b) the Eentec R-1 [62].

with electrolyte. If the sensor rotates, liquid is forced through the MET sensor placed across the channel, converting liquid motion into electrical output. The parameters of R-1 and R-2 (see **Table 3**) are very close to fulfilling all technical requirements for entirely rotational seismology for both seismological and engineering applications.

Nevertheless, measurements carried out in the last decade showed reasonable results only for higher frequencies. The test with model R-1 showed its linear sensitivity equal to 6×10^{-5} rad/s/(m/s^2) and a 2% cross-axis sensitivity [65]. The calibration quality casts also doubt in lower frequency range (<1 Hz) [66] since the frequency response does not have a flat shape, and at frequencies above 1 Hz, the dynamic range is only 80 dB [56]. Moreover, the measurement [52] in a temperature range of 20–50°C revealed deviations in the scale factor from the nominal value equaling 27 and 18% for R-1 and R-2, respectively, which suggests that this technology needs to be improved. In spite of the abovementioned disadvantages of the electrochemical seismometers, the R-1 model has recorded several hundreds of local earthquakes and two explosions in Taiwan [67].

The sensors designed by Applied Technology Associates (USA) [68] represent another technology with fluid. These devices operate based on the physical principle named magnetohydrodynamics (MHD). The main part of the sensing is a rotational proof mass containing conducting fluid as well as a permanent magnet that is fixed to the sensor case (**Figure 4**). The case-fixed magnetic flux moves through the inertially fixed conducting fluid with relative velocity as the case is rotated with the angular velocity Ω. This relative velocity between the magnetic flux and the fluid conductor generates a radially oriented electric field. This interaction or the MHD effect produces a voltage difference between the electrode surfaces that may be amplified by a transformer or other active electronic amplifier configurations. The signal (voltage output) is proportional to the angular rate Ω [70].

Parameter	Unit	R-1 [62]	R-2 [64]
Axial		Triaxial	Triaxial
Sensitivity[1]	rad/s/√Hz	1.2×10^{-7}	0.6×10^{-7}
Maximum rate	rad/s	0.10	0.40
Dynamic range	dB	110	117
Frequency band (extended)	Hz	0.05–20 (0.03–50)	0.03–50 (0.01–100)
Scale factor[2]/optional	V/rad/s	50/ 2×10^2	50/5–2×10^2
Operating temperature	°C	−15 to +55 (extended −45 to +55)	
Shock survival	g	200	200
Power supply	VDC	9–14	9–18
Power consumption	W	0.28	0.54
Weight	kg	1.0	1.5
Dimensions (L × W × H)	mm	120 × 120 × 90	120 × 120 × 100

[1]An output noise for SNR = 1 also defined as a resolution @ 1 Hz in (rad/s).
[2]Understood as the gain of the instrument ([19] p. 79).

Table 3. The main parameters of rotational seismometers R-1, R-2.

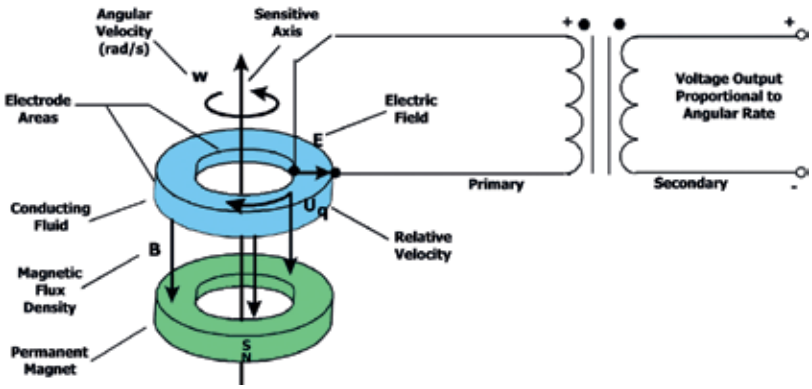

Figure 4. Principle of magnetohydrodynamics effect of a conductive fluid in the presence of a magnetic field [69].

At ATA website, one can find two models of angular rate sensors: ARS-14 and ARS-15 (**Figure 5a** and **b**), where ARS-14 is able to measure angular motions as low as 30 nanoradians. Nevertheless, it should be emphasized that the sensor construction in MHD technology limits the frequency bandpass because the lower corner frequency is a function of parameters such as conductive fluid and fluid proof geometry. The upper value of a frequency bandwidth is usually determined by a signal processing unit. The ATA model Proto-SMHD (**Figure 5c**) which can be found in [69] is interesting because it is the device suited for microseismic signal detection. Nevertheless, in the literature, there are no examples of these sensors application for recording effects connected with rotational seismology.

The last group is the optical systems operating based on the Sagnac effect [72] (more precisely, the von Laue-Sagnac effect). They are interferometric devices which use light for rotation detection. For the abovementioned reason, they have nonfrequency dependence of an output signal. The optical rotational seismometer exists in laser (RLG) or fiber (FOG) technology.

The ring laser gyroscopes (RLGs) detect the Sagnac beat frequency of two counter-propagating laser beams, which are propagated along a rectangular or triangular perimeter (**Figure 6a**). In the RLG, two coherent laser beams of an equal wavelength are generated. They are introduced into the system, and they circulate around the closed cavity in opposite directions. If the whole

Figure 5. Various models of angular rate sensors by ATA: (a) ARS-14, (b) ARS-15 [69], and (c) Proto-SMHD [71].

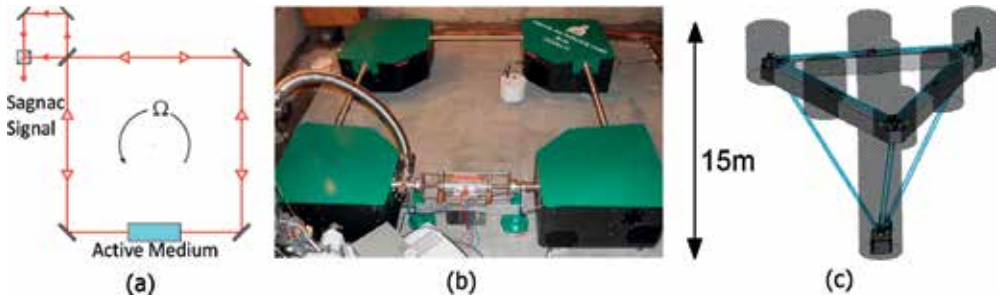

Figure 6. The ring laser gyroscope: (a) principle of operation, (b) GEOSensor [73], and (c) ROMY project—schema of the construction [74].

system rotates, the effective cavity length between the counter-propagating laser differs and a frequency splitting of two counter-propagating optical waves is obtained. The Sagnac frequency, δf, is described as:

$$\delta f = \frac{4A}{\lambda P} n\Omega \tag{1}$$

where A and P are the area and perimeter enclosed by the beam path, respectively; λ is optical wavelength of the laser oscillation, Ω is vector of angular velocity at which the instrument is turning; n is normal vector to the laser beam plane.

The RLGs have been applied for the rotational seismic events recording since the 1990s. The first ring laser gyroscope named "C-I" was assembled in the University of Canterbury in New Zealand in 1988–1990, and their parameters can be found in [75]. The next version was the ring laser "C-II" [76]. Its cavity with an area of 1.0 m^2 was equipped with an ultra-high vacuum between metal flanges and a solid piece of Zerodur (glass ceramic with a low thermal expansion coefficient). The ring laser gyro with an area of 16 m^2 and named ring laser "G" was assembled at Wettzell, Germany in 1998–2001. The bigger ring laser gyro named "UG-1" is installed in Cashmere Cavern, New Zealand. Its laser cavity has an area of 367 m^2. Especially, for seismological application, the ring laser "GEOsensor" has been designed and assembled at Wettzell, Germany. The "ROtational Motions in seismologY (ROMY)" [74] is a big project under the leadership of Igel. During the project, an apparatus consisting of four individual triangular ring lasers arranged in the shape of a tetrahedron with 12 m of length on each side (**Figure 6c**) will be used. The ROMY's constructors expect sensitivity in the range between 0.02 and 0.05 × 10^{-12} rad/s [74]. **Table 4** summarizes the fundamental parameters of various RLG systems. As one can see, there are not so many installations of RLGs, mostly because of their high cost and high sophistication involved in installation. They are very sensitive to external local disorders such as temperature, noise or pressure. Due to their dimensions and special isolation, they are unable to be transported.

Regarding the practical application of the optic rotational seismometer in fiber technology, the authors have knowledge only about one, other than their solution described in the next section, from iXBlue (France) named blueSeis-3A. Its parameters are available on web page http://www.blueseis.com as: portable, three-component system with 0.01–100 Hz broadband,

RLG name	Area (m^2)	Sensitivity (rad/s/√Hz)
C-II	1	7.2×10^{-10}
G	16	9.0×10^{-11}
UG1	367	4.7×10^{-12}
GEOsensor	2.56	4.5×10^{-11}
ROMY	249	$(0.02–0.05) \times 10^{-12}$

Table 4. The sensitivity of different RLG systems used for rotation detection.

low noise <20 nrad/s/√Hz, high dynamic range, Plug & Play, no calibration needed, maintenance-free, embedded digitizer, GNSS time stamping, and so on.

4. Comparison of results obtained from measurements using optical and mechanical rotational seismometers

Finally, in this section, we compare results obtained from two rotational seismometer systems installed for a continuum measurement in Książ, Poland seismological observatory—the Fibre-Optic System for Rotational Events& phenomena Monitoring (FOSREM) based on a fiber-optic gyroscope and the Twin Antiparallel Pendulum Seismometers (TAPS) based on microarray of mechanical seismometers.

FOSREM is a new version of Autonomous Fibre-Optic Rotational Seismometer (AFORS), which was used between 2007 and 2017 in Książ. Each FOSREM contains three basic parts, which work interdependently: rotational seismometers FOSREM-XX type, data transmission unit (DTU), and power communication unit (PCU), see **Figure 7a**. The heart of the FOSREM—the rotational seismometer FOSREM-XX type—contains an optical head for generating the phase shift proportional to the detected rotation rate as well as the electronic part for data processing (**Figure 7b**). The optical head is constructed according to a so-called minimum configuration of FOG [77]. The light beam emitted by the source SLED is halved by the coupler and propagated to the sensor loop where two beams are propagating in the opposite direction. The sensor loop has been constructed by winding of 5 km SMF-28e + fiber in a double-quadrupole mode on a 0.215 m duralumin circular frame with attenuation equal to 0.35 dB/km@1310 nm [78]. The two polarizers mounted in line between two couplers assure the same optical path for the both counter-propagating waves. In order to shift the operating point to quadrature point of operation, the phase modulator at the end of the sensors loop was applied. The detected rotation rate is obtained by a specially designed system of filters (see **Figure 7b**), which properly select and amplify the first ($A_{1\omega}$) and the second ($A_{2\omega}$) amplitude of harmonic detected output signal u(t). The electronic part calculates the rotation rate Ω. Applying the following equation [79]:

$$\Omega(t) = S_o \tan^{-1}\left[S_e\, u(t)\right] = S_o \tan^{-1}\left[S_e\left(\frac{A_{1\omega}}{A_{2\omega}}\right)\right], \tag{2}$$

S_o and S_e are optical and electronical constant of the interferometer, respectively.

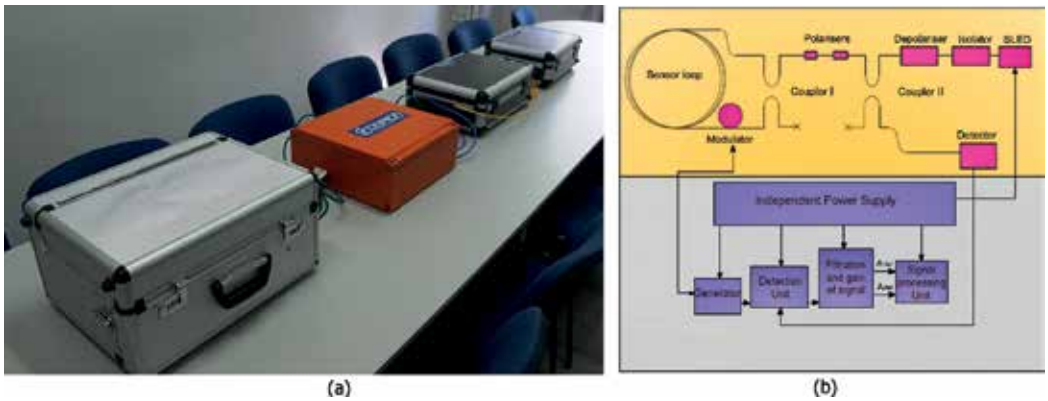

Figure 7. FOSREM: (a) from left: rotational seismometer FOSREM-SS, FOSREM-BB, data transmission unit (DTU), and power communication unit (PCU); (b) schematic diagram of FOSREM-XX, top—optical head, bottom—electronic part.

In order to continuously collect data, the special software has been applied which enables the recording of only values of signals, which gained the assumed level of event [79]. The DTU enables a synchronic data recording from up to three rotational seismometers with their collection on a local disc as well as a transfer to PCU via fiber link. The PCU transmits the recorded data using Internet or GSM/GPS to a dedicated server FOSREM with a rate up to 100 Mbps. Furthermore, PCU enables the device to run for a minimum of 12 h.

Table 5 summarizes the main parameters of three fiber systems used by our team. They differ in sizes, mechanical protections, and measuring range. AFORS and FOSREM-SS are suited for seismological investigation, but they cannot be applied for an engineering application because they have limited detection of the maximum rotation rate. FOSREM-BB due to the optimized optical part and the special software solution allows for the rotation rate detection in a wider range of signal amplitude up to 10 rad/s.

AFORS and FOSREM may work even when tilted; moreover, when used in continuous mode, they may record the tilt. They are portable, easy to assemble, as well as fully remotely controlled via Internet. It makes them as suitable devices to work with in a continuous mode for a very long period of time (weeks, months, and even years). For these reasons, AFORS (in 2007) and two FOSREM-SS (in 2017) have been mounted in seismological observatory in Książ in order to gather data connected with rotational seismic events.

As a reference system, the TAPS has also been mounted in Książ. TAPS is a mechanical rotational sensor constructed by a group from Institute of Geophysics PAS, Poland [80]. It is a set of two antiparallel pendulum seismometers (SM-3 type, Russia) mounted at one axis and connected parallel with opposite orientations (**Figure 8**). If the ground motion includes the displacement $u(t)$ and the only vertical rotation $\Omega(t)$, the electromotive force (EMF) $f(t)$ recorded by each SM-3 contains the component of displacement $\pm u(t)$ and the rotational motion $\Omega(t)$ multiplied by the proper length of the pendulum l [80]:

$$f_{L,R}(t) = \pm u(t) + l \cdot \Omega(t), \tag{3}$$

	Unit	AFORS	FOSREM-SS	FOSREM-BB
Picture of the optical head				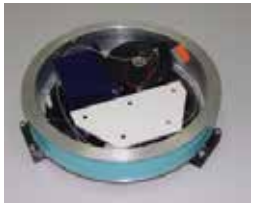
Optical losses	dB	14.47	16.89	16.37
Theoretical sensitivity	rad/√Hz	4×10^{-9}	2.18×10^{-8}	2.06×10^{-8}
Frequency bandpass	Hz	0.83–106.15	DC–328.12	
Accuracy in bandpass	rad/s	$(0.48–6.1) \times 10^{-8}$	3×10^{-8}–1.6×10^{-6}	
Angle Random Walk	rad/√Hz	1.2×10^{-8}	3.2×10^{-8}	4.9×10^{-8}
Bias instability	rad/s	1.1×10^{-8}	1.6×10^{-8}	0.8×10^{-8}
Dimension	mm	$700 \times \phi = 160$	470 × 360 × 230	360 × 360 × 160
Weight	kg	~18	~10	
Operating temperature	°C	0–50		
Measuring range	rad/s	4×10^{-9}–6.4×10^{-3}	2×10^{-8}–0.06	2×10^{-8}–10

Table 5. The main parameters of rotational seismometers AFORS and FOSREM type.

http://dx.doi.org/10.5772/intechopen.72169

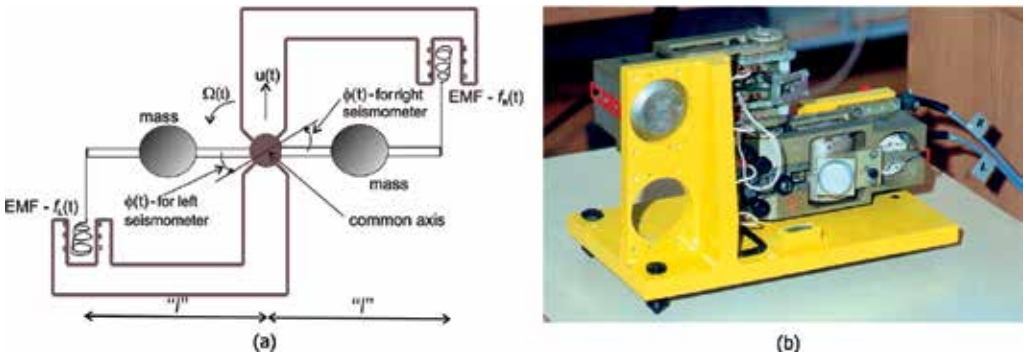

Figure 8. The TAPS rotational seismometer: (a) scheme [81] and (b) general view. ϕ(t) is the angle of rotation for a given pendulum.

where the signs "+" and "−"represent right (R) and left (L) seismometers, respectively. From the above, the rotational and translational components can be obtained from the sum and difference of two recorded signals, respectively as:

$$\Omega(t) = \frac{1}{2l}\left[f_R(t) + f_L(t)\right] \text{ and } u(t) = \frac{1}{2l}\left[f_R(t) - f_L(t)\right]. \quad (4)$$

Due to the rotational rate determination from the sum of the measured signals, the inaccuracies and difficulties can be observed. If the two antiparallel seismometers are precisely the same, the sum of the signals is proportional to the rotation rate. Taking into account the practical aspects of the pendulums, they are never identical. There is a difference in measured signals, which is widely described in [81]. As a result, it causes noise in the measurements of one order of magnitude greater for TAPS than for SM-3. In practice, the attenuation characteristic differences of the pendulum seismometers equal to a few per cent can generate a false rotational signal, especially if the rotational component is small in comparison with the translation one. There are different solutions for eliminating this problem, unfortunately with limited efficiency. Nowadays, one can find the records obtained by TAPSs including rotational motions during earthquakes [46, 82, 83] and seismic activity connected with artificial detonation in mine regions [84–87]. Unfortunately, this system does not fulfill the requirements for seismological applications of the rotational seismology due to the limited frequency bandpass as well as the measuring range.

In order to illustrate the rotational phenomena in the seismic wave field, we present in **Figure 9** seismograms of seismic events recorded in Książ. This earthquake was felt around Jarocin town and radiated the seismic field with clean rotational components. The distance to the source was of about 200 km. We show the unfiltered diagrams of the whole waveforms, but with a low-pass filtration which cut the spectrum at about 12.5 Hz. We decided to use these analyses in order to remove a high-frequency noise. The presented data allow for the comparison of rotational signals obtained by two different devices—TAPS and AFORS which have totally different idea of design. The compatibility between these two sensors is disturbed by differences in their spectral characteristics [86]. Unfortunately, we have observed noncorrelation between TAPS and AFORS for the same set of recorded events. For this reason, we decided to install in Ksiaż two FOSREM-SS in order to obtain more precise data.

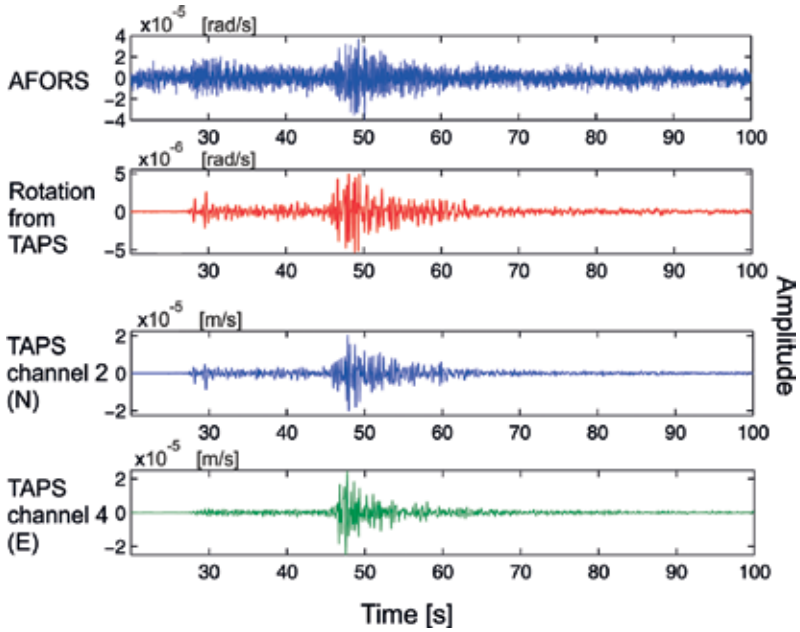

Figure 9. M = 3.8 earthquake near Jarocin, Poland, 2012.01.06, 15:37:56. The uppermost window shows a rotation signal obtained from the AFORS. Plots of the rotation labeled "from TAPS" were obtained with the array method—two TAPSs were used.

5. Conclusions

Several advanced technologies of rotational sensors began to develop due to rapid increasing interest of rotational seismology. Nevertheless, the strict requirements for this scientific discipline are not fulfilled in many cases. From the presented review, it is clear that probably technologies based on optical interferometer are the most promising ones. However, it can be concluded that theoretical and mainly experimental studies of the rotational seismology are still in the initial state of development. Future works should be channeled toward acquiring a large amount of reliable experimental data recorded by different devices regarding rotational events from long distance sources (earthquakes generated in natural ways) as well as from short distance sources (the shocks generated in an artificial way—the explosions in a mine region). Such data are very handy for the confirmation of any theoretical investigation in the area of rotational seismology.

Acknowledgements

This work was carried out with the financial support of the Polish Ministry of Science and Higher Education project POIR.04.02.00-14-A003/16: "EPOS—System Obserwacji Płyty Europejskiej", the National Science Centre, Poland under project 2016/23/N/ST10/02508 as well as the Statutory Activity of the Military University of Technology PBS-654.

Author details

Leszek R. Jaroszewicz[1]*, Anna Kurzych[1], Krzysztof P. Teisseyre[2] and Zbigniew Krajewski[1]

*Address all correspondence to: jarosz@wat.edu.pl

1 Military University of Technology, Warsaw, Poland

2 Institute of Geophysics Polish Academy of Sciences, Warsaw, Poland

References

[1] Vivenzio G. Istoria e teoria de- tremuoti in generale, ed in particulare di quelli della Calabria e di Messina del 1783. Stamperia Reale, Napoli. 1783

[2] Vivenzio G. Istoria de- tremuoti avvenuti nella provincial della Calabria ultteriore e nella citt/E di Messina nell-Anno 1783, e do quanto nella Calabria fu fatto per lo suo Risorggimento fino al 1787, preceduta da una teoria ed istoria generale de tremuoti. Napoli: Stamperia Reale; 1788. pp. 1-2

[3] Kozák JT. Tutorial on earthquake rotational effects: Historical examples. Bulletin of the Seismological Society of America. 2009;**99**(2B):998-1010. DOI: 10.1785/0120080308

[4] Cucci L, Tertulliani A. Clues for a relation between rotational effects induced by the 2009 Mw 6.3 L'Aquila (Central Italy Earthquake) and site and source effects. Bulletin of the Seismological Society of America. 2011;**101**(3):1109-1120. DOI: 10.1785/0120100264

[5] Kozák JT. Development of earthquake rotational effect study. In: Teisseyre R, Takeo M, Majewski E, editors. Earthquake Source Asymmetry, Structural Media and Rotation Effects. 1st ed. Heidelberg: Springer; 2006. pp. 3-10

[6] Hinzen KG. Rotation of vertically oriented objects during earthquakes. Journal of Seismology. 2012;**16**:797-814. DOI: 10.1007/s10950-011-9255-6

[7] Lee WHK, Celebi M, Todorovska MI, Igel H. Introduction to the special issue on rotational seismology and engineering applications. Bulletin of the Seismological Society of America. 2009;**99**(2B):945-957. DOI: 10.1785/01.20080344

[8] Anderson JG. Strong-motion seismology. In: Lee WHK, Kanamori H, Jennings PC, Kisslinger C, editors. The International Handbook of Earthquake and Engineering Seismology, Part B. 1st ed. Amsterdam: Academic Press; 2003. pp. 937-965. DOI: 10.1016/S0074-6142(03)80171-7

[9] Teisseyre R, Takeo M, Majewski E. Earthquake Source Asymmetry, Structural Media and Rotation Effects. 1st ed. Heidelberg: Springer; 2006. p. 582. ISBN: 978-3-540-31337-3

[10] Teisseyre R, Nagahama H, Majewski E. Physics of Asymmetric Continuum: Extreme and Fracture Processes. Earthquake Rotation and Soliton Waves. 1st ed. Heidelberg: Springer; 2008. p. 293. ISBN: 978-3-540-68354-4

[11] McGuire R. Probabilistic seismic hazard analysis: Early history. Earthquake Engineering & Structural Dynamics. 2008;**37**:329-338. DOI: 10.1002/eqe.765

[12] Presentation on Seismotectonics from the Department of Geophysics, University of Munich [Internet]. 2016. Available from: www.geophysik.uni-muenchen.de/~igel/Lectures/Sedi/sedi_tectonics.ppt [Accessed: August 10, 2016]

[13] Carey SW. Earth expansion and the null universe. In: Carey SW, editor. Expanding Earth Symposium, Sydney, 1981. 1st ed. Hobart: University of Tasmania; 1983. p. 365-372

[14] Ju L, Blair DG, Zhao C. Detection of gravitational waves. Reports on Progress in Physics. 2000;**63**:1317-1427. PII: S0034-4885(00)07909-4

[15] Lantz B, Schofield R, O'Reilly B, Clark DE, DeBra D. Review: Requirements for a ground rotation sensor to improve advanced LIGO. Bulletin of the Seismological Society of America. 2009;**99**(2B):980-989. DOI: 10.1785/0120080199

[16] Ross MP, Venkateswara K, Hagedorn CA, Gundlach JH, Kissel JS, Warner J, et al. Low Frequency Tilt Seismology with a Precision Ground Rotation Sensor. arXiv:1707.03084 [physics.geo-ph]. July 25, 2017

[17] Trifunac MD. Review: Rotations in structural response. Bulletin of the Seismological Society of America. 2009;**99**(2B):968-979. DOI: 10.1785/01.20080068

[18] Mustafa A. Earthquake Engineering—From Engineering Seismology to Optimal Seismic Design of Engineering Structures. 1st ed. Rijeka: InTech; 2015. p. 408. DOI: 10.5772/58499

[19] Havskov J, Alguacil G. Instrumentation in Earthquake Seismology. 2nd ed. Heidelberg: Springer; 2016. p. 413. DOI: 10.1007/978-3-319-21314-9

[20] Post EJ. Sagnac effect. Reviews of Modern Physics. 1967;**39**:475-494. DOI: 10.1103/RevModPhys.39.475

[21] Igel H, Schreiber U, Flaws A, Velikoseltsev A, Cochard A. Rotational motions induced by M8.1 Tokachi-oki earthquake, September 25, 2003. Geophysical Research Letters. 2005;**32**:L08309. DOI: 10.1029/2004GL022336

[22] Cochard A, Igel H, Schuberth B, Suryanto W, Velikoseltsev A, Schreiber U, et al. Rotational motions in seismology: Theory, observation, simulation. In: Teisseyre R, Takeo M, Majewski E, editors. Earthquake Source Asymmetry, Structural Media and Rotation Effects. 1st ed. Heidelberg: Springer; 2006. pp. 391-411

[23] Schreiber KU, Hautmann JN, Velikoseltsev A, Wassermann J, Igel H, Otero J, et al. Ring laser measurements of ground rotations for seismology. Bulletin of the Seismological Society of America. 2009;**99**(2B):1190-1198. DOI: 10.1785/0120080171

[24] Brokešová J, Málek J. Six-degree-of-freedom near-source seismic motions I: Rotation-to-translation relations and synthetic examples. Journal of Seismology. 2015;**19**(2):491-509. DOI: 10.1007/s10950-015-9479-y

[25] Brokešová J, Málek J. Six-degree-of-freedom near-source seismic motions II: Examples of real seismogram analysis and S-wave velocity retrieval. Journal of Seismology. 2015;**19**(2):511-539. DOI: 10.1007/s10950-015-9480

[26] Grekova EF, Lee WHK. Suggested readings in continuum mechanics and earthquake seismology. Bulletin of the Seismological Society of America. 2009;**99**(2B):1076-1081. DOI: 10.1785/0120080343

[27] Cosserat E, Cosserat F. Théorie des corps déformables. Librairie Scientifique A. Hermann et Fils. 1909 (Engl. translation by D. Dedelphenich 2007). Available from: www.uni-due.de/~hm0014/Cosserat_files/Cosserat09_eng.pdf [Accessed: July 21, 2016]

[28] Eringen AC. Microcontinuum Field Theories. 1st ed. Berlin: Springer; 1999. p. 248. ISBN 978-1-4612-0555-5

[29] Nowacki W. Theory of micropolar elasticity. Course Held at the Department for Mecha-Nics of Deformable Bodies. 1st ed. Wien: Springer; 1970. p. 266. ISBN: 978-3-7091-2720-9

[30] Nowacki W. Thermoelasticity. 2nd ed. Warsaw: PWN—Polish Scientific Publishers/ Pergamon Press; 1986. p. 578. ISBN-10: 1483130061

[31] Merkel A, Tournat V, Gusev V. Dispersion of elastic waves in three-dimensional non-cohesive granular phononic crystals: Properties of rotational modes. Physics Review. 2010;**E82**:03305. DOI: 10.1103/PhysRev.E.82.031305

[32] Parfitt V, Eringen A. Reflection of plane waves from the flat boundary of a micropolar half-space. The Journal of the Acoustical Society of America. 1969;**45**:1258-1272. DOI: 10.1121/1.413086

[33] Pujol J. Tutorial on rotations in the theories of finite deformation and micropolar (Cosserat) elasticity. Bulletin of the Seismological Society of America. 2009;**99**(2B):1011-1027. DOI: 10.1785/0120080161

[34] Wang Y, Abe AS, Latham S, Mora P. Implementation of particle-scale rotation in the 3-D lattice solid model. Pure Applied Geophysics. 2006;**163**:1769-1785. DOI: 10.107/s00024-006-0096-0

[35] Kulikov GM, Plotnikova SV. Simple and effective elements based upon Timoshenko-Mindlin shell theory. Computer Methods in Applied Mechanics and Engineering. 2002;**191**:1173-1187. DOI: 10.1023/A:1020978008577

[36] Grekova EF. Nonlinear isotropic elastic reduced Cosserat continuum as a possible model for geomedium and geomaterials. Spherical prestressed state in the semilinear material. Journal of Seismology. 2012;**16**:695-707. DOI: 10.1007/s10950-012-9299-2

[37] Neff P, Ghiba ID, Madeo A, Placidi L, Rosi G. A unifying perspective: The relaxed linear micromorphic continuum. Continuum Mechanics and Thermodynamics. 2014;**26**:639-681. DOI: 10.1007/s00161-013-0322-9

[38] Hadjesfandiari AR, Dargush GF. Evolution of generalized couple-stress continuum theories: A critical analysis. Preprint. 2014. Available from: www.arxiv.org/abs/1501.03112 [Accessed: July 18, 2016]

[39] Merkel A, Tournat V, Gusev V. Experimental evidence of rotational elastic waves in granular photonic crystals. Physical Review Letters. 2011;**107**:225502. DOI: 10.1103/PhysRevLett.107.225502

[40] Cabaret J, Béquin P, Theocharis G, Andreev V, Gusev VE, Tournat V. Nonlinear hysteretic torsional waves. Physical Review Letters. 2015;**115**:054301. DOI: 10.1103/PhysRevLett.115.054301

[41] Allein F, Tournat V, Gusev VE, Theocharis G. Transversal-rotational and zero group velocity modes in tunable magneto-granular phononic crystals. Extreme Mechanics Letters. 2017;**12**:65-70. DOI: 10.1016/j.eml.2016.08.001

[42] Kröner E. Continuum theory of defects. In: Balian R et al, editors. Les Houches, Session XXXV, 1980, Physique des Defauts/Physics of Defects. 1st ed. Dordrecht: North Holland Publishing Company; 1982. p. 890. ISBN-13: 978-0444862259

[43] Teisseyre R. Spin and twist motions in a homogeneous elastic continuum and cross-band geometry of fracturing. Acta Geophysica Polonica. 2004;**52**:173-184

[44] Teisseyre R. Asymmetric continuum: Standard theory. In: reference [10]. pp. 95-109

[45] Teisseyre R. Tutorial on new developments in the physics of rotational motions. Bulletin of the Seismological Society of America. 2009;**99**(2B):1028-1039. DOI: 10.1785/0120080089

[46] Teisseyre R, Suchcicki J, Teisseyre KP, Wiszniowski J, Palangio P. Seismic rotation waves: Basic elements of the theory and recordings. Annales de Geophysique. 2003;**46**:671-685

[47] Teisseyre R, Suchcicki J, Teisseyre KP. Recording the seismic rotational waves: Reliability analysis. Acta Geophysica Polonica. 2003;**51**:37-50

[48] Teisseyre KP. Mining tremors registered at Ojców and Książ observatories: Rotational field components. Publications of the Institute of Geophysics, Polish Academy of Sciences. 2006;**M-29**(395):77-92

[49] Teisseyre KP. Analysis of a group of seismic events using rotational components. Acta Geophysica. 2007;**55**(4):535-553

[50] Aksenov V. Bend-rotation wave as a mechanism of macroseismic effects. In: Teisseyre R, Takeo M, Majewski E, editors. Earthquake Source Asymmetry, Structural Media and Rotation Effects. 1st ed. Heidelberg: Springer; 2006. pp. 227-240

[51] Majewski E. Spinors and twistors in the description of rotational seismic waves and spin and twist solitons. Bulletin of the Seismological Society of America. 2009;**99**(2B):1137-1146. DOI: 10.1785/0120080160

[52] Bernaue F, Wassermann J, Igel H. Rotational sensors—A comparison of different sensor types. Journal of Seismology. 2012;**16**:595-602. DOI: 10.1007/s10950-012-9286-7

[53] Jaroszewicz LR, Kurzych A, Krajewski Z, Marć P, Kowalski JK, Bobra P, Zembaty Z, Sakowicz B, Jankowski R. Review of the usefulness of various rotational seismometers with laboratory results of fibre-optic ones tested for engineering applications. Sensors. 2016;**16**:2161. DOI: 10.3390/s16122161

[54] Mohite S, Patil N, Pratap R. Design, modelling and simulation of vibratory micromachined gyroscopes. Journal of Physics: Conference Series. 2006;**34**:757-763

[55] Systron Donner, Inc [Internet]. Available from: www.systron.com/sites/default/files/964120_n-hz1.pdf [Accessed: August 24, 2017]

[56] Gladiator Technologies [Internet]. Available from: www.gladiatortechnologies.com [Accessed: August 25, 2017]

[57] Zembaty Z, Kokot S, Bobra P. Application of rotation rate sensors in an experiment of stiffness 'reconstruction'. Smart Materials and Structures. 2013;**22**(7):077001. DOI: 10.1088/0964-1726/22/7/077001

[58] Brokešová J, Málek J, Evans JR. Rotaphone-D—A new six-degree-of-freedom short-period [Internet]. Available from: www.rotational-seismology.org/events/workshops/Presentations_2016/presentations/Brokesova_talk/view [Accessed: August 25, 2017]

[59] Brokešová J, Málek J. New portable sensor system for rotational seismic motion measurements. The Review of Scientific Instruments. 2010;**81**(8):084501. DOI: 10.1063/1.346327.1

[60] Brokešová J, Málek J, Kolínský P. Rotaphone, a mechanical seismic sensor system for field rotation rate measurements and its in situ calibration. Journal of Seismology. 2012;**16**(4):603-621. DOI: 10.1007/s10950-012-9274-y

[61] Brokešová J. Short-period seismic rotations and translations recorded by Rotaphone [Habilitation Thesis]. Appendix G. Prague: Department of Geophysics, Charles University; 2015

[62] Eentec. High Resolution Rotational Seismometer Model R-1 [Internet]. Available from: www.eentec.com/R-1_data_new.htm [Accessed: August 24, 2017]

[63] Abramovich IA, Kharlamov AV. Electrochemical transducer and a method for fabricating the same. Patent US6576103 B2. 2001-08-8

[64] Rotational Seismometers R-2, R3. AST LLC. In: Data Sheet Presented at 4th International Working Group on Rotational Seismology Meeting; 20-23 June 2016; Tutzing. 2016

[65] Nigbor RL, Evans RJ, Hutt C. Laboratory and field testing of commercial rotational seismometers. Bulletin of the Seismological Society of America. 2009;**99**(2B):1215-1227. DOI: 10.1785/0120080247

[66] Wassermann J, Lehendorfer S, Igel W, Schreiber U. Performance test of a commercial rotational motions sensor. Bulletin of the Seismological Society of America. 2009;**99**(2B):1449-1456. DOI: 10.1785/0120080157

[67] Lee WHK, Huang BS, Langston CA, Lin CJ, Liu CC, Shin TC, Teng TL, Wu CF. Review: Progress in rotational ground-motion observations from explosions and local earthquakes in Taiwan. Bulletin of the Seismological Society of America. 2009;**99**(2B):958-967. DOI: 10.1785/0120080205

[68] Applied Technology Associates [Internet]. Available from: www.atacorp.com/index.html [Accessed: August 25, 2017]

[69] Applied Technology Associates. Angular Rate Sensors [Internet]. Available from: www.atacorp.com/angular_rate_sensors.html [Accessed: August 21, 2017]

[70] Applied Technology Associates. Magnetohydrodynamic (MHD) Technology [Internet]. Available from: www.atacorp.com/magnetohydrodynamic_mhd_technology.html [Accessed: August 22, 2017]

[71] Applied Technology Associates. Seismic SMHD—Rotational Sensor Development and Deployment [Internet]. Available from: www.osti.gov/scitech/servlets/purl/1258768 [Accessed: August 23, 2017]

[72] Sagnac G. L'ether lumineux demontre par l'effet du vent relatif d'Etherdanus un interferometre en rotation uniforme. C. R. l'Academy of Sciences. 1913;**95**:708-710

[73] The GEOsensor Project: Rotations—A New Observable for Seismology [Internet]. Available from: www.geophysik.uni-muenchen.de/~igel/PDF/schreibertetal_geotech_2005.pdf [Accessed: August 23, 2017]

[74] The ROMY project: ROtational ground Motions: A new observable for seismology [Internet]. Available from: www.rotational-seismology.org/events/workshops/Presentations_2016/ presentations/Igel_talk [Accessed: August 25, 2017]

[75] Stedman GE, Li Z, Bilger HR. Sideband analysis and seismic detection in large ring laser. Applied Optics. 1995;**34**:7390-7396. DOI: 10.1364/AO.34.005375

[76] Stedman GE. Ring-laser tests of fundamental physics and geophysics. Reports on Progress in Physics. 1997;**60**:615-688. DOI: 10.1088/0034-4885/60/6/001

[77] LeFevre HC. The Fiber Optic Gyroscope. 2nd ed. Norwood: Artech House; 2014. p. 313. ISBN: 0-89006-537-3

[78] Kurzych A, Kowalski JK, Sakowicz B, Krajewski Z, Jaroszewicz LR. The laboratory investigation of the innovative sensor for torsional effects in engineering structures' monitoring. Opto-Electronics Review. 2016;**24**(3):134-143. DOI: 10.1515/oere−2016−0017

[79] Kowalski JK, Jaroszewicz LR, Krajewski Z, Kurzych A, Marć P. Measurement method and system for measuring amplitude of first two harmonics of signal derived from Sagnac system. Pat. Appl. PCT/IB2015/059521. 2015-12-10

[80] Teisseyre R, Nagahama H. Micro-inertia continuum: Rotations and semi-waves. Acta Geophysica Polonica. 1999;**47**:259-272

[81] Solarz L, Krajewski Z, Jaroszewicz LR. Analysis of seismic rotations detected by two antiparallel seismometers: Spine function approximation of rotation and displacement velocities. Acta Geophysica Polonica. 2004;**52**:198-217

[82] Moriya T, Teisseyre R. Design of rotation seismometer and non-linear behaviour of rotation components of earthquakes. In: Teisseyre R, Takeo M, Majewski E, editors. Earthquake Source Asymmetry, Structural Media and Rotation Effects. 1st ed. Heidelberg: Springer; 2006. pp. 439-450

[83] Teisseyre R. Continuum with defect and self-rotation fields. Acta Geophysica Polonica. 2002;**50**:51-68

[84] Teisseyre R, Boratyński W. Continuum with self-rotation nuclei: Evolution of defect fields and equation of motion. Acta Geophysica Polonica. 2002;**50**:223-230

[85] Jaroszewicz LR, Krajewski Z, Solarz L, Teisseyre R. Application of the FORS-II for investigation of the seismic rotation waves. Proceedings of SPIE. 2005;**5776**:385-393

[86] Wiszniowski J. Rotation and twist motion recording—Couple pendulum and rigid seismometer system. In: Teisseyre R, Takeo M, Majewski E, editors. Earthquake Source Asymmetry, Structural Media and Rotation Effects. 1st ed. Heidelberg: Springer; 2006. pp. 451-470

[87] Kurzych A, Teisseyre KP, Krajewski Z, Jaroszewicz LR. Rotational components of the seismic fields caused by local events. In: Mustafa A, editor. Earthquake Engineering—From Engineering Seismology to Optimal Seismic Design of Engineering Structures. 1st ed. Rijeka: InTech; 2015. pp. 163-188

Chapter 3

Inversion and Interpretation of Magnetic Anomaly in the Presence of Significant Remanence and Self-Demagnetization Based on Magnetic Amplitude

Shuang Liu and Xiangyun Hu

Additional information is available at the end of the chapter

http://dx.doi.org/10.5772/intechopen.71027

Abstract

Remanent magnetization and self-demagnetization effects of high-susceptibility body distort the intensity and direction of internal magnetization and hence complicate the inversion and interpretation of magnetic anomaly. The magnitude magnetic anomaly, which is weakly sensitive to the magnetization direction, provides an indirect way to investigate these complex anomalies. We study the sensitivity characteristics of 2D magnitude magnetic anomaly to magnetization direction and source shapes, implement the magnetization intensity inversion, and further estimate the magnetization direction by inverting for the total field data. The magnetic amplitude inversion is tested by the use of synthetic data, which are caused by prism models with strong remanent magnetization and high susceptibility. It is also applied to the field data of an iron-ore deposit in South Australia. The primary advantage of magnitude anomaly inversion is that the magnetization directions are not assumed to parallel the geomagnetic field. The magnetization intensity inversion and magnetization direction estimation make full use of the amplitude and phase information of magnetic anomalies. Magnetic amplitude inversion including other amplitude quantities such as normalized source strength and analytic signal offers an effective approach to investigate and interpret the magnetic anomalies affected by complicated remanence and self-demagnetization.

Keywords: magnetic anomaly, inversion and interpretation, remanent magnetization, self-demagnetization, magnetic amplitudes, mineral resources

1. Introduction

Susceptibility is the primary parameter used to represent the magnetic property of rocks and ores. Thus, numerous studies of magnetic data inversion were devoted to recover the

susceptibility distributions and to infer the positions and shapes of magnetic sources. For example, Li and Oldenburg presented the techniques of depth-weighted, wavelet-transform compression and joint inversion of surface and borehole magnetic data [1–3]; Pilkington utilized the preconditioned conjugate gradient algorithm to solve the matrix equation [4]; Portniaguine and Zhdanov presented the image focusing techniques based on the minimum gradient support functions [5, 6]; Fedi presented the depth from extreme point method based on upward continuation theory [7], and so on. Nonetheless, the remanent magnetization also is an important part of rocks' and ores' magnetic property. It originates from conditions at their time of formation and widely exists in many real examples. The remanence alters the strength and direction of internal magnetization and exhibits large extents of uncertainty and regionality, which complicates the interpretation of magnetic data. Apart from the remanence, the self-demagnetization effect of high-susceptibility field sources also changes the magnitude and direction of internal magnetization [8–11]. Inversion of magnetic anomaly in the presence of remanence and self-demagnetization has become a hot topic in recent years.

Some strategies have been proposed to deal with the remanence problem as Clark [12] summarized. The first kind of approach is to estimate the magnetization direction before recovering the physical property distributions using a standard magnetic inversion. The methods of estimating the magnetization direction are many. For example, Fedi et al. proposed the max-min method of reduced-to-the-pole (RTP) to obtain the magnetization direction [13]; Bilim and Ates estimated the magnetization direction by searching for the maximum correlation between pseudo-gravity and gravity anomalies [14]. Phillips used Helbig's integrals for estimating the vector components of the magnetic dipole moment from the first-order moments of the vector magnetic field components [15]. Nicolosi et al. computed the magnetization direction of crustal structures using an equivalent source algorithm [16]. Dannemiller and Li estimated the total magnetization direction based on the correlation between the vertical gradient and the total gradient of the RTP field [17]. Gerovska et al. inverted the magnetization direction by correlating RTP and the magnitude magnetic anomalies [18]. Li et al. estimated the magnetization direction of magnetic anomalies through the correlation between normalized source strength and RTP [19]. The above magnetization direction estimation approaches are more amenable for simple and isolated anomalies because usually a unique magnetization direction is achieved. Due to the fact that only an averaged magnetization direction can be achieved, the above methods are more applicable for some simple and isolated anomalies.

In addition, an alternative method is presented to directly invert for some kinds of amplitude anomalies which are low sensitive to magnetization directions such as the total gradient data [20], the magnitude magnetic anomaly [21–25], the normalized source strength [26–28], and the analytic signal [29, 30]. This approach is more effective when the magnetization direction is highly variable due to the factors such as structural changes. The third method is the magnetization vector inversion. Wang et al. recovered a three-component Cartesian magnetization model and inverted the three components of total magnetization. However, their approach was more applicable in determining the total magnetization of separated, homogeneous bodies [31]. Lelièvre and Oldenburg improved their methods and

calculated the three components of magnetization in a Cartesian and spherical framework, which served more complicated scenarios and had widespread applications in magnetic data inversion under the influences of significant remanent magnetization [32]. Similarly, Ellis et al. established the matrix equations between the magnetization components and magnetic anomalies and then optimized the objective function to obtain three components of magnetization vector [33]. These proposed methods were more applied to the inversion in the presence of remanence, but seldom used to invert the high-susceptibility distributions when the self-demagnetization effect is considered. Liu et al. inverted the 2D magnetization vector distributions of a high-susceptibility prism model based on the borehole magnitude magnetic anomalies [8].

The physical principles of self-demagnetization are different with remanence, but they have similar response in that both change the strength and direction of internal magnetization vectors. In cases where susceptibility of magnet is <0.1 SI, the effects of demagnetization are insignificant and can be neglected in forward modeling. However, such effects are important when modeling bodies with high susceptibility [11]. It is demonstrated that the self-demagnetization effect tends to reduce the magnitude and biases the direction of internal magnetization, thereby distorting the amplitudes and shapes of magnetic anomalies [34]. The self-demagnetization widely exists in magnetic exploration [10] and engineering prospecting [9, 35]. A large number of forward modeling studies in relation to self-demagnetization have been carried out [9, 36–50], but it is still difficult to invert the property distributions considering the implications of self-demagnetization. The earlier approaches dealing with this problem involve correcting the magnetic anomaly by the use of the demagnetization factors for some simple models such as the 3D sphere and 2D elliptic cylinder [10]. Obviously, this method is only suitable for some simple geological conditions. Being similar to the electrical methods, in addition, Lelièvre and Oldenburg directly solved the Maxwell's equations using a finite volume discretization to recover the 3D high susceptibility distributions [9]. This is an effective way to solve the self-demagnetization problem, but the algorithms for solving the partial differential equations are difficult to implement under the complicated boundary conditions and rugged topography. Krahenbuhl and Li proposed an amplitude inversion method, and the study gave good results under the influence of self-demagnetization at high magnetic susceptibility [35]. Liu et al. inverted the 2D magnetization magnitude and direction distributions of a high-susceptibility dike model using borehole magnetization vector inversion [8]. Krahenbuhl and Li implemented the inversion of multiple source bodies and complex structures exhibiting strong self-demagnetization based on the magnetic amplitude data [50].

Taking the 2D magnetic anomaly as an example, we discuss the characteristics of magnitude magnetic anomaly to magnetization direction and shapes of magnetic sources, and introduce the computations of magnitude magnetic anomaly in frequency domain. We recover the magnetization intensity distributions from the magnitude magnetic anomaly. Then, the total field anomalies are computed to estimate the magnetization direction. We simulate the magnetic field responses of high-susceptibility source under the self-demagnetization effect using the finite element method (FEM) and use the synthetic prism models with significant remanent

magnetization and high susceptibility to test the amplitude inversion, respectively. Finally, amplitude inversion is applied to the field data of an iron-ore deposit in Southern Australia.

2. Methodology

2.1. 2D magnitude magnetic anomaly

The magnitude magnetic anomaly (i.e., T_a) belongs to the magnitude transforms and has some differences compared with the total field anomaly (i.e., ΔT). The 2D magnitude magnetic anomaly is defined as

$$T_a = \left(H_{ax}^2 + Z_a^2\right)^{\frac{1}{2}}, \tag{1}$$

where H_{ax} and Z_a are the horizontal and vertical components of magnetic anomalies, respectively. Given that H_{ax} and Z_a anomalies satisfy the linear superposition principle, T_a can be added by anomalies from each magnetic cell numbered i:

$$T_a = \left[\left(\sum\nolimits_i H_{axi}\right)^2 + \left(\sum\nolimits_i Z_{ai}\right)^2\right]^{\frac{1}{2}}. \tag{2}$$

For single magnetic cell, the magnitude anomaly can be written as

$$T_{ai} = \left(H_{axi}^2 + Z_{ai}^2\right)^{\frac{1}{2}}. \tag{3}$$

Based on Eqs. (2) and (3), the following equation can be deduced:

$$T_a \leq \sum\nolimits_i T_{ai}\ , \tag{4}$$

which indicates that the magnitude magnetic anomaly, the first difference with total field, is nonlinear relative to the magnetization intensity. It complicates the forward modeling and inversion. For example, the magnitude magnetic anomalies cannot be computed by adding single mesh cell's anomalies. Also, their sensitivity matrix is more complex to calculate than that of total field anomalies.

According to the 2D Poisson formula of magnetic field, the horizontal and vertical component anomalies are given by:

$$\begin{cases} H_{ax} = \dfrac{\mu_0}{4\pi G\sigma}\left[M_x V_{xx} + M_z V_{zx}\right] \\ Z_a = \dfrac{\mu_0}{4\pi G\sigma}\left[M_x V_{xz} + M_z V_{zz}\right] \end{cases}, \tag{5}$$

where V is the gravitational potential. Thus, T_a can be written as

$$T_a = \left(H_{ax}^2 + Z_a^2\right)^{\frac{1}{2}} = \frac{\mu_0 M_s}{4\pi G\sigma}\left[V_{xx}^2 + V_{xz}^2\right]^{\frac{1}{2}} = \frac{\mu_0 M_s}{4\pi G\sigma}\left[V_{zz}^2 + V_{zx}^2\right]^{\frac{1}{2}}, \tag{6}$$

where $\frac{\mu_0 M_s}{4\pi G\sigma}$ is a constant, σ is the residual density, M_s is the effective magnetization intensity, and V_{xx}, V_{zz}, V_{xz}, and V_{zx} are the second-order partial derivatives of gravitational potential, none of which are dependent on the direction of magnetization. Eq. (6) demonstrates that the magnitude magnetic anomaly is not dependent on the magnetization orientation.

Figure 1 shows the examples of total field anomalies and magnitude magnetic anomalies of a rectangular prism model magnetized by different magnetization inclinations (i.e., $I = 0°$, $30°$, $60°$, $90°$, $135°$), of which the magnetization intensity is $M = 100$ A/m and geomagnetic inclination and declination are $I_0 = 45°$ and $D_0 = 0°$, respectively. For the different magnetization inclinations, the total field anomalies (colored solid lines) are different, but their corresponding magnitude magnetic anomalies (black solid line) are completely similar. In fact, the observed total field anomalies contain amplitude and phase information. The magnitude anomalies reflect their amplitude information, which is related to the intensity of magnetic bodies' magnetization or susceptibility. The phase information is related to the magnetization direction. Therefore, the primary advantage of using amplitude anomalies of total field anomalies to invert the magnetization intensity or susceptibility distributions is that it is not essential to input the magnetization inclination or not to assume the magnetization inclination paralleling the Earth's magnetic field.

Besides, the magnitude magnetic anomalies show better discrimination to the occurrences of the magnetic bodies. As for tabular models with different inclinations, the shapes of magnitude magnetic anomalies are different. In **Figure 2**, the magnitude anomalies of vertical tabular bodies (i.e., $\alpha = 90°$) are symmetrical with similar decrease rate at the two sides of the anomalies. As for dipping tabular bodies with inclinations $\alpha = 15°$, $30°$, $45°$, $60°$ and $75°$, the magnitude anomalies at inclined direction decrease slightly, while they are steep at another direction. Therefore, the magnitude magnetic anomalies are conveniently utilized to preliminarily determine the inclined direction of magnetic bodies.

Overall, magnitude magnetic anomaly has two advantages. First, it does not depend on the magnetization direction. The magnitude anomaly has the approximate resolution to recover

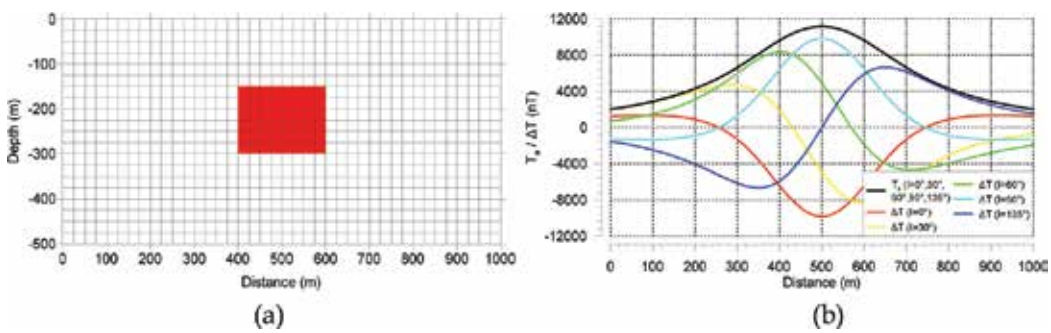

Figure 1. (a) The rectangular prism model (b) corresponding total field anomalies and magnitude magnetic anomalies.

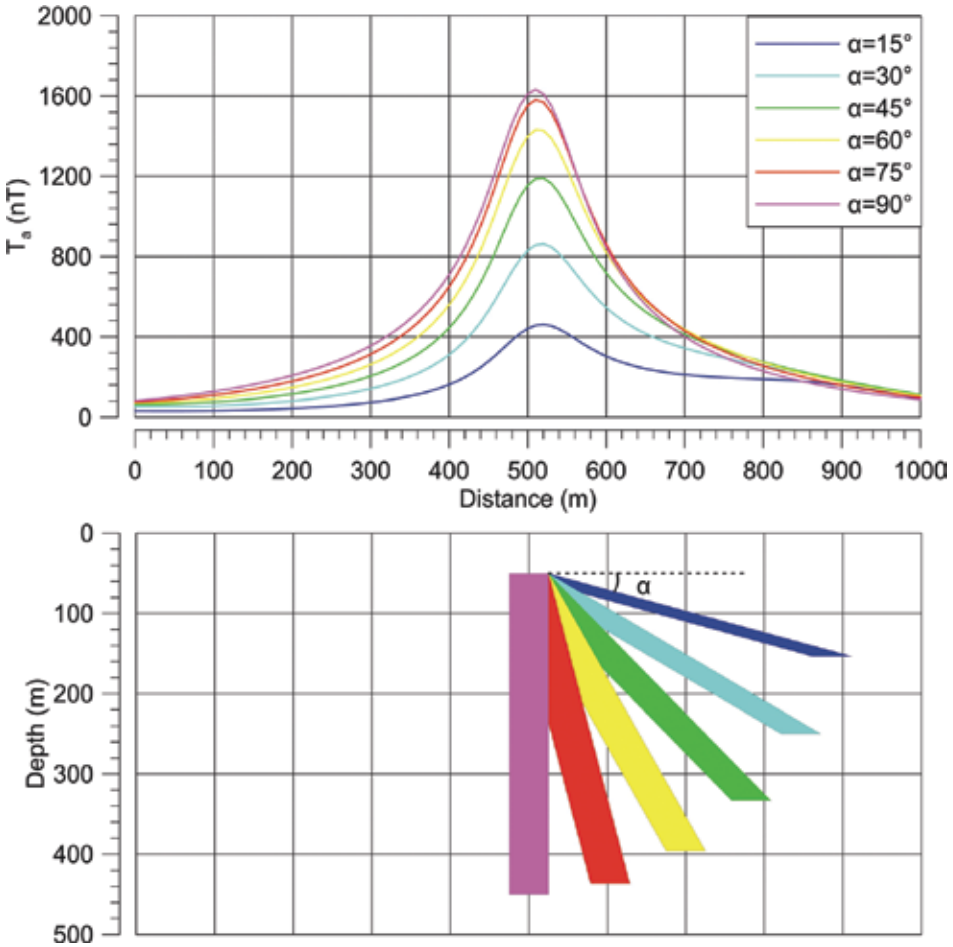

Figure 2. The magnitude magnetic anomalies of the dipping prisms with different inclinations.

the magnetic sources as total field anomaly. Second, magnitude anomaly performs more accurately in estimating the occurrence of magnetic bodies. Owing to the influences of inclined magnetization, it is difficult to determine the dipping direction using total field anomaly.

2.2. Computation of magnitude magnetic anomaly

Magnitude magnetic anomaly (i.e., T_a) belongs to the transformed quantity which is computed from observed total field anomaly (i.e., ΔT) in frequency domain [51]. Initially, we calculate the frequency spectrum of ΔT by implementing fast Fourier transform (FFT):

$$\Delta T \xrightarrow{FFT} \mathcal{F}_{\Delta T}, \tag{7}$$

where $\mathcal{F}_{\Delta T}$ represents the frequency spectrum of ΔT. Then, the frequency spectrums of horizontal and vertical components (i.e., H_{ax} and Z_a) are achieved by, respectively, multiplying a transformed factor on the ΔT frequency spectrum:

$$\mathcal{F}_{H_{ax}} = \omega_{\Delta T \to H_{ax}} \mathcal{F}_{\Delta T}, \tag{8}$$

and

$$\mathcal{F}_{Z_a} = \omega_{\Delta T \to Z_a} \mathcal{F}_{\Delta T}, \tag{9}$$

where $\mathcal{F}_{H_{ax}}$ and $\mathcal{F}_{Z_a}$ are the frequency spectrums of H_{ax} and Z_a components; $\omega_{\Delta T \to H_{ax}}$ and $\omega_{\Delta T \to Z_a}$ are the frequency factors transforming ΔT to H_{ax} and Z_a components and expressed as:

$$\omega_{\Delta T \to H_{ax}}(\kappa) = \frac{i}{sinI_0 + icosI_0 cosA_0}, \tag{10}$$

and

$$\omega_{\Delta T \to Z_a}(\kappa) = \frac{1}{sinI_0 + icosI_0 cosA_0}, \tag{11}$$

where I_0 and A_0 denote the inclination of the Earth's magnetic field and the azimuth of profile, and i is the imaginary number. Hence, the horizontal and vertical component anomalies are obtained by carrying out the inverse frequent Fourier transform (IFFT):

$$\mathcal{F}_{H_{ax}} \xrightarrow{IFFT} H_{ax}, \tag{12}$$

and

$$\mathcal{F}_{Z_a} \xrightarrow{IFFT} Z_a. \tag{13}$$

After obtaining the H_{ax} and Z_a components, the magnitude anomalies are computed by the use of Eq. (1).

Eqs. (7)–(13) summarize the calculation processes of magnitude magnetic anomaly. The critical processes are based on the computations of H_{ax} and Z_a components in frequency domain. Regardless of geomagnetic inclination and profile's azimuth, it does not need inputting another parameter during the whole calculation processes.

2.3. Magnetization intensity inversion

Eq. (4) indicates that the magnitude magnetic anomaly vector $\mathbf{T}_a$ is nonlinearly related to the magnetization intensity vector $\mathbf{m}$. Their relation is given by

$$\mathbf{T}_a = T_a(\mathbf{m}) \tag{14}$$

where $T_a(\mathbf{m})$ is a nonlinear function. Using first-order Taylor expansions on Eq. (14), we obtain the following matrix equation:

$$\Delta \mathbf{T}_a = \mathbf{J}_{T_a} \Delta \mathbf{m} \tag{15}$$

where $\Delta\mathbf{T}_a$ and $\Delta\mathbf{m}$ are corrections of $\mathbf{T}_a$ and $\mathbf{m}$, respectively, and $\mathbf{J}_{T_a}$ is named sensitivity matrix whose element $J_{T_a(i,j)}$ is the partial derivative of T_a at the ith observation point to the jth model parameter m_j [23]. Thus,

$$J_{T_a(i,j)} = \frac{\partial T_{ai}}{\partial m_j} = \frac{\partial}{\partial m_j}\left(H_{axi}^2 + Z_{ai}^2\right)^{\frac{1}{2}} = \frac{1}{T_{ai}}\left(H_{axi}G_{H_{ax(i,j)}} + Z_{ai}G_{Z_{a(i,j)}}\right), \tag{16}$$

where i ($i = 1,2,\ldots,m$) denotes the ith observation point, j ($j = 1,2,\ldots,n$) denotes the jth mesh cell, m and n are the total numbers of observation points and mesh cells, respectively, and $G_{H_{ax(i,j)}}$ and $G_{Z_{a(i,j)}}$ are the elements of $\boldsymbol{G}_{H_{ax}}$ and $\boldsymbol{G}_{Z_a}$. Here, $\boldsymbol{G}_{H_{ax}}$ and $\boldsymbol{G}_{Z_a}$ are the constant sensitivity matrices of H_{ax} and Z_a anomalies. This equation demonstrates that because of the nonlinearity relation between magnitude anomalies and magnetization intensity, it is more complicated to compute the sensitive matrix of T_a than that of H_{ax}, Z_a, and ΔT anomalies. The sensitivity matrix of T_a is related to the sensitive matrices of H_{ax}, Z_a and the calculated H_{ax}, Z_a, and T_a anomalies.

The minimum error solution of Eq. (15) is equivalent to solving the symmetric positive definite equation:

$$\mathbf{J}_{T_a}^T\mathbf{J}_{T_a}\Delta\mathbf{m} = \mathbf{J}_{T_a}^T\Delta\mathbf{T}_a. \tag{17}$$

We multiply a matrix $\mathbf{P}$ at both sides of Eq. (17); hence,

$$\mathbf{P}\left(\mathbf{J}_{T_a}^T\mathbf{J}_{T_a}\Delta\mathbf{m}\right) = \mathbf{P}\left(\mathbf{J}_{T_a}^T\Delta\mathbf{T}_a\right), \tag{18}$$

where $\mathbf{P}$ usually is a diagonal matrix named preconditioner, which is used to reduce the condition number of Eq. (17) and promote the convergence rate. When Pilkington [4] and Liu et al. [8] used preconditioned conjugate gradient method to invert the magnetic anomaly, the preconditioner is given by.

$$\mathbf{P} = z^{\beta}\mathbf{I}, \tag{19}$$

where z is the buried depth of mesh cells, β is a constant related to the magnetic anomalies' attenuation rate with the increase of distances between cells and observation point, and $\mathbf{I}$ is the unit matrix.

2.4. Estimation of effective magnetization direction

After obtaining the magnetization intensity distributions, we can regard them as known information and then calculate the total field anomalies using different magnetization directions. Thus, if the magnetization direction is given appropriately, the computed total field anomalies should fit the observed total field anomalies and their correlation coefficients get to maximum. Therefore, we compute the correlation coefficients between the observed and predicted total field anomalies of which the magnetization inclinations rotate a cycle from 0 to 360° with a certain step:

$$R(I) = \frac{C\left[\Delta T^{obs}, \Delta T^{pre}\right]}{\sqrt{C\left[\Delta T^{obs}, \Delta T^{obs}\right] C[\Delta T^{pre}, \Delta T^{pre}]}} \quad \left(0^{\circ} \le I \le 360^{\circ}\right), \tag{20}$$

where I is the magnetization inclination, $R(I)$ is the correlation coefficient between observed and predicted total field anomalies, ΔT^{obs} is the observed total field anomalies, ΔT^{pre} is the predicted total field anomalies when the magnetization inclination is set to be I, and $C\left[\Delta T^{obs}, \Delta T^{obs}\right]$, $C[\Delta T^{pre}, \Delta T^{pre}]$ are the covariance of observed and predicted data, $C\left[\Delta T^{obs}, \Delta T^{pre}\right]$ is the cross-covariance between observed and predicted data. Therefore, the most appropriate magnetization inclination is that when the correlation coefficients of Eq. (20) get to the maximal values, it can be expressed as,

$$I_{\text{best}} = \arg\ max[R(I)]. \tag{21}$$

Eqs. (20) and (21) are the principle formulas used to estimate the magnetization direction. Based on the recovered magnetization distributions, we calculate the predicted magnetic anomalies magnetized by different magnetization inclinations varied from 0 to 360°. The magnetization inclination with the largest correlation coefficients between the observed and predicted anomalies is defined as the most appropriate magnetization direction. In essence, the method makes use of the phase information of total field anomalies to determine the magnetization direction.

3. Synthetic examples: magnetic amplitude inversion with significant remanence

3.1. Rectangular prism with different magnetization inclinations

We firstly test the method by the use of the 2D rectangular prism in **Figure 1a**, of which the top buried depth is 150 m and the length and width are 150 and 200 m, respectively. The Earth's magnetic field intensity is T_0 = 50,000 nT, with inclination $I_0 = 45^{\circ}$ and declination $D_0 = 0^{\circ}$. The rectangular prism is magnetized by a constant magnetization with intensity M = 100 A/m and declination $D = 0^{\circ}$, but the magnetization inclinations are assumed to be $I = 0^{\circ}$, 30°, 45°, 60°, 90°, and 135° under influence of remanent magnetization. The magnetic observation point spacing is 20 m, and there are 51 points in total. As shown in **Figure 1b**, the total field anomalies are changed for different magnetization inclinations. However, for different magnetization inclinations varied from 0 to 135°, their amplitude anomalies always are the black solid line of the **Figure 1b**. The 2D amplitude data are strictly invariant with the magnetization direction. Therefore, using the amplitude anomalies to recover the magnetization, intensity distributions reduces the errors resulting from the incorrect magnetization direction. When inverting for the total field data, it is necessary to input the correct magnetization direction.

We invert for the amplitude data of the rectangular prism model in **Figure 1b**. The subsurface is divided into 800 (20 rows × 40 columns) mesh cells with size of 25 × 25 m. The

preconditioned conjugate gradient algorithm converges stably after hundreds of iterations, and the predicted amplitude data accurately fit the observed data. The recovered magnetization distributions including the position and shape of magnetic sources yield a good approximation with the true model (**Figure 3a**). The magnitude anomalies show similar resolution to the recovery of physical property distributions compared with the total field anomalies (**Figure 3b**).

With the known magnetization intensity distribution of **Figure 3a**, subsequently, the total field anomalies are computed of which the magnetization inclinations are varied a cycle from 0 to 360° by a step of 0.5°. Then, we calculate the correlations between the observed and predicted total field anomalies for each magnetization inclination. As shown in **Figure 4**, the six colored solid lines, respectively, represent the correlation curves of the six synthetic magnetization inclinations (i.e., I = 0°, 30°, 45°, 60°, 90°, and 135°), of which the horizontal and vertical axes denote the magnetization inclination and the value of correlation. The correlation curve fluctuates between −1 and 1 shaped as the sine or cosine function. Each curve has one maximum

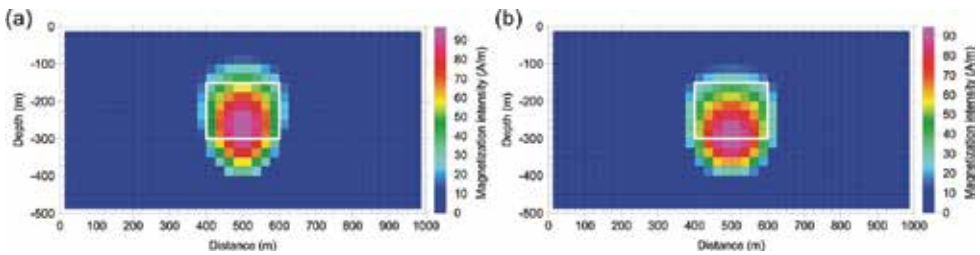

Figure 3. The magnetization intensity inversion results of the rectangular model using (a) magnitude magnetic anomalies and (b) total field anomalies.

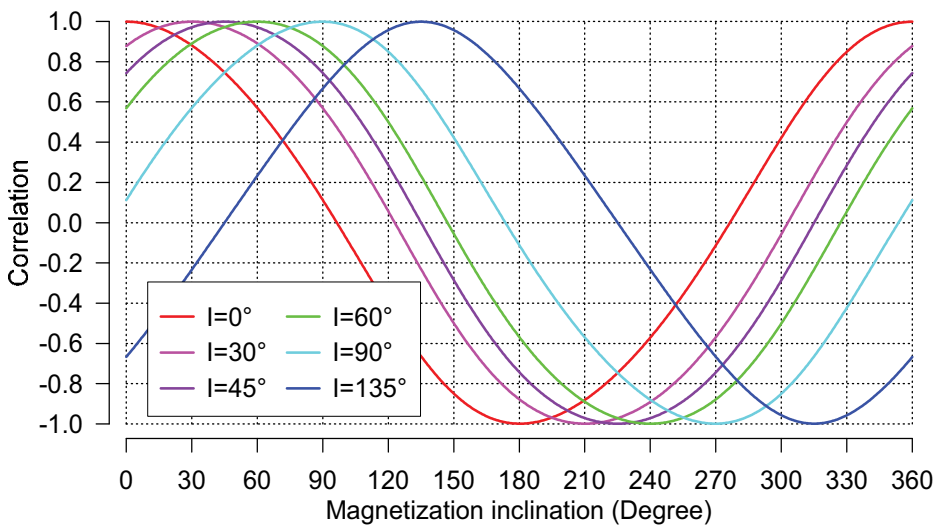

Figure 4. The correlation curves of the rectangular model with different magnetization inclinations. The positions of maximal values reflect the magnetization directions.

point, and the position of the maximum point represents the optimal magnetization direction. For example, for the red solid curve when the magnetization direction is horizontal (i.e., $I = 0°$), the maximal peak locates at $I = 0.5°$ with maximal correlation $R = 0.9986$, and therefore, the estimated optimal magnetization is $I_{best} = 0.5°$. The results of magnetization direction determination for the six synthetic magnetization inclinations are shown in **Table 1**. The synthetic magnetization inclinations are 0°, 30°, 45°, 60°, 90°, and 135°, and their corresponding estimated magnetization inclinations are 0.5°, 30.0°, 45.0°, 60.0°, 90.0°, and 135.0°. The maximal correlations resulted to 0.9986. The estimated magnetization inclinations are in agreement with the true values (error < 0.5°).

3.2. Complicated prisms with the same magnetization inclination

We design four 2D prism models, of which the cross sections are the dipping tabular, syncline tabular, cut tabular, and reproduction tabular (**Figure 5**). The Earth's magnetic field intensity is $T_0 = 50{,}000$ nT, with inclination $I_0 = 45°$ and declination $D_0 = 0°$. The models are magnetized by a constant magnetization magnitude $M = 100$ A/m with inclination $I = 60°$ and declination $D = 0°$. The magnetic observation point spacing is 20 m, and there are 51 points in total. The observed total field anomalies and the transformed magnitude anomalies are shown in **Figure 6**. Being similar to amplitude inversion of the **Figure 3**, the subsurface is divided into

Synthetic (degree)	0	30	45	60	90	135
Estimated (degree)	0.5	30.0	45.0	60.0	90.0	135.0
Correlation	0.9987	0.9987	0.9988	0.9987	0.9987	0.9986

Table 1. The estimated magnetization inclinations for rectangular model using correlation method.

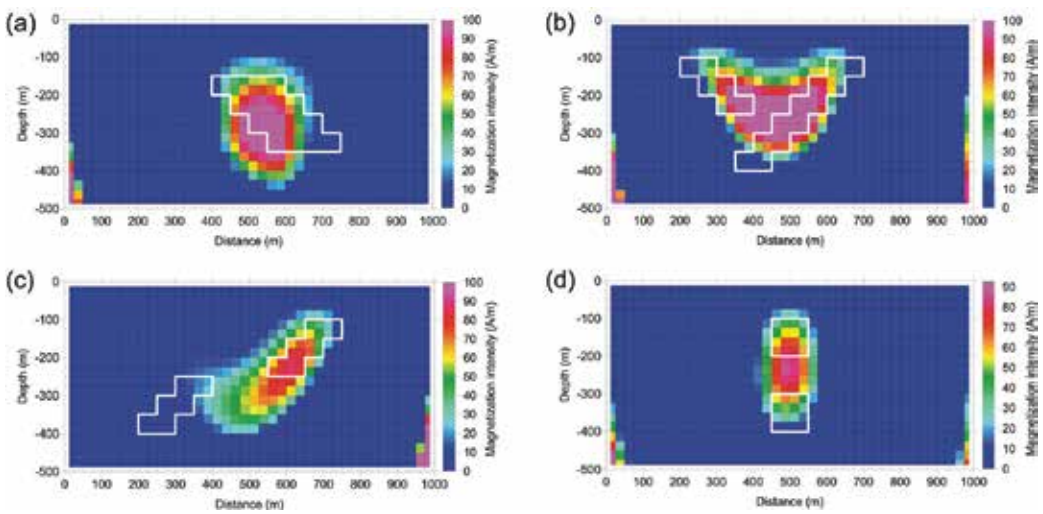

Figure 5. The magnetization intensity inversion results using magnitude magnetic anomalies for the synthetic prism model: (a) dipping prism, (b) syncline prism, (c) cut prism, and (d) reproduction prism.

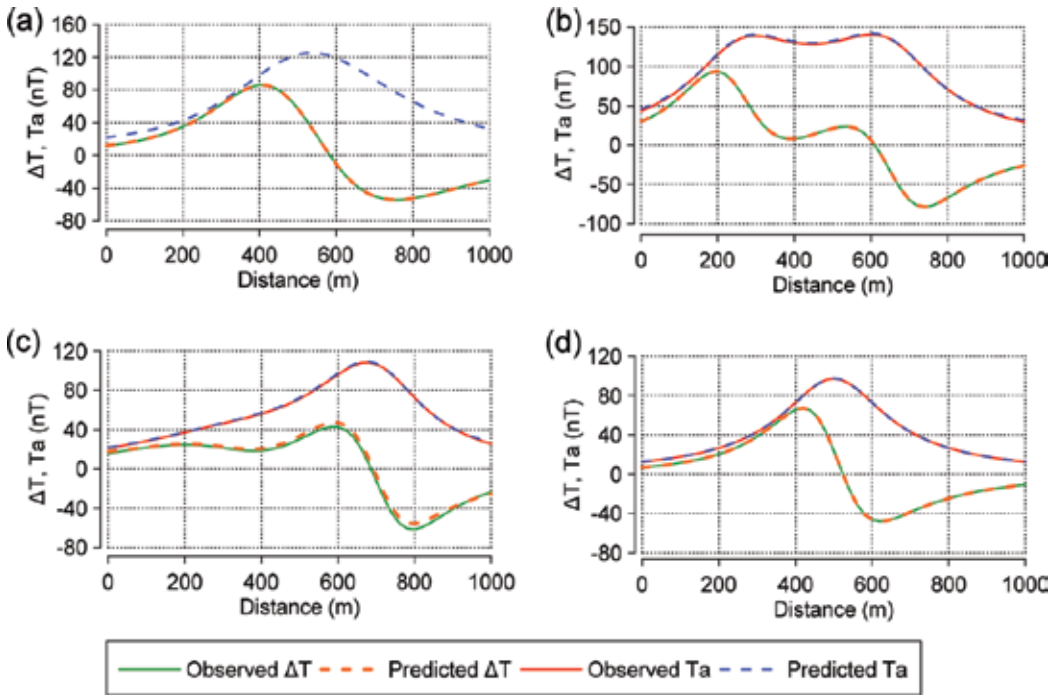

Figure 6. The observed and predicted total field anomalies and magnitude magnetic anomalies of the synthetic prism models: (a) dipping prism, (b) syncline prism, (c) cut prism, and (d) reproduction prism.

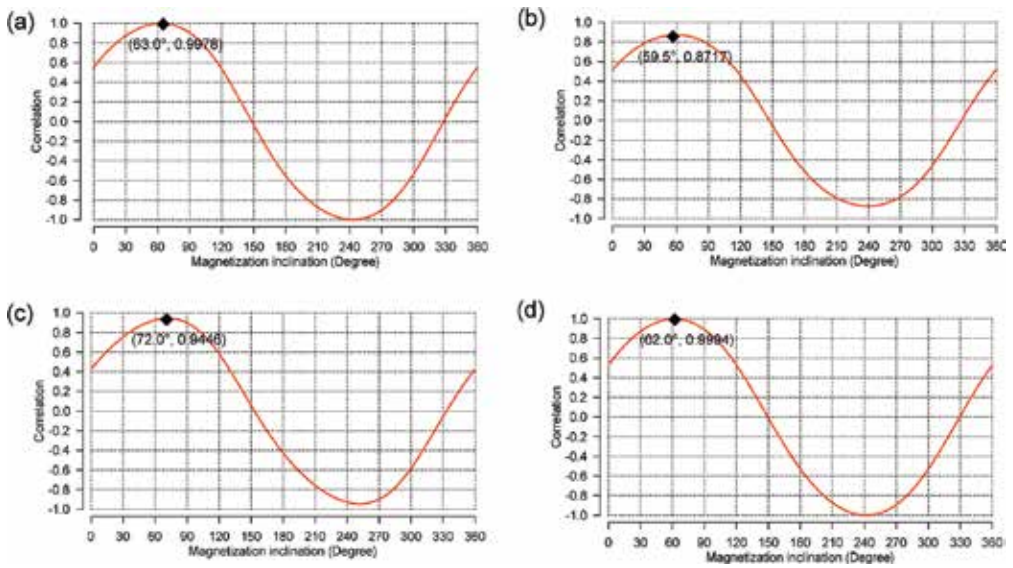

Figure 7. The correlation coefficient curves and the computed magnetization directions of the synthetic prism model: (a) dipping prism, (b) syncline prism, (c) cut prism, and (d) reproduction prism.

800 (20 rows × 40 columns) rectangular cells. The preconditioned conjugate gradient converges after 100 iterations on average, and simultaneously, the predicted magnitude anomalies accurately fit the observed magnitude data (**Figure 7**). The recovered magnetization intensity distributions are shown in **Figure 5**. The inversion results are basically in accordance with the synthetic models. Owing to the lower resolution due to deep-buried magnetic sources, the deeper sources of combinational models including the cut prisms (**Figure 5c**) and reproduction prisms (**Figure 5d**) are not clearly distinguished.

After recovering the magnetization intensity distributions (**Figure 5**), we estimated the magnetization directions based on the known magnetization intensity distributions. The correlation curves and the estimated magnetization inclination are shown in **Figure 7** and **Table 2**. Except the syncline prism model with error of 12°, other determined magnetization inclinations are close to 60°. The amplitude data do not clearly distinguish the closed magnetic bodies leading to the predicted total field data not fitting the observed total field data accurately for combinational syncline and cut prisms. Besides, compared with the traditional correlation methods for estimating the magnetization direction [14, 15–18], this method considers magnetic sources' shapes and positions, which improves the precision of magnetization direction determination.

Model	a	B	c	D
Synthetic (degree)	60	60	60	60
Estimated (degree)	63.0	59.5	72.0	62.0
Correlation	0.9978	0.8717	0.9446	0.9994

Table 2. The magnetization inclination determination results for four prism models: (a) dipping prism, (b) syncline prism, (c) cut prism, and (d) reproduction prism.

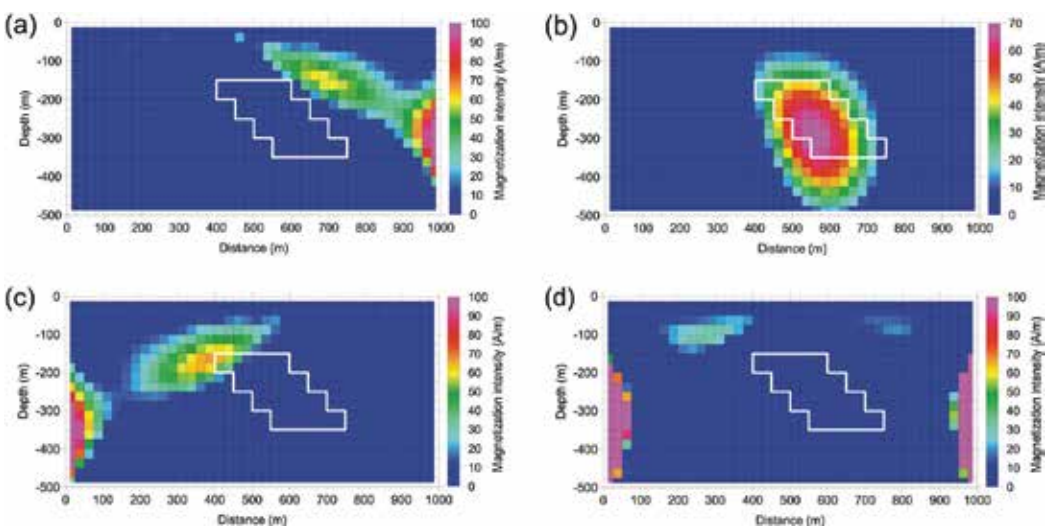

Figure 8. The magnetization intensity inversion results for the total field anomalies of the dipping prism model using different magnetization inclinations: (a) I = 0°, (b) I = 45°, (c) I = 90°, and (d) I = 135°.

Taking the dipping prism as an example, we invert for the magnetization distributions from total field anomalies (true magnetization inclination is 45°) by giving different magnetization inclinations (i.e., I = 0°, 45°, 90°, 135°), assuming that we do not know the real magnetization direction of prism model. Only when the magnetization direction is given to be correct (true magnetization inclination is I = 45°), the inversion results coincide with the true model (**Figure 8b**). Otherwise, the inversion results have large errors compared with the true model (**Figure 8a**, **c**, and **d**). And even some of the iterations cannot be converged. Therefore, it is essential to give the correct magnetization inclination when using total field anomalies to recover the magnetization distributions. Otherwise, the inversion results may be distorted by the inaccurate magnetization direction.

4. Field examples: Brennand iron-ore deposit, Eyre peninsula, South Australia

The Brennand iron-ore deposit lies in the Eyre Peninsula, South Australia, located at longitude: 135° 52′ 00″ E and latitude: 34° 24′ 00″ S. The banded iron formation (BIF) ore bodies have high magnetic susceptibility and produce strong magnetic anomalies. The aeromagnetic anomalies

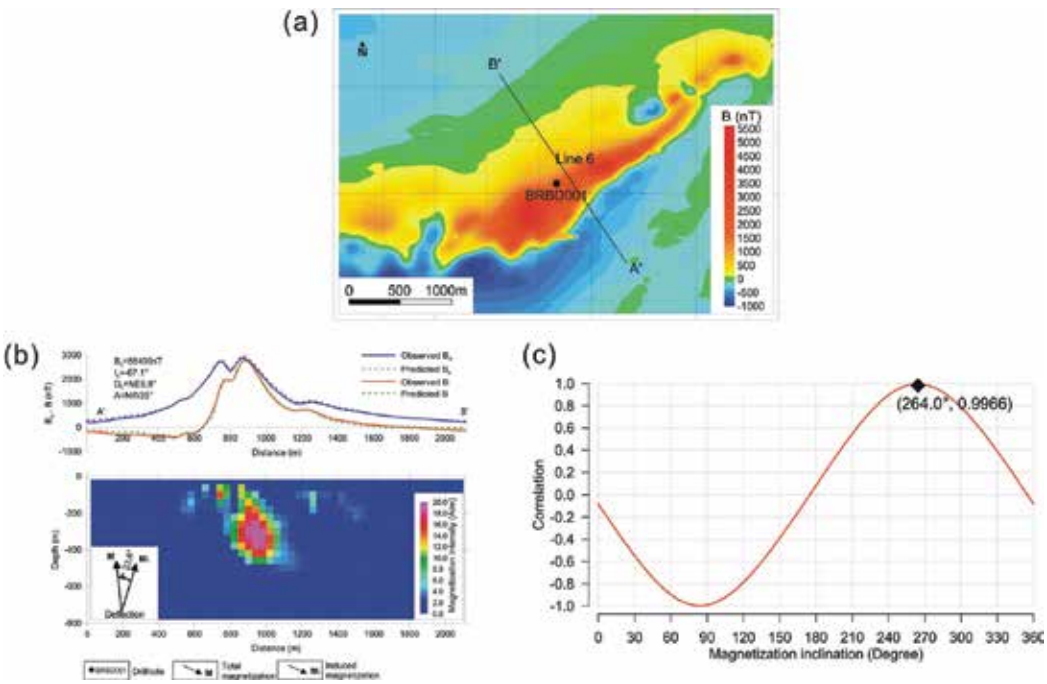

Figure 9. The magnetization intensity and direction inversion results for the Line 6 of the Brennand iron-ore deposit, Eyre Peninsula, South Australia: (a) the contour map of total field anomalies, (b) the recovered magnetization intensity distributions, and (c) the estimated magnetization direction.

strike northeast-southwest direction with amplitudes from −1000 to 5000 nT (**Figure 9a**). We use the data of Line 6 that traverses the center of mining area to test the method. The point spacing of this profile is 20 m, and there are 107 observation points in total.

First, we divided the subsurface into 1060 (20 rows × 53 columns) square cells with size of 40 m. The recovered magnetization intensity distributions indicate that the magnetic bodies are inclined to northwest about 60° and extend downward around 300 m (**Figure 9b**). Besides, the correlation curve demonstrates that the magnetization inclination is 264.0° (**Figure 9c**). The declination and inclination of the Earth's magnetic field in the mining area are NE6.8° and −67.1°. In the profile of Line 6, the effective magnetization inclination increases to −72.4°. Therefore, the magnetization direction deflects 23.6° (i.e., 360–264 − 72.4°) from Earth's magnetic field.

5. Synthetic example: magnetic amplitude inversion of high-susceptibility body

We design a 2D dike model with high susceptibility = 10.0 SI, of which the four vertices' coordinates are A (350–300 m), B (450–300 m), C (550–100 m), and D (450–100 m) (**Figure 10**). The geomagnetic field intensity is T_0 = 50,000 nT with an inclination of 45°. First, the finite element method (FEM) is used to simulate the surface total field anomalies (i.e., ΔT), the

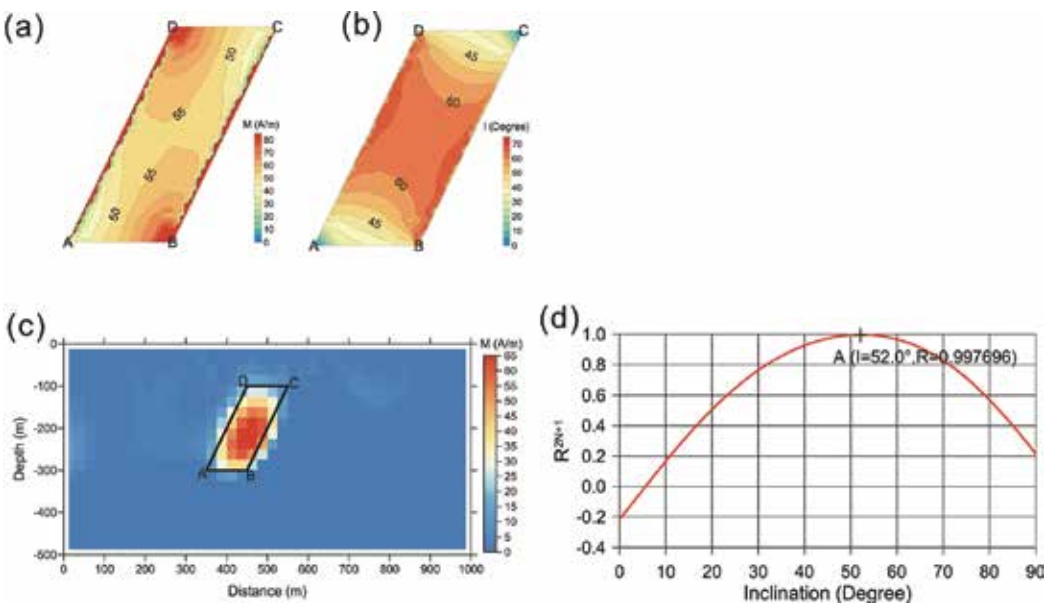

Figure 10. The magnetization inversion results of the high-susceptibility (κ = 10.0 SI) dike model: (a) the real internal magnetization intensity, (b) direction distributions when the self-demagnetization effect is not negligible, (c) the inverted magnetization intensity distributions using magnetic amplitude inversion, and (d) the estimated magnetization inclination using correlation coefficient method.

magnitude magnetic anomaly (i.e., T_a), the true internal magnetization intensity, and the inclination distributions. Theoretical simulation reveals that the internal magnetization distribution is inhomogeneous with average strength (50–60 A/m) (**Figure 10a**), which is far less than 397 A/m (i.e., $M = \kappa H_0 = \kappa T_0/\mu_0$) when demagnetization is not considered. The self-demagnetization effect decreases the internal magnetization intensity. Moreover, the internal magnetization inclination ranges from 50 to 65° with average of 60° (**Figure 10b**). The self-demagnetization effect deflects the magnetization direction about 15° (i.e., 60–45°) to the long-axis direction of the dike model. The computed total field anomaly and magnitude anomaly are shown with red and blue solid curves in **Figure 11**. The point spacing is 3 m.

We inverted for the magnitude magnetic anomaly (i.e., blue curve in **Figure 11**), and the cross section was divided into 40 × 20 square cells with size of 25 m. The preconditioned conjugate gradient method was converged after 200 times of iterations, and the predicted magnitude anomaly fit the observed anomaly accurately (**Figure 11**). The inverted magnetization intensity distributions are shown in **Figure 10c**. The range of the inverted magnetization intensity is (40–65 A/m), of which the amplitudes and shapes are in accordance with the real distribution of magnetization in the presence of demagnetization (**Figure 10a**). The correlation coefficients (with step of 0.2° varied from 0 to 90°) between the observed and predicted data reach the maximum at A (I = 52.0°, R = 0. 997,696). Hence, for this high-susceptibility prism, the estimated internal magnetization inclination is 52° (**Figure 10d**). This result is in good agreement with the theoretical distributions of magnetization inclination (**Figure 10b**). Therefore, from the magnetization vector inversion results, it can be concluded that the demagnetization effect biases the magnetization direction to the dike's long-axis direction 7° (i.e., 52–45°). They reduce the magnetization intensity and magnetic anomalies by about seven times (i.e., 397/60). The relative error of magnetic anomalies caused by demagnetization effects reaches 85% (i.e., (397–60)/397). Theoretically, for high-susceptibility magnetic bodies of which the susceptibility is 10 SI, the magnetic anomalies' error caused by demagnetization effects reaches 83% [8].

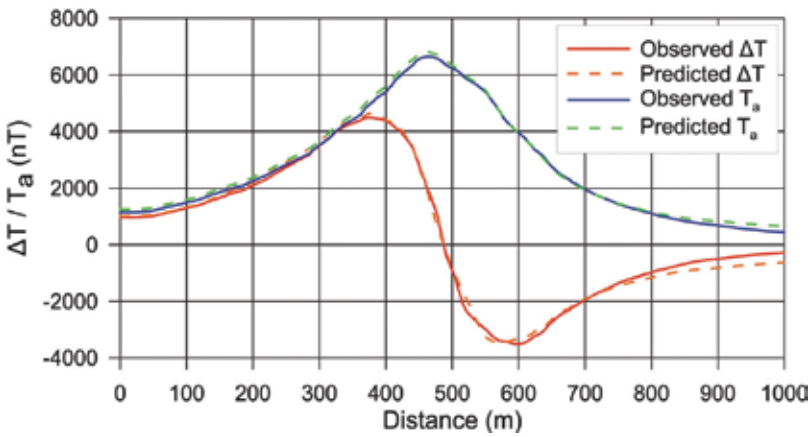

Figure 11. The observed and predicted total field anomalies and magnitude magnetic anomalies.

6. Weak sensitivity of 3D magnitude magnetic anomaly to magnetization direction

The 2D magnitude magnetic anomaly is totally independent of the magnetization direction and has high centricity with the magnetic source's position, which provides an idea of magnitude magnetic transform to investigate the inversion and interpretation of magnetic anomaly [21, 52]. For 3D cases, magnitude magnetic anomaly is written as

$$T_a = \left(H_{ax}^2 + H_{ay}^2 + Z_a^2\right)^{\frac{1}{2}}, \tag{22}$$

Which, however, has low sensitivity to the direction of magnetization. Stavrev and Gerovska [52] and Pilkington and Beiki [26] used a variable to evaluate the sensitivity of magnitude magnetic transform to magnetization direction by comparing with the field of vertical magnetization direction, expressed as

$$S(I,D) = \iint |F(I,D) - F(I_b,D_b)|dxdy / \iint |F(I_b,D_b)|dxdy, \tag{23}$$

where F is the magnitude magnetic transform; I and D are inclination and declination of magnetization direction, respectively; $I_b = 90^\circ$ and $D_b = 90^\circ$.

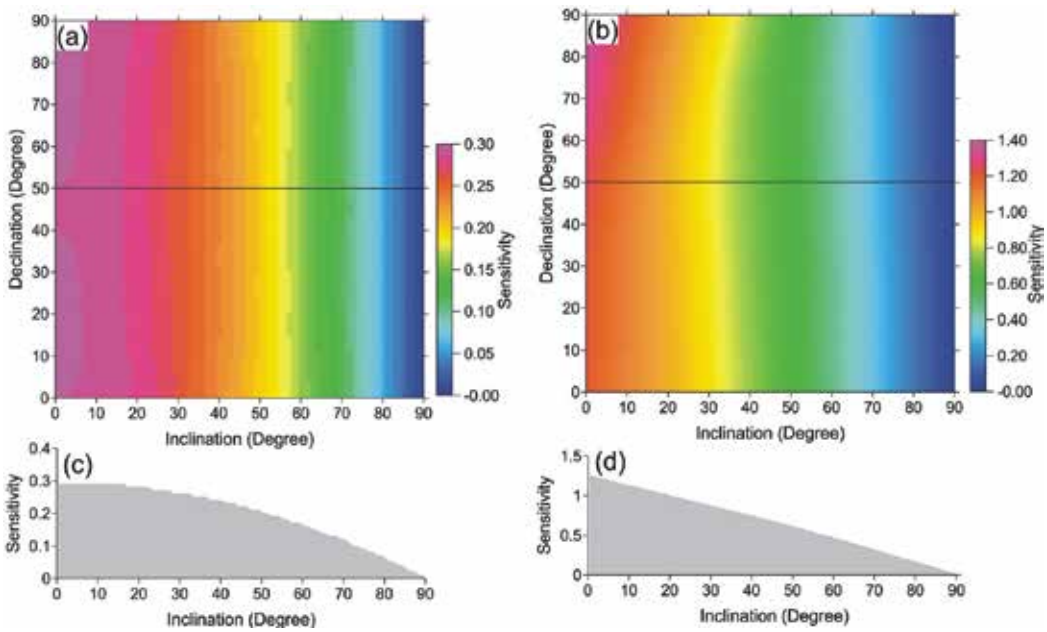

Figure 12. Sensitivities of (a, c) magnitude magnetic anomaly and (b, d) total field anomaly to the total magnetization direction. Plot (a) shows the sensitivity of magnitude magnetic anomaly to magnetization inclination and declination. Plot (b) shows the sensitivity of total field anomaly to magnetization inclination and declination. Plot (c) shows the sensitivity of magnitude magnetic anomaly to magnetization inclination (i.e., cross section at declination = 50° in plot (a)). Plot (d) shows the sensitivity of total field anomaly to magnetization inclination (i.e., cross section at declination = 50° in plot (b)).

Figure 12 shows the sensitivities of magnitude magnetic anomaly and total field anomaly to the magnetization inclination and declination. It is revealed that both the magnitude magnetic anomaly and total field anomaly are mainly sensitive to magnetization inclination. And the

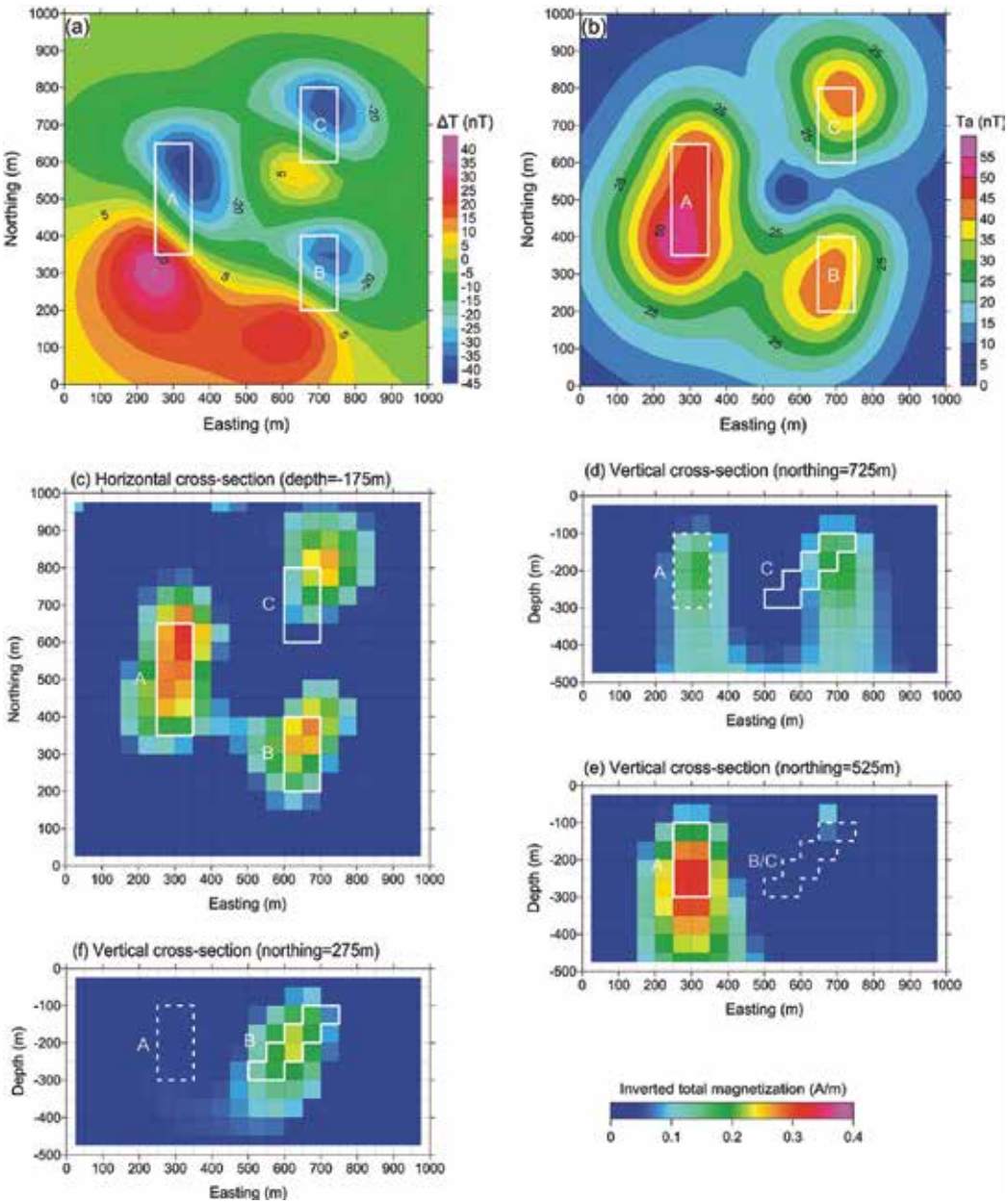

Figure 13. Magnetization inversion results of magnitude magnetic anomaly of a 3D synthetic model with horizontal total magnetization direction: (a) total field anomaly, (b) magnitude magnetic anomaly, (c) horizontal cross section at depth = −175 m, and vertical cross sections at northing = (d) 725 m, (e) 525 m, and (f) 275 m.

magnitude magnetic anomaly shows far weaker sensitivity than total field. The sensitivity value in Eq. (23) of total field is up to 1.3 when the magnetization direction is horizontal, while it is only 0.3 for magnitude magnetic anomaly. When the magnetization direction is horizontal, for magnitude magnetic data and total field data, the sensitivity reaches a maximal value.

The weak sensitivity feature of 3D magnitude magnetic anomaly to magnetization direction impacts the magnetization intensity inversion results. **Figure 13a** and **b** shows the total field anomaly and magnitude magnetic anomaly of the 3D synthetic model when the total magnetization direction is horizontal (magnetization intensity M = 1 A/m, inclination $I = 0°$, declination = 30°; geomagnetic inclination $I_0 = 45°$, declination $D_0 = 0°$). The total fields include positive and negative anomalies showing a relatively complicated feature. The magnitude magnetic anomaly only has positive values, and its extreme points show some offsets from the horizontal centers of magnetic source (**Figure 13b**). When inverting the magnitude magnetic anomaly, as shown in **Figure 13(c–f)**, the recovered magnetization distributions also have some offsets to north compared with the true models. The deep shapes of recovered magnetization intensity distributions in particularly for sources A and C have big differences with the true models, which also would increase the error of magnetization direction estimation.

7. Conclusions

Remanent magnetization is prevalent in many mining areas, but their directions usually are unknown because of the difficulty in collecting the oriented samples. For high-susceptibility source, the influence of self-demagnetization effect also cannot be ignored. The magnitude anomalies are frequently transformed from the observed total field anomalies. The primary advantage of magnitude anomalies inversion is that the magnetization directions are not assumed to parallel the geomagnetic field, or it is not necessary to input the magnetization directions as the total field data inversion. The magnitude anomalies have similar resolution to the recovery of physical property distributions and perform higher sensitivity to the occurrences of magnetic bodies compared with the total field anomaly. Based on the known magnetization intensity distributions, the total field anomalies are computed by the use of different magnetization directions. Thus, the magnetization direction of maximal correlation with the observed total field anomaly is deemed as the most appropriate magnetization direction. This strategy considers the influences of magnetic sources' shapes and obtains an average magnetization direction compared with another correlation approaches. The inverted magnetization intensity and direction help to study the influences of remanence and self-demagnetization. The method makes full use of the amplitude and phase information of total field anomaly to determine the magnetization intensity and direction, respectively. The amplitude anomaly is more related to the intensity of magnetization vector, while the phase is mainly dependent on the direction of magnetization vector. The 2D magnitude magnetic anomaly provides an idea of magnitude magnetic transform to implement the amplitude data inversion, but in 3D case, magnitude magnetic anomaly is weakly sensitive to magnetization direction, which brings some errors for the inversion of magnetization intensity. Other magnetic anomaly quantities such as analytic signal and normalized source strength have weak sensitivity to magnetization

direction, so they also can be inverted to study the remanent magnetization and self-demagnetization. The amplitude data inversion provides an effective approach to investigate the complex remanence and self-demagnetization.

Acknowledgements

This work was financially supported by the National Natural Sciences Foundation of China (41604087, 41630317), the Natural Sciences Foundation of Hubei Province (2016CFB122), the China Postdoctoral Science Foundation (2016M590132), and the Fundamental Research Funds for the Central Universities, China University of Geosciences (Wuhan) (CUGL170407, CUG160609).

Author details

Shuang Liu* and Xiangyun Hu

*Address all correspondence to: lius@cug.edu.cn

Institute of Geophysics and Geomatics, China University of Geosciences (Wuhan), Wuhan, China

References

[1] Li Y, Oldenburg DW. Fast inversion of large-scale magnetic data using wavelet transforms and a logarithmic barrier method. Geophysical Journal International. 2003;**152**(2): 251-265

[2] Li Y, Oldenburg DW. Joint inversion of surface and three-component borehole magnetic data. Geophysics. 2000;**65**(2):540-552

[3] Li Y, Oldenburg DW. 3-D inversion of magnetic data. Geophysics. 1996;**61**(2):394-408

[4] Pilkington M. 3-D magnetic imaging using conjugate gradients. Geophysics. 1997;**62**(2): 1132-1142

[5] Portniaguine O, Zhdanov MS. 3-D magnetic inversion with data compression and image focusing. Geophysics. 2002;**67**(5):1532-1541

[6] Portniaguine O, Zhdanov MS. Focusing geophysical inversion images. Geophysics. 1999; **64**(3):874-887

[7] Fedi M. DEXP: A fast method to determine the depth and the structural index of potential fields sources. Geophysics. 2007;**72**(1):I1-I11

[8] Liu S, Hu X, Liu T, et al. Magnetization vector imaging for borehole magnetic data based on magnitude magnetic anomaly. Geophysics. 2013;**78**(6):D429-D444

[9] Lelièvre PG, Oldenburg DW. Magnetic forward modelling and inversion for high susceptibility. Geophysical Journal International. 2006;**166**(1):76-90

[10] Guo W, Dentith MC, Li Z, et al. Self demagnetisation corrections in magnetic modelling: Some examples. Exploration Geophysics. 1998;**29**(3/4):396-401

[11] Guo W, Dentith MC, Bird RT, et al. Systematic error analysis of demagnetization and implications for magnetic interpretation. Geophysics. 2001;**66**(2):562-570

[12] Clark DA. Methods for determining remanent and total magnetisations of magnetic sources–a review. Exploration Geophysics. 2014;**45**(4):271-304

[13] Fedi M, Florio G, Rapolla AA. Method to estimate the total magnetization direction from a distortion analysis of magnetic anomalies. Geophysical Prospecting. 1994;**42**(3): 261-274

[14] Bilim F, Ates A. An enhanced method for estimation of body magnetization direction from pseudogravity and gravity data. Computers & Geosciences. 2004;**30**(2):161-171

[15] Phillips JD. Can we estimate total magnetization directions from aeromagnetic data using Helbig's integrals? Earth, Planets and Space. 2005;**57**(8):681-689

[16] Nicolosi I, Blanco-Montenegro I, Pignatelli A, et al. Estimating the magnetization direction of crustal structures by means of an equivalent source algorithm. Physics of the Earth and Planetary Interiors. 2006;**155**(1):163-169

[17] Dannemiller N, Li Y. A new method for determination of magnetization direction. Geophysics. 2006;**71**(6):L69-L73

[18] Gerovska D, Araúzo-Bravo MJ, Stavrev P. Estimating the magnetization direction of sources from southeast Bulgaria through correlation between reduced-to-the-pole and total magnitude anomalies. Geophysical Prospecting. 2009;**57**(4):491-505

[19] Li J, Zhang Y, Yin G, et al. An approach for estimating the magnetization direction of magnetic anomalies. Journal of Applied Geophysics. 2017;**137**(1–7)

[20] Shearer S, Li Y, 3D inversion of magnetic total gradient data in the presence of remanent magnetization, in 74th SEG Annual Meeting Expanded Abstracts. 2004. p. 774-777

[21] Liu S, Hu X, Xi Y, et al. 2D sequential inversion of total magnitude and total magnetic anomaly data affected by remanent magnetization. Geophysics. 2015;**80**(3):K1-K12

[22] Li S, Li Y. Inversion of magnetic anomaly on rugged observation surface in the presence of strong remanent magnetization. Geophysics. 2014;**79**(2):J11-J19

[23] Li Y, Shearer SE, Haney MM, et al. Comprehensive approaches to 3D inversion of magnetic data affected by remanent magnetization. Geophysics. 2010;**75**(1):L1-L11

[24] Leao-Santos M, Li Y, Moraes R. Application of 3D magnetic amplitude inversion to iron oxide-copper-gold deposits at low magnetic latitudes: A case study from Carajas Mineral Province, Brazil. Geophysics. 2015;**80**(2):B13-B22

[25] Li Y, He ZX, Liu YX. Application of magnetic amplitude inversion in exploration for volcanic units in a basin environment. Geophysics. 2012;**77**(5):B219-B225

[26] Pilkington M, Beiki M. Mitigating remanent magnetization effects in magnetic data using the normalized source strength. Geophysics. 2013;**78**(3):J25-J32

[27] Guo L, Meng X, Zhang G. Three-dimensional correlation imaging for total amplitude magnetic anomaly and normalized source strength in the presence of strong remanent magnetization. Journal of Applied Geophysics. 2014;**111**:121-128

[28] Zhou J, Meng X, Guo L, et al. Three-dimensional cross-gradient joint inversion of gravity and normalized magnetic source strength data in the presence of remanent magnetization. Journal of Applied Geophysics. 2015;**119**:51-60

[29] Ekinci YL, Özyalın Ş, Sındırgı P, et al. Amplitude inversion of 2D analytic signal of magnetic anomalies through differential evolution algorithm. Journal of Geophysics and Engineering. 2017;**14**:1492-1508

[30] Srivastava S, Agarwal B. Inversion of the amplitude of the two-dimensional analytic signal of the magnetic anomaly by the particle swarm optimization technique. Geophysical Journal International. 2010;**182**(2):652-662

[31] Wang M, Di Q, Xu K, et al. Magnetization vector inversion equations and 2D forward and inversed model study. Chinese Journal of Geophysics. 2004;**47**(3):528-534 (in Chinese with English abstract)

[32] Lelièvre PG, Oldenburg DW. A 3D total magnetization inversion applicable when significant, complicated remanence is present. Geophysics. 2009;**74**(3):L21-L30

[33] Ellis RG, de Wet B, Macleod IN, Inversion of magnetic data for remanent and induced sources, in 22nd ASEG International Geophysical Conference and Exhibition Extended Abstracts. 2012. p. 1-4

[34] Liu S, Feng J, Gao W, et al. 2D inversion for borehole magnetic data in the presence of significant remanence and demagnetization. Chinese Journal of Geophysics. 2013;**56**(12): 4297-4309 (in Chinese with English abstract)

[35] Krahenbuhl RA, Li Y, Influence of self-demagnetization effect on data interpretation in strongly magnetic environments, In: SEG 77th Annual Meeting, San Antonio (TX), USA, Expanded Abstracts. 2007. p. 713-716

[36] Vogel A. The application of electronic computers to the calculation of effective magnetisation. Geophysical Prospecting. 1963;**11**(1):51-58

[37] Sharma PV. Demagnetization effect of a rectangular prism. Geophysics. 1968;**33**(1):132-134

[38] Sharma PV. Rapid computation of magnetic anomalies and demagnetization effects caused by bodies of arbitrary shape. Pure and Applied Geophysics. 1966;**64**(1):89-109

[39] Fang H. Calculation of magnetic anomaly by three-dimensional bodies of high susceptibility with arbitrary shapes. Acta Geologica Sinica. 1978;**78**(1):63-78 (in Chinese with English abstract)

[40] Eskola L, Tervo T. Solving the magnetostatic field problem (a case of high susceptibility) by means of the method of subsections. Geoexploration. 1980;**18**(2):79-95

[41] YuI B. Calculation of the magnetic field due to two-dimensional anisotropic objects of arbitrary sections with consideration of demagnetization. Izvestiya, Earth Physics. 1980; **16**(2):126-130

[42] Wang S. The direct problem of magnetic prospecting under anisotropic condition and the solution to solve it. Acta Geophysica Sinica. 1983;**26**(1):58-69 (in Chinese with English abstract)

[43] Wang S. On the theory using the finite element method to solve direct problem of magnetic exploration. Acta Geophysica Sinica. 1981;**24**(2):207-217 (in Chinese with English abstract)

[44] Wu X, Liu X. Magnetization distribution of a 3-dimensional bodies of high susceptibility. Acta Geophysica Sinica. 1982;**25**(5):470-480 (in Chinese with English abstract)

[45] Xu B. The problem of heterogeneous magnetization for homogeneous non-quadratic surface magnetic body. Journal of Changchun University of Earth Science. 1982;**12**(2): 103-114 (in Chinese with English abstract)

[46] YuI B. Incorporation of demagnetization when solving direct magnetic exploration problems for three-dimensional isotropic objects. Izvestiya, earth. Physics. 1983;**19**(5):417-420

[47] Furness P. A versatile integral equation technique for magnetic modelling. Journal of Applied Geophysics. 1999;**41**(4):345-357

[48] Purss MB, Cull JP. A new iterative method for computing the magnetic field at high magnetic susceptibilities. Geophysics. 2005;**70**(5):L53-L62

[49] Kostrov NP. Calculation of magnetic anomalies caused by 2D bodies of arbitrary shape with consideration of demagnetization. Geophysical Prospecting. 2007;**55**(1):91-115

[50] Krahenbuhl RA, Li Y. Investigation of magnetic inversion methods in highly magnetic environments under strong self-demagnetization effect. Geophysics. 2017

[51] Gerovska D, Araúzo-Bravo MJ. Calculation of magnitude magnetic transforms with high centricity and low dependence on the magnetization vector direction. Geophysics. 2006;**71**(5):I21-I30

[52] Stavrev P, Gerovska D. Magnetic field transforms with low sensitivity to the direction of source magnetization and high centricity. Geophysical Prospecting. 2000;**48**(2):317-340

Chapter 4

Basement Tectonics and Fault Reactivation in Alberta Based on Seismic and Potential Field Data

Eneanwan Ekpo, David Eaton and Ronald Weir

Additional information is available at the end of the chapter

http://dx.doi.org/10.5772/intechopen.72766

Abstract

Injection-induced seismicity in Western Canada and elsewhere in North America has drawn considerable recent interest. Current models indicate that induced earthquakes occur on reactivated basement faults, which can be challenging to detect using seismic-reflection data. Here we use regional gravity and magnetic datasets, together with LITHOPROBE crustal seismic profiles, to investigate basement tectonics and crustal structure in an area of Western Canada that is prone to induced seismicity. Previously mapped basement faults that were active during the Paleozoic can be recognized on the basis of pronounced curvature, truncations and/or offsets of stratigraphic marker horizons. Within the Precambrian crystalline basement, however, brittle faults are poorly imaged by seismic data due to various factors such as the obscuring effect of multiples. Regional potential-field fabrics are critical to establish the tectonic setting of basement domains, with complementary information provided by magnetic, Bouguer and isostatic residual gravity anomalies based on 2D modelling constrained by seismic profiles. However, individual faults appear to lack diagnostic expression in regional potential-field anomaly data, since the anomalies are dominated by the effects of larger-scale crustal structures. We show evidence that large-scale basement faults can potentially be recognized on the basis of truncation and offset of distinct horizons within the Winagami Reflection Sequence (WRS), which is interpreted as a regionally-extensive mid-crustal sill complex emplaced during a Proterozoic magmatic pulse. An abundance of caution is necessary to interpret these features, due to complications arising from out-of-plane reflections at long reflection times.

Keywords: magnetics, gravity, seismic, basement reactivation, induced seismicity

1. Introduction

During the last decade, exploitation of unconventional resources, including low-permeability hydrocarbons, has been a major focus of oil and gas development in North America. One

emerging area of concern is induced seismicity, which has led to a renewed interest in faults as well as the structural architecture of Precambrian basement. Recent studies of injection-induced seismicity in parts of Western Canada [1–3] have highlighted the probable role of pre-existing basement faults in controlling the distribution of induced earthquakes. Although some basement-related faults in this region have been identified using seismic-reflection images (for example, see [4–6]), faults that may control the location of induced earthquakes are often challenging to detect using seismic-reflection images alone. Problematic cases include faults with a geometry that is unfavourable for seismic mapping in horizontally stratified rocks, such as sub horizontal thrust faults or vertical strike-slip faults, or brittle faults hosted within crystalline basement rocks that lack clear marker reflections. The latter is particularly true in the shallow crystalline basement in Western Canada, where basement structure may be difficult to discern in the presence of strong multiple reflections [7].

Modelling and interpretation of regional gravity and magnetic data can provide valuable insights for understanding crustal structure beneath sedimentary basins [8, 9] including constraints for understanding geological risk factors for induced seismicity [10]. Models derived from magnetic and gravity data, due to their non-uniqueness, are usually combined with other geological and geophysical information (e.g. seismic and well data), to provide insights into the geometry of the subsurface [9]. The Western Canada Sedimentary Basin (WCSB) is a mature hydrocarbon basin, where extensive public-domain datasets are available, including regional-scale gravity and magnetic anomaly data as well as crustal seismic profiles. To complement the potential field data, this study uses crustal seismic-reflection data from the Alberta Basement Transects (ABT) Peace River Arch Industry Seismic Experiment (PRAISE) project [11], part of Canada's LITHOPROBE program [12].

The objective of this contribution is to present new insights arising from geophysical imaging and mapping of representative basement fault structures, together with a discussion of how they may be significant as a framework for understanding induced seismicity. The LITHOPROBE seismic profiles intersect structural boundaries that are seen on the regional aeromagnetic and gravity mapping. Our interpretation approach involves mapping and identification of basement structures, followed by 2D gravity and magnetic modelling for selected features. Since the gravity and aeromagnetic data span a large geographical area they are useful to characterize large-scale trends, whereas the 2D seismic lines give detailed constraints for building a model, such as fault throw and timing. Potential field data thus give a more complete tectonic picture of the area by filling in the gaps between areas of seismic coverage, providing an opportunity to improve our understanding of the structural framework.

2. Regional geological setting

The Precambrian basement beneath Alberta was formed by amalgamation of disparate domains that were assembled by the plate-tectonic processes of subduction and collision [13–15]. The crystalline basement in Alberta can be subdivided into three broad regions

http://dx.doi.org/10.5772/intechopen.72766

(**Figure 1**). Southern Alberta is dominated by Archean domains, bounded to the north by the Vulcan Low; central Alberta consists of the domains of the Hearne Province that surround the Snowbird Tectonic Zone (STZ); and, northern Alberta consists of the domains that surround the early Proterozoic Great Slave Lake shear zone (GSLsz). Basement domains that are the focus of this study occur between the STZ and GSLsz and have Paleoproterozoic crystallization ages (1.9–2.4 Ga).

Subdivision of the crystalline basement underlying the WCSB into tectonic domains is based on sparse drillcore samples from hydrocarbon exploration wells, coupled with potential-field interpretation [14, 15]. The drillcore samples are described by [15] in terms of location, rock type, mineralogy and crystallization age based on U-Pb geochronology. Our study area is underlain by basement rocks of the Ksituan, Chinchaga, Buffalo Head and Wabumum domains (**Figure 1**), which are composed of igneous, metaigneous and less commonly metasedimentary rocks of Paleoproterozoic age (2.4–1.9 Ga). The 1.90–1.98 Ga Ksituan domain is defined by its strong, positive magnetic expression, which is typical of calc-alkaline magmatic belts due to the presence of magnetite as an accessory mineral phase [15]. Crustal imbrication

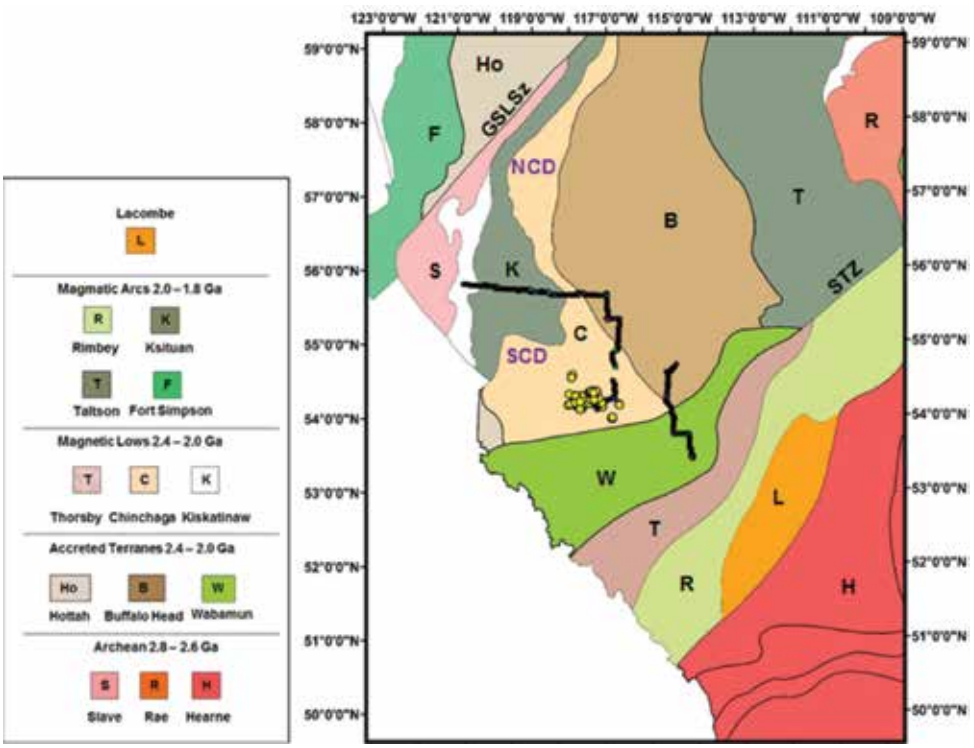

Figure 1. Location map showing tectonic domains of the Precambrian basement from [15]. Black lines show LITHOPROBE seismic profiles from the ABT-PRAISE transect. Yellow dots show seismicity from within the region 54–56°N, 116–118°W, from January 2014 to January 2017 ($M_W \geq 2.5$). Abbreviations and generalized ages of basement domain names are indicated in the legend. In addition, GSLsz denotes Great Slave Lake shear zone, STZ denotes Snowbird Tectonic Zone, SCD and NCD denotes southern and northern Chinchaga domain.

and pervasive ductile deformation of the Ksituan domain is evident from well-developed seismic-reflection fabrics, in the form of panels of dipping reflections in the upper and middle crust [4]. To the east, the slightly older (2.0–2.32 Ga) Buffalo Head Terrane is characterized by sinuous aeromagnetic patterns and discrete subdomains, composed of metaplutonic and subordinate felsic metavolcanic rocks [14]. The eastern edge of the Buffalo Head is defined by the Kimiwan anomaly, a linear magnetic high ~250 km in length. The origin of this magnetic anomaly has been interpreted as either a decapitated calc-alkaline pluton, or a broad zone of hydrothermal alteration and enhanced susceptibility above a crustal-scale extensional fault [9]. The former interpretation is more consistent with oxygen isotope signature of basement samples [16].

To the south, the Chinchaga domain overlaps in age with the Buffalo Head Terrane and is delineated by a negative magnetic anomaly pattern that reflects the absence of calc-alkaline granitic rocks. As discussed below, we distinguish between the northern and southern Chinchaga domains based on potential-field evidence. The southern Chinchaga domain is of particular interest as it underlies the Kaybob-Duvernay region where induced seismicity is concentrated. Finally, the Wabamun domain is interpreted as a structurally bound wedge-shaped block that is enclosed by strands of the Snowbird Tectonic Zone (STZ; [14]), possibly analogous (in terms of structural style) to Archean crustal-scale lozenges formed by annealed mylonites where the STZ is exposed at the surface [17].

Throughout the study area, dipping reflection fabrics observed on LITHOPROBE profiles in the upper and middle crust are cross-cut by the Winagami Reflection Sequence (WRS), a set of prominent, sub-horizontal reflections with an estimated areal extent of ~120,000 km^2 [18]. These reflections are interpreted as sheet-like mafic intrusions that record a ca. 1.8 Ga magmatic event. At several locations, the reflections can be followed around perpendicular bends in survey lines with no change in apparent dip, confirming that the reflectors are approximately horizontal [18]. As illustrated in **Figure 2**, at some locations individual reflections appear to be truncated and offset, suggestive of post-intrusive fault displacement [9].

Sedimentary units in this part of the WCSB are broadly divisible into three major stratigraphic successions that were deposited in three distinct phases [19]. From Cambrian to mid-Devonian time this region was situated near a passive margin, with non-deposition in the emergent Peace River Arch over a large region in the northern part of this study area [4]. During the Devonian, extensive carbonate shelf complexes formed, locally capped by linear reef chains, isolated reefs or reef complexes [20]. It has been suggested that sedimentation patterns, including abrupt facies changes, the development of fracture porosity and the orientation of reef trends or clastic strandlines, may have been influenced by small topographic features on the basement surface [21] that were transferred up section through a process of tectonic inheritance [20]. During the next major phase, the topographic expression of the Peace River Arch reversed to form the Peace River Embayment. Within the embayment, the formation of a network of satellite grabens caused localized subsidence during the Carboniferous, followed by more widespread subsidence during Permian and Triassic time [22]. The final major depositional phase was characterized by enhanced Mesozoic subsidence within a foreland basin in front of advancing Laramide thrust sheets [23].

http://dx.doi.org/10.5772/intechopen.72766

3. Geophysical data

In the 1990s, the Canadian LITHOPROBE program acquired a series of long 2D seismic-reflection transects as part of the Alberta Basement Transects program, with the objective of identifying structures present in the sedimentary basin and deeper levels of the crust [11]. The data were acquired using vibroseis sources and recorded to 18 s two-way time (TWT). In the case of the ABT-PRAISE program, acquisition parameters included a 25-m receiver group interval, 480 channels and unusually long offsets (>6 km) that are conducive to attenuation of multiple reverberations [4]. A representative 2D migrated data example is shown in **Figure 2**, where the approximate depth in the crystalline basement is calculated assuming an average P-wave velocity of 6 km/s.

Terrestrial gravity data used in this study were compiled on a 1 km grid by the Canadian Geodetic Survey and made available through the Geoscience Data Repository for Geophysical Data. Although the grid is sampled at 1 km, the raw data were acquired using an irregular distribution of stations with an average inter-station spacing of >5 km. Despite dense sampling along LITHOPROBE profiles [9], anomaly wavelengths that can be resolved without aliasing (based on the Nyquist criterion) are thus greater than 10 km. A Bouguer gravity anomaly map of Western Canada derived from this dataset contains a conspicuous gravity low (~ −200 mGal) associated with the isostatic root coincident with areas of high elevations in the Rocky Mountains (**Figure 3a**). This anomaly obscures most of the basement domains that are of interest in this study. One exception is the Snowbird Tectonic Zone (STZ), which is almost perpendicular to the deformation front and forms the southern boundary of basement domains in our study area. The isostatic residual gravity anomaly map (see [24]) is plotted in **Figure 3b**. By removing most of the gravitational effects of the isostatic root, the isostatic anomaly map reveals a distinct basement fabric parallel to the STZ that is truncated by orogen-parallel anomalies. A residual positive isostatic anomaly with an amplitude of ~25 mGal

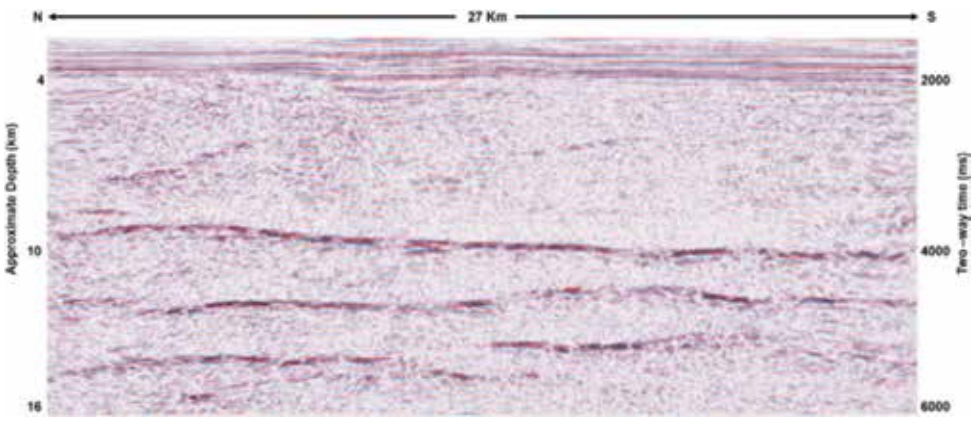

Figure 2. Representative seismic expression of the Winagami Reflection Sequence (WRS) from LITHOPROBE deep seismic profiles. The WRS is comprised of subparallel high-amplitude reflections that form an anastomosing fan that converges toward the southeast [18]. The location of this section is marked in **Figure 4**.

is caused by flexural support of the Rocky Mountain front ranges, which is not accounted for by the isostatic correction [2].

An enlargement of the isostatic gravity map for our study area is shown in **Figure 4a**. The area is characterized by positive anomalies with ovoid shape and peak amplitudes of ~10 mGal,

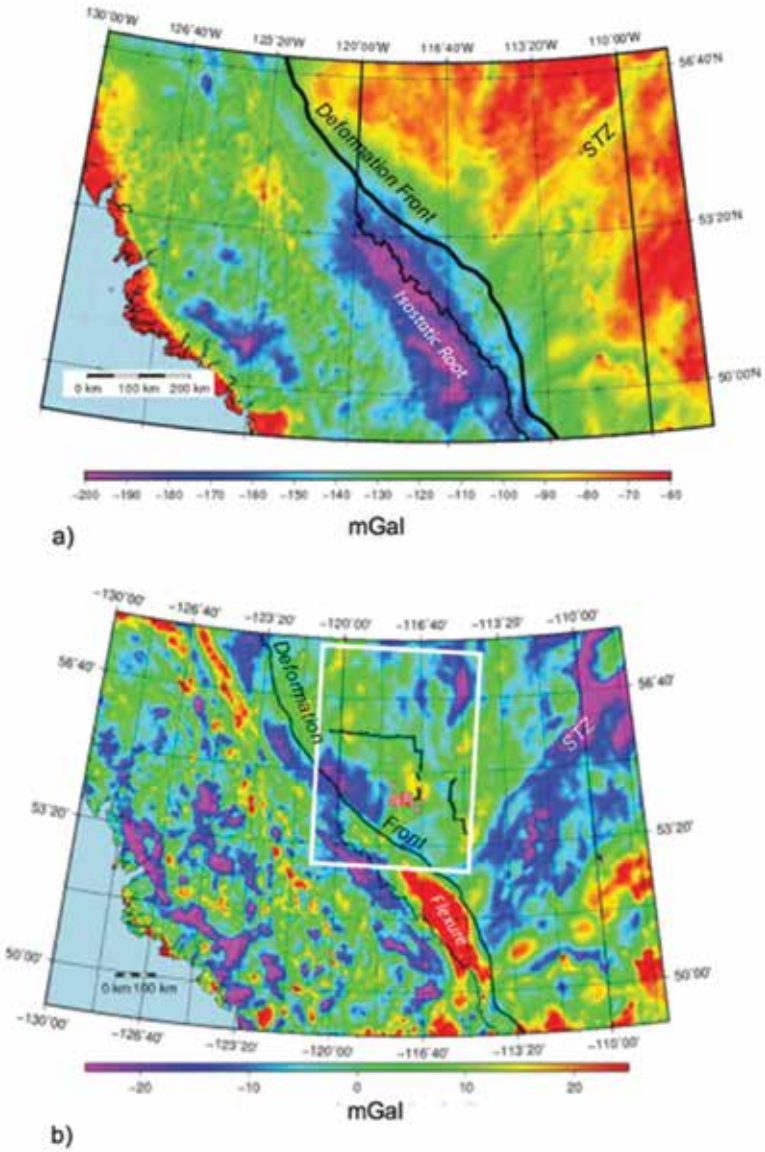

Figure 3. (a) Bouguer gravity anomaly map of Western Canada, showing a −200 mGal anomaly associated with the isostatic root beneath high elevations in the Rocky Mountains as well as a linear anomaly along the Snowbird Tectonic Zone (STZ). (b) Isostatic gravity anomaly map, highlighting a positive residual associated with lithospheric flexural support for high topography [2]. Black lines show ABT-PRAISE transect and white box shows area of **Figure 4**.

which produce overall weak NE–SW fabric wavelengths in the ranges of 25–50 km. The only basement tectonic domain boundary that is clearly expressed in this map is the boundary between the southern Chinchaga domain, characterized by positive isostatic gravity residual, and the Wabamun domain which has a weakly negative character.

The aeromagnetic dataset used in this study is a 200-m residual total-field intensity grid obtained from the national aeromagnetic database (Geoscience Data Repository for Geophysical Data). This grid was compiled from different vintages of survey data, including public-domain and industry surveys flown over several decades [9]. **Figure 4b** shows an aeromagnetic anomaly map of the study area derived from this dataset. In contrast to the gravity anomaly map (**Figure 4b**), basement domain boundaries are prominently expressed in the aeromagnetic map. This is expected, since at a regional scale, the shape and intensity of the magnetic anomalies is primarily controlled by the magnetic susceptibility of the basement domains [15]. Apart from the loss of short-wavelength content toward the southwest due to thickening of the sediment cover, short-wavelength basement topography is muted by the high flexural strength of the lithosphere [21] and thus has a relatively minor influence on the magnetic anomalies.

There are a number of prominent magnetic features in **Figure 4b**. The Ksituan domain (K) is characterized by elongate positive magnetic anomalies with wavelengths ~5–10 km that converge northwards toward the GSLsz, located in the northwest corner of the map. An abrupt rectilinear high-gradient zone separates the Ksituan domain from the southern Chinchaga

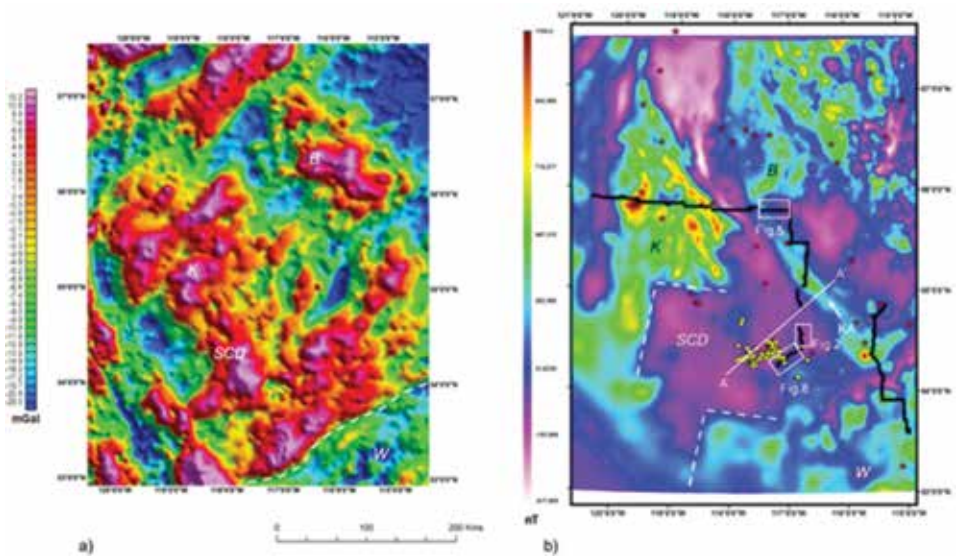

Figure 4. (a) Enlargement of isostatic residual gravity anomaly map within the area outlined in **Figure 3**. K, B, W and SCD denote Ksituan, Buffalo Head, Wabamun and Southern Chinchaga Domain, respectively. Dashed line indicates boundary between SCD and W, which may be a northern splay of the Snowbird Tectonic Zone. (b) Aeromagnetic anomaly map of the same area. Red stars show locations of basement drillcore and yellow circles show seismicity from **Figure 1**. SCD is bounded to the north and south by similar rectilinear edges, as shown by the dashed white lines. Short-wavelength features of magnetic anomalies diminish to the southwest due to increasing basement depth.

domain, which is characterized by muted, longer-wavelength negative magnetic anomalies. A "conjugate" rectilinear boundary, geometrically identical to the northern rectilinear boundary, marks the southern edge of the Chinchaga magnetic low. The Kimiwan anomaly (KA) is a NW-trending positive magnetic anomaly that merges with the arcuate western margin of the Buffalo Head high (B). Unlike other parts of the WCSB [9, 24], there is remarkably little correlation between the anomaly fabrics evident in the gravity and magnetic maps. The Kaybob-Duvernay region, where a high-concentration of induced seismicity exists, is underlain by basement rocks of the southern Chinchaga domain. Although the epicentral distribution in **Figure 4b** reveals a diffuse cloud that is elongate in an east-west direction, the location uncertainty for individual events is ~20 km. In contrast, recent studies that feature high-resolution epicentre locations [2] and well-resolved focal mechanisms [3] indicate that individual fault planes are approximately vertical with a likely north-south strike direction. Thus, local potential-field anomaly fabrics in this region with a roughly north-south trend may be of particular relevance for understanding induced seismicity.

4. Modelling and interpretation

The first example that we consider is the Tangent fault, a Carboniferous normal fault that bounds a half-graben within the Peace River Embayment [4]. This fault has not generated any induced seismicity, but it provides a useful template for interpretation of the geophysical expression of other faults. **Figure 5** shows a LITHOPROBE profile across the Tangent fault, which is characterized by a clearly defined down-to-the-east displacement of the top of the Precambrian basement. After correlating stratigraphic picks using a well tie, it is evident that overlying Paleozoic marker reflections (Wabamun, Banff, Debolt) exhibit a folded (or draped) character across the Tangent fault. This deformation style is consistent with a case study by [6],

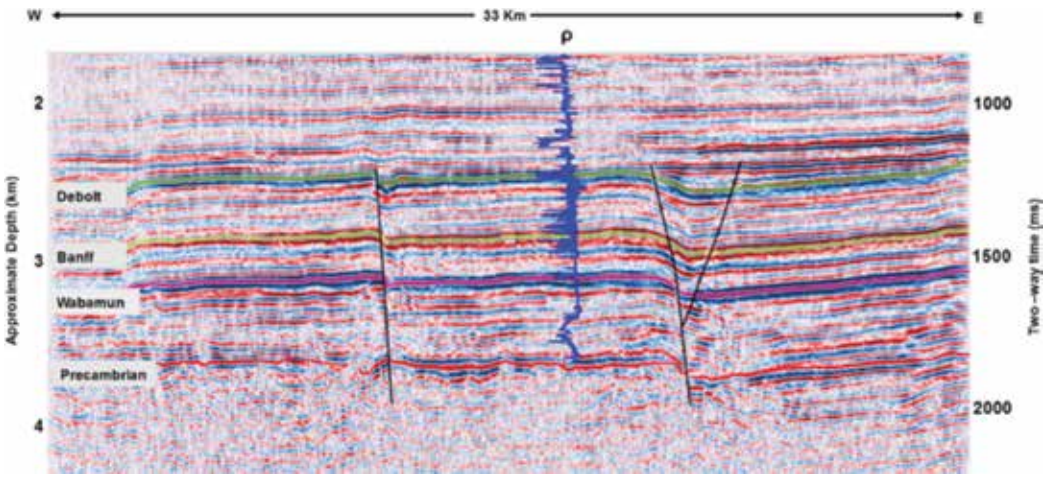

Figure 5. Seismic profile across the Tangent fault as well as a smaller fault to the west, showing the density well log used to obtain a stratigraphic tie. This section was used to build the 2D model in **Figure 6**.

http://dx.doi.org/10.5772/intechopen.72766

who argued that curvature attributes derived from seismic data are well suited to identify subtle faults in the Kaybob-Duvernay region. In addition to the main Tangent fault, an antithetic fault and a smaller fault are visible in the profile.

Figure 6 shows a simple gravity model for the Tangent fault, based on geometrical constraints derived from the seismic profile (**Figure 5**). The 2D gravity modelling method is based on the computed gravitational response of polygonal prisms of uniform density [25]. The model comprises three lithostratigraphic successions: Carboniferous-Mississippian (Debolt and Banff), Devonian (Wabamum) and Precambrian (Top of the crystalline basement). An average density was used from the available density log in the area as a constraint. The density of each layer is indicated on the profile. A good fit between observed and modelled gravity was achieved; however, the faults in this profile have a very small gravitational response. While this may reflect the coarse sampling of the raw gravity data, it demonstrates that the public-domain gravity data are primarily useful for regional interpretations, rather than investigation of small-scale structures such as individual faults. This can be observed with the gravity anomaly profile replicating the topmost layer of the crystalline basement.

The well-documented basement faulting illustrated above provides an interpretative template for basement faults in the Kaybob-Duvernay region. **Figure 7** shows a 1.7–2.4 s time

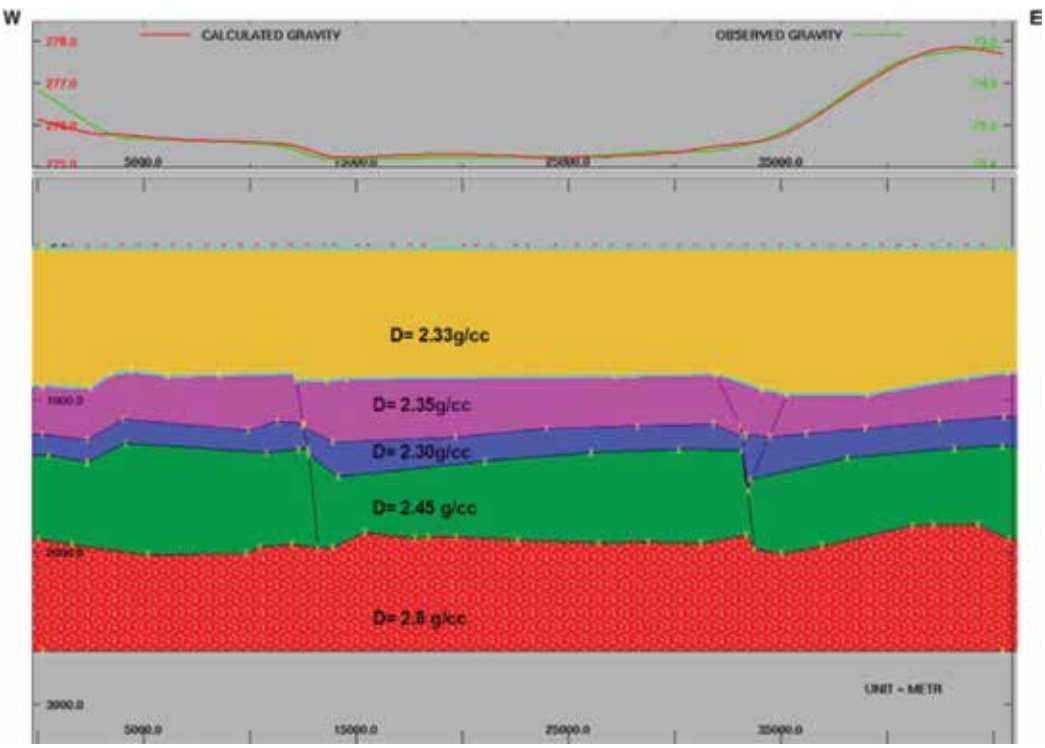

Figure 6. 2D gravity model across the Tangent fault as well as a smaller fault to the east. Layer boundaries are defined based on seismic profile data (**Figure 5**). These faults appear to have a subtle gravity response.

window of data from the ABT-PRAISE transect in this region, which is prone to induced seismicity. The profile is plotted with a vertical exaggeration of ~8:1. There are several interpreted basement faults in this profile, as marked by the black lines. These faults are interpreted based on observed reflection discontinuities. These features share some characteristics with the Tangent fault, including similar, albeit lower amplitude, expression of folding/drape within the sedimentary layers. One of the inferred basement faults is in close proximity to the edge of the Bigstone Leduc reef, while another inferred fault appears to correlate with a positive topographic feature that coincides with a downlap reflection termination (Z-marker) in the Upper Devonian Ireton formation [26]. Due to the effects of contamination by multiple reverberations below the top of basement at ~2100 ms, it is not clear if these interpreted faults merge at depth in the crystalline basement.

Figure 8 shows the same seismic profile as in **Figure 7b**, but for a larger time window of 1.5–6.25 s, plotted with a vertical exaggeration of ~1.4. This profile contains strong but discontinuous WRS reflections, with a gentle southwest apparent dip within an approximate depth extent of 11–16 km (based on an assumed average basement velocity of 6.0 km/s). Individual WRS reflection show apparent truncations as they approach a listric corridor where these mid-crustal reflections are absent. This pattern of disrupted WRS reflections resembles a similar disrupted pattern described by [9] for a crustal seismic profile across the Kimiwan Anomaly. Based on this reflection geometry, a crustal-scale reverse fault is tentatively interpreted that extends to the top of crystalline basement, at a point where faulting is seen in **Figure 7**. The

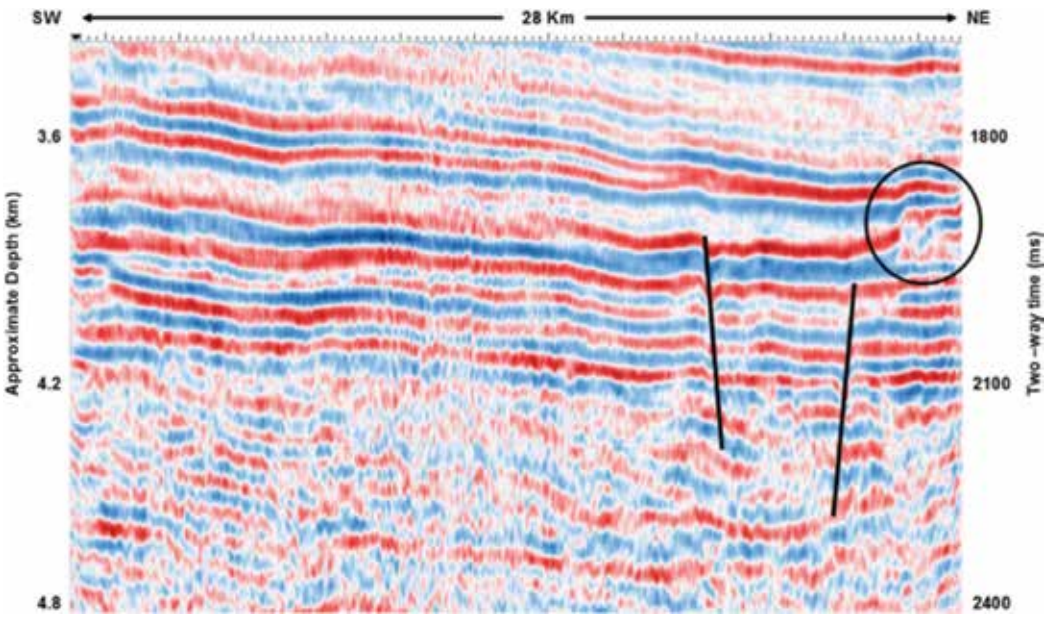

Figure 7. LITHOPROBE seismic profile showing sedimentary layers (vertical exaggeration ~8:1) from the Kaybob-Duvernay region, where induced seismicity has occurred. Several basement faults are evident, as indicated by the black lines. Circle highlights a Leduc reef (Bigstone). Previous workers have suggested that basement faulting may have been influenced the locations of Leduc reefs [7, 20].

http://dx.doi.org/10.5772/intechopen.72766

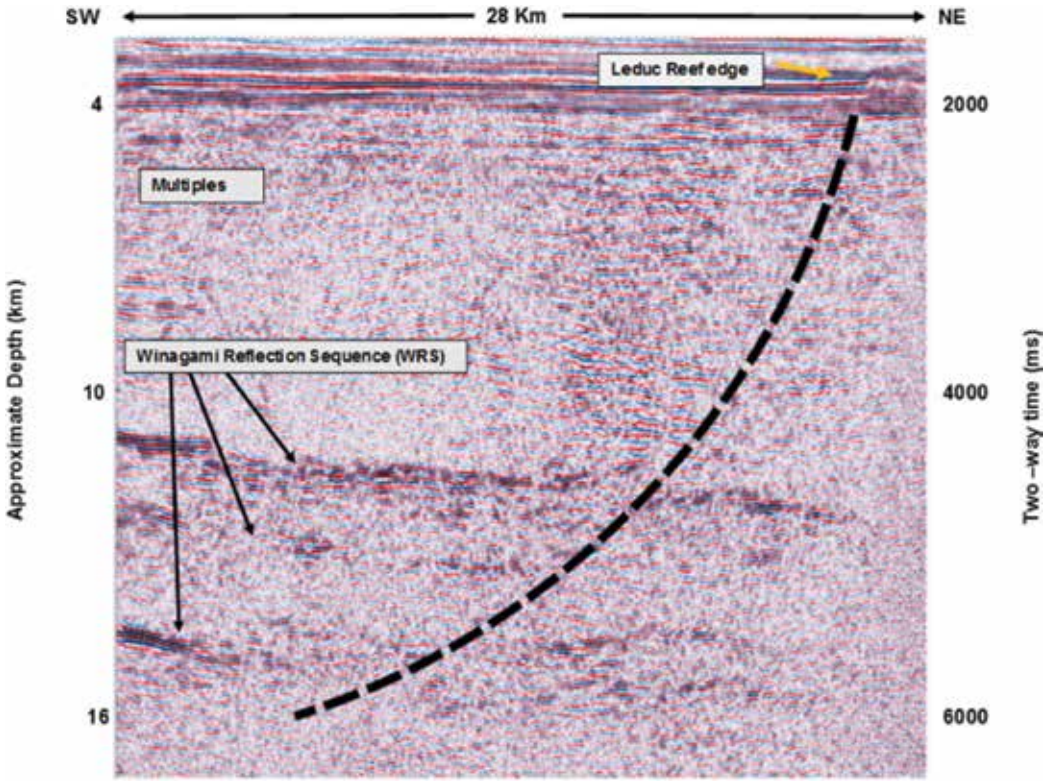

Figure 8. LITHOPROBE seismic data from the same spatial location as in **Figure 6**, showing crustal-scale structure of Winagami Reflection Sequence (WRS). Disruption of the WRS reflections is interpreted here as evidence for post-intrusion basement faulting.

apparent fault offsets of Paleozoic reflections are considerably smaller in amplitude than the apparent offset evident in the middle crust. The interpreted crustal geometry in **Figure 8** was used to develop a gravity and magnetic model (**Figure 9**), with layer parameters in **Table 1**.

Like the gravity modelling, the magnetic modelling was performed using a 2D algorithm based on uniformly magnetized polygonal prisms. Only induced magnetization was considered, based on local parameters for the geomagnetic field. The 2D gravity and magnetic modelling depicted in **Figure 8** shows that a good fit can be achieved between measured and observed potential-field profiles, using polygon vertices derived from the seismic interpretation. Following [9], no regional-residual separation was applied to permit assessment of the influence of features at various crustal levels. The dominant wavelength of the anomalies (>20 km) implies that the depth of features that give rise to the anomalies is considerably deeper than the top of the crystalline basement (~4 km). In this model, the sedimentary package overlaying the crystalline basement (light brown) was treated as one uniform unit with no magnetic susceptibility (k = 0 SI). Hence, the magnetic sources were attributed only to the crystalline basement. The model showed the structure of the basement on a regional scale. Hence, high-frequency anomalies were not modelled. This example also demonstrates

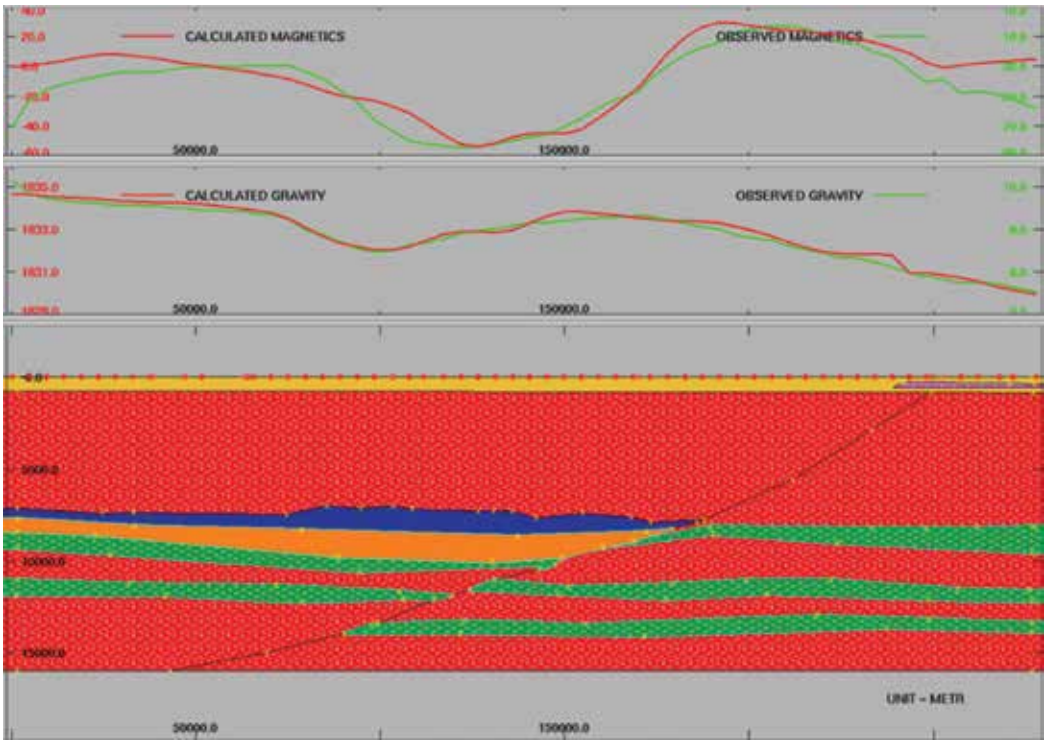

Figure 9. Gravity and magnetic model constructed based on seismic data in **Figures 6** and **7**. Layer densities and magnetic susceptibilities are given in **Table 1**. Total magnetic field parameters used for the 2D magnetic modelling: inclination 68.80°N, declination 2°N and magnitude 49,738 nT.

Modelled layers	Density (g/cc)	Magnetic susceptibility (SI)
Sedimentary package	2.17	0
Leduc reef (pink)	2.08	0.00017
WRS (blue)	2.64	0.02
Basement (brown)	2.82	−0.027
WRS (green)	2.64	0.063
Basement (red)	2.79	0.05

Table 1. Density and magnetic susceptibility values for **Figure 9**.

that the seismic structural interpretation is consistent with the observed gravity and magnetic anomalies.

A final modelling example is presented in **Figure 10**. Here, magnetic and gravity profiles are extracted from the total-intensity aeromagnetic and isostatic gravity anomaly grids, along profile A-A′ (**Figure 4**). This profile cross-cuts the Kimiwan Anomaly as well as a north-south

http://dx.doi.org/10.5772/intechopen.72766

trending positive magnetic anomaly within the southern Chinchaga domain. The Kimiwan Anomaly has a positive magnetic signature (**Figure 4**) about 40 km in width with a northwest orientation. In the isostatic gravity map, this feature is difficult to map. The observed magnetic profile was extracted from the total field intensity magnetic map by getting a profile perpendicular to the two features of interest. Since no seismic constraint is available along this profile, the purpose of this simple forward model is to examine the applicability of the alteration-zone model for the Kimiwan Anomaly [9] to the north-south trending magnetic anomaly from the southern Chinchaga domain. The data was fitted with the anomalous regions situated in the middle crust (**Figure 10**). The observed gravity profile is included for reference. It is not modelled, as the gravity anomaly has a different and non-orthogonal strike direction from the magnetic anomaly so the 2D modelling assumptions would be violated. This example shows that the north-south trending Chinchaga magnetic anomaly, near the region of induced seismicity, can be fit using an anomalous region in the middle crust with susceptibility, depth extent and geometry that is similar to (albeit with a narrower than) the alteration-zone model for the Kimiwan Anomaly [9].

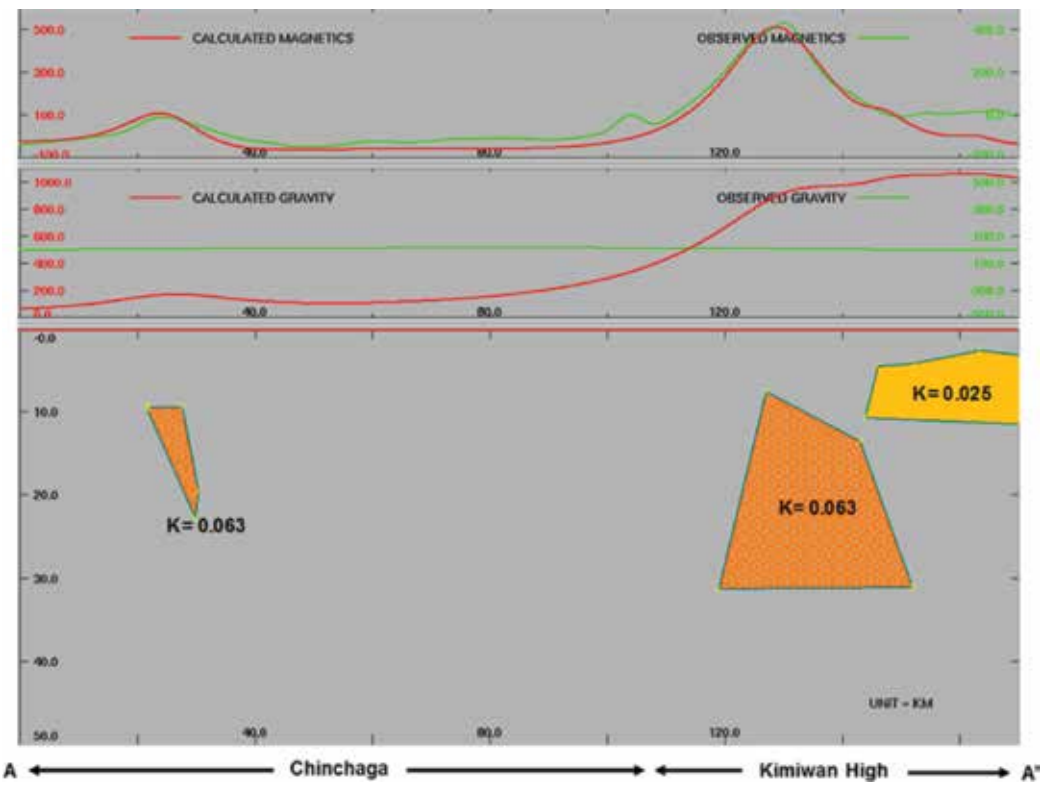

Figure 10. Magnetic model and observed gravity along profile A-A′ (location shown in **Figure 4**). The profile crosses the Kimiwan Anomaly (KA), which forms the boundary between the Southern Chinchaga Domain (SCD) and the Buffalo Head Terrain. A smaller magnetic anomaly at x ~ 30 km is located within the SCD with a trend that is parallel with the KA as well as fault-plane solutions in the Duvernay region. Total magnetic field parameters used: inclination 74.80°N, declination 16°N and magnitude 56,930 nT. Magnetic susceptibility values (K) are in SI units.

5. Discussion and conclusions

In this study, potential-field methods are combined with seismic and well data to investigate basement structure in Alberta. Our analysis shows that regional gravity anomaly patterns primarily reflect large-scale crustal features, such as a Bouguer gravity low that marks the isostatic root beneath the Rocky Mountains (**Figure 3a**), an isostatic gravity high that reflects a flexurally supported topographic load in the Rock Mountain front ranges of Alberta (**Figure 3b**), and NE-SW linear fabrics associated with the Snowbird Tectonic Zone (STZ). On the other hand, magnetic-anomaly maps provide the primary method for delineating the extent of basement tectonic domains [14]. Isostatic-residual gravity anomalies (**Figure 4a**) are characterized by longer wavelength than magnetic anomalies (**Figure 4b**). While the magnetic anomalies predominantly reflect the magnetic susceptibility of the uppermost basement [15], due to the wavelength difference the gravity anomalies are primarily sensitive to deeper crustal levels. This difference in depth sensitivity may explain why the observed isostatic gravity and magnetic intensity fabrics are poorly correlated (**Figure 4**). Moreover, based on the available regional datasets the (likely subtle) magnetic and gravity expression of basement faults appears to be overwhelmed by anomalies produced by large-scale crustal features. This suggests that a good strategy to improve the sensitivity of potential-field methods to detect and constrain basement faults is to acquire densely sampled data and apply a well-characterized regional-residual separation.

There is evidence to suggest that the southern Chinchaga domain is a distinct block from the northern Chinchaga domain, although basement drillcore samples are too sparse to either validate or falsify this interpretation. The Chinchaga domain has primarily negative magnetic anomaly values throughout its north-south extent, but there are distinct characteristics of the magnetic anomalies in the southern part that are dissimilar from magnetic-anomaly characteristics in the north. Specifically, the southern Chinchaga domain has a more muted negative character, with distinct internal positive anomalies that are absent in the north. In contrast, the northern Chinchaga domain is characterized by high-amplitude negative anomalies. In addition, the southern Chinchaga domain has strikingly rectilinear boundaries, in contrast to the arcuate nature of internal and bounding fabrics in the north. There are north-south trending magnetic anomalies in the southern Chinchaga domain that have an orientation consistent with observed induced-seismicity focal mechanisms, so this distinction may be important in terms of fully understanding the relationships of magnetic anomalies to induced seismicity.

As indicated by a LITHOPROBE seismic profile across the Tangent fault in the Peace River Embayment, despite a sharp offset at the top of crystalline basement, the seismic expression of faulting of Paleozoic layers is dominated by folding. This draped seismic expression supports the use of seismic curvature attribute analysis [6] for mapping potential fault structures. In the shallow basement, faults in the WCSB are difficult to map due to the lack of coherent reflections and the obscuring effects of multiple reverberations. On the other hand, disruption and offset of reflections within the Winagami Reflection Sequence (WRS) provides a potential opportunity to pinpoint loci of crustal-scale faulting at depth as an aid in the interpretation of basement faults. This interpretation approach relies on an assumption that these bright

reflections represent mafic sills that were originally more laterally continuous than at present, such that observed offsets can be reasonably interpreted as post-intrusion fault deformation. Extrapolation to the top of basement of the tentatively interpreted crustal-scale reverse fault (**Figures 6** and **7**) would bring this fault to the base of the WCSB close to several interpreted faults in close proximity to a major Leduc reef edge.

Acknowledgements

We are grateful for support from the Natural Sciences and Engineering Research Council of Canada (NSERC) and Chevron for the Industrial Research Chair (IRC) in Microseismic System Dynamics. Warner Miles is thanked for helping with access to gridded aeromagnetic data, and Brian Roberts is thanked for providing LITHOPROBE data. CGG is gratefully acknowledged for licensing of the Geoview suite and LCT software through CGG's worldwide university program. Patrick Quist CGG Houston is thanked for help with answering questions relating to the LCT software and troubleshooting of the seismic and magnetic data. Geosoft software was also used for visualization and interpretation of potential field data. Lydia Dicaprio and Andrew Poulin are thanked for help with GMT and ArcGIS softwares.

Author details

Eneanwan Ekpo[1]*, David Eaton[1] and Ronald Weir[2]

*Address all correspondence to: eneanwan.ekpo@ucalgary.ca

1 MIC, University of Calgary, Calgary, Canada

2 CREWES, University of Calgary, Calgary, Canada

References

[1] Schultz R, Corlett H, Haug K, Kocon K, MacCormack K, Stern V, Shipman T. Linking fossil reefs with earthquakes: Geologic insight to where induced seismicity occurs in Alberta. Geophysical Research Letters. 2016 Mar 28;**43**(6):2534-2542

[2] Bao X, Eaton DW. Large variations in lithospheric thickness of western Laurentia: Tectonic inheritance or collisional reworking? Precambrian Research. 2015 Sep 30;**266**:579-586

[3] Schultz R, Wang R, Gu YJ, Haug K, Atkinson G. A seismological overview of the induced earthquakes in the Duvernay play near Fox Creek, Alberta. Journal of Geophysical Research: Solid Earth. 2017 Jan 1;**122**(1):492-505

[4] Eaton DW, Ross GM, Hope J. The rise and fall of a cratonic arch: A regional seismic perspective on the Peace River Arch, Alberta. Bulletin of Canadian Petroleum Geology. 1999;**47**(4):346-361

[5] Green DG, Mountjoy EW. Fault and conduit controlled burial dolomitization of the Devonian west-central Alberta Deep Basin. Bulletin of Canadian Petroleum Geology. 2005;**53**(2):101-129

[6] Chopra S, Sharma RK, Ray AK, Nemati H, Morin R, Schulte B, D'Amico D. Seismic reservoir characterization of Duvernay shale with quantitative interpretation and induced seismicity considerations—A case study. Interpretation. 2017 Feb 27

[7] Eaton DW, Milkereit B, Ross GM, Kanasewich ER, Geis W, Edwards DJ, Kelsch L, Varsek J. Lithoprobe basin-scale seismic profiling in central Alberta: Influence of basement on the sedimentary cover. Bulletin of Canadian Petroleum Geology. 1995;**43**(1):65-77

[8] Pilkington M, Miles WF, Ross GM, Roest WR. Potential-field signatures of buried Precambrian basement in the Western Canada Sedimentary Basin. Canadian Journal of Earth Sciences. 2000 Nov 1;**37**(11):1453-1471

[9] Hope J, Eaton D. Crustal structure beneath the Western Canada Sedimentary Basin: Constraints from gravity and magnetic modelling. Canadian Journal of Earth Sciences. 2002 Mar 1;**39**(3):291-312

[10] Shah AK, Keller GR. Geologic influence on induced seismicity: Constraints from potential field data in Oklahoma. Geophysical Research Letters. 2017 Jan 16;**44**(1):152-161

[11] Hope J, Eaton DW, Ross GM. Lithoprobe seismic transect of the Alberta Basin: Compilation and overview. Bulletin of Canadian Petroleum Geology. 1999;**47**(4):331-345

[12] Clowes R, Cook F, Hajnal Z, Hall J, Lewry J, Lucas S, Wardle R. Canada's LITHOPROBE Project (collaborative, multidisciplinary geoscience research leads to new understanding of continental evolution). Episodes. 1999 Mar 1;**22**:3-20

[13] Hoffman PF. United plates of America, the birth of a craton: Early Proterozoic assembly and growth of Laurentia. Annual Review of Earth and Planetary Sciences. 1988 May;**16**(1):543-603

[14] Ross GM, Parrish RR, Villeneuve ME, Bowring SA. Geophysics and geochronology of the crystalline basement of the Alberta Basin, Western Canada. Canadian Journal of Earth Sciences. 1991 Apr 1;**28**(4):512-522

[15] Villeneuve ME, Ross GM, Parrish RR, Theriault RJ, Miles W, Broome J. Geophysical subdivision, U–Pb geochronology and Sm–Nd isotope geochemistry of the crystalline basement of the Western Canada Sedimentary Basin, Alberta and northeastern British Columbia. Geological Survey of Canada Bulletin. 1993;**447**:86

[16] Burwash RA, Chacko T, Muehlenbachs K, Bouzidi Y. Oxygen isotope systematics of the Precambrian basement of Alberta: Implications for Paleoproterozoic and Phanerozoic tectonics in northwestern Alberta. Canadian Journal of Earth Sciences. 2000 Nov 1;**37**(11):1611-1628

[17] Hanmer S, Parrish R, Williams M, Kopf C. Striding-Athabasca mylonite zone: Complex Archean deep-crustal deformation in the East Athabasca mylonite triangle, northern Saskatchewan. Canadian Journal of Earth Sciences. 1994 Aug 1;**31**(8):1287-1300

[18] Ross GM, Eaton DW. Winagami reflection sequence: Seismic evidence for postcollisional magmatism in the Proterozoic of Western Canada. Geology. 1997 Mar 1;**25**(3):199-202

[19] Cant DJ. Regional structure and development of the Peace River Arch, Alberta: A Paleozoic failed-rift system? Bulletin of Canadian Petroleum Geology. 1988;**36**(3):284-295

[20] Edwards DJ, Brown RJ. Understanding the influence of Precambrian crystalline basement on Upper Devonian carbonates in central Alberta from a geophysical perspective. Bulletin of Canadian Petroleum Geology. 1999;**47**(4):412-438

[21] Ross GM, Eaton DW. Basement reactivation in the Alberta Basin: Observational constraints and mechanical rationale. Bulletin of Canadian Petroleum Geology. 1999;**47**(4):391-411

[22] Barclay JE, Krause FF, Campbell RI, Utting J. Dynamic casting and growth faulting: Dawson Creek graben complex, Carboniferous-Permian Peace River embayment, Western Canada. Bulletin of Canadian Petroleum Geology. 1990;**38**(1):115-145

[23] O'connell SC. Geological history of the Peace River arch. Geological Atlas of the Western Canada Sedimentary Basin, GD Mossop and I. Shetsen (comp.). Canadian Society of Petroleum Geologists and Alberta Research Council Special Report. 1994;**4**:431-438

[24] Goodacre AK, Grieve RA, Halpenny JF, Warren LA. Isostatic Gravity Anomaly Map of Canada. Ottawa, Ontario, Canada: Surveys and Mapping Branch; 1987

[25] Talwani M, Ewing M. Rapid computation of gravitational attraction of three-dimensional bodies of arbitrary shape. Geophysics. 1960 Feb;**25**(1):203-225

[26] Eaton DW, Ross GM, Clowes RM. Seismic-reflection and potential-field studies of the Vulcan structure, Western Canada: A Paleoproterozoic Pyrenees? Journal of Geophysical Research: Solid Earth. 1999;**104**(B10):23255-23269

Section 2

Geo-Hazard: Seismicity and Geoelectric

Chapter 5

Characterization of Hydrocarbon-Contaminated Sites Based on Geoelectrical Methods of Geophysical Exploration

Omar Delgado-Rodríguez, Vladimir Shevnin,
Héctor Peinado-Guevara and
María Ladrón de Guevara-Torres

Additional information is available at the end of the chapter

http://dx.doi.org/10.5772/intechopen.73103

Abstract

Electrical methods are effective tools for the characterization of oil-contaminated sites and are applied in defining the geometry of the contaminated plume and in designing the remedial process. The optimal methodology integrates geoelectric methods, data processing, and interpretation techniques. Electromagnetic profiling is a reliable and fast method used to provide the configuration of oil-contaminated plume from apparent resistivity map and used to guide the subsequent electrical resistivity tomography survey. From advanced field work methods, data processing, and interpretation procedures, electrical resistivity tomography survey provides the three-dimensional (3D) configuration of the contaminated plume, migration pathways, location of active contaminated sources, and information about lithology. For separate contaminated and clean zones, a petrophysical modeling is used for the calculation of soil resistivity based on groundwater salinity. Taking the pore-water salinity value into account, an inversion algorithm recalculates resistivity maps into maps of clay content, porosity, and cation exchange capacity, allowing a more accurate determination of the volume of contaminated soil. From clay content data, hydraulic conductivity values are calculated for determining the groundwater vulnerability due to vertical migration of contaminants from upper layers. The optimal geoelectric methodology is an efficient procedure to assess hydrocarbon-contaminated sites, with emphasis on large sites with deeper groundwater table.

Keywords: oil-contaminated soil, geoelectrical characterization, petrophysical modeling, contaminated plume, OGEOMET

1. Introduction

In many countries, the growth of oil industry has been accompanied by the contamination of environment owing to exploitation, transportation, refining, and distribution of hydrocarbons. Over the years, great interest has been focused on the study of the environmental impact from oil industry. The spill of oil products can be a devastating event, with obvious consequences. Oil spills have a wide range of negative effects on the environment and economy. The spillage damages waterways, animal life, and plants. Determining the presence and concentration of hydrocarbon contaminants in the subsurface is performed by drilling and chemical analysis of soil samples collected from wells. The steps involved before the results of chemical analyses are obtained are very boring, expensive, and time-consuming. Moreover, in most geological situations, the oil contaminants are concentrated above the water table, implying that it is necessary to drill up to the aquifer, thereby increasing its vulnerability by the infiltration of contaminants from the surface. In most cases, geological conditions such as the presence of hard formations and deeper groundwater table make the drilling works more complicated, expensive, and time-consuming. The location of drilling points without prior knowledge of the spatial distribution of contaminants in subsoil ("blind" selection of drilling points) decreases the efficiency of this procedure.

The resistivity contrast between clean and contaminated rocks depends on the age of the spill. In the case of recent spills, the presence of high-resistivity anomalies is expected. A low-resistivity anomaly arises in contaminated zones between 4 and 6 months after the spill has occurred, depending on the lithological and weather condition of the study area. Sauck [1] proposed that the low-resistivity anomaly is created by the intense action of bacteria on hydrocarbons in the lower part of the vadose zone. The organic and inorganic acids yielded during biodegradation process increase the dissolution of minerals, releasing ions that increase the total dissolved solids (TDSs) in the pore water. Abdel-Aal et al. [2] found some important details of this biodegradation process and changes in the electrical properties of contaminated zones. They demonstrated that the increase of soil conductivity contaminated by hydrocarbons due to the biodegradation process is mainly related to high-surface conductivity of biofilms between solid and liquid components created by bacteria in the pores of the affected rocks. Thus, the application of geoelectric methods is very useful for characterizing both recent and matured oil-contaminated zones [1–3].

Several investigations have demonstrated the successful application of the surface resistivity methods for configuration (in plan and depth) of the hydrocarbon-contaminated zones. Electrical resistivity tomography (ERT) and electromagnetic profiling (EMP) methods are useful for the delimitation of the resistivity anomalies caused by different types of hydrocarbon contaminants and rocks in rural [4, 5], industrial [6], and urban [7] sites. Soil resistivity depends mainly on water content and its salinity, clay content, and porosity. There are many models describing the dependence of soil resistivity on these factors (e.g., [8, 9]). The methodology shown in this chapter includes the use of the petrophysical model explained in detail by Shevnin et al. [10]. In the laboratory, the behavior of soil resistivity versus water salinity in clean soil samples is measured, and clay content, porosity, and cation exchange capacity (CEC) are determined. The knowledge of these petrophysical parameters is used to define the geoelectric

boundary between contaminated and clean zones. It is also possible to obtain cross sections and maps of clay content, porosity, and CEC, using interpreted resistivity data from ERT survey and groundwater salinity information [11]. For uncontaminated soil, these parameters (clay content, porosity, and cation exchange capacity) are close to true petrophysical parameters, estimated with traditional methods in the laboratory. In contaminated soils, petrophysical parameters reach anomalous values. This helps in defining the contaminated plume.

This chapter presents an optimal geoelectric methodology for the characterization of hydrocarbon-contaminated sites that include the application of EMP and ERT methods with advanced petrophysical inversion of the geoelectrical data in order to define the geoelectric boundary between clean and contaminated soil and to estimate soil petrophysical parameters.

2. Optimal geoelectric methodology (OGEOMET)

The optimal geoelectric methodology (OGEOMET) integrates the field and laboratory methods for measuring the soil and water resistivity in situ and on samples, respectively. OGEOMET also includes advanced petrophysical interpretation of the geoelectric data in order to define the geoelectric boundary between clean and contaminated soil and to estimate some soil petrophysical parameters. The field operations include EMP and ERT methods to obtain the spatial distribution of the soil resistivity and the groundwater resistivity measurements (WRMs). In addition, we perform the resistivity measurements in soil samples (RMSSs) to determine clay content, porosity, CEC, and hydraulic conductivity required for the characterization of the contaminated site. **Figure 1** shows the flowchart of field operations, processing, and representation of results obtained from the OGEOMET.

2.1. Application of the electromagnetic profiling (EMP) method

EMP is a reliable and fast method to provide the configuration of the surface contaminated by oil plume from apparent resistivity map. The application of the EMP method involves measuring the response of the subsurface in an induced electromagnetic field. Using the EM31-MK2 equipment [12] (**Figure 2**), an electromagnetic field is generated by a transmitter antenna, inducing eddy currents within the ground. These induced currents generate a secondary magnetic field. Both primary and secondary magnetic fields are measured in a receiver antenna. The ground conductivity (mS/m) is calculated from the ratio of the secondary and primary magnetic fields, and it is affected by a number of factors including clay content, moisture and salinity of pore water, conductive (metal) objects, and conductive contaminants. The EMP results, although not providing detailed stratigraphic information (layers and their thicknesses), can offer the horizontal changes in soil apparent conductivity.

In **Figure 3**, an example of EMP application on one rural site is presented [4]. The depth of the local aquifer is 4 m. The resistivity map has been constructed from the EMP data obtained using EM31-MK2 equipment [12] for the vertical polarization of the magnetic field, ensuring a maximal depth of investigation of 6 m. Twenty-two EMP profiles were performed on the

study site. Each measured conductivity value (mS/m) was converted to a resistivity (Ohm-m) value. The low-resistivity anomalies (blue zones, **Figure 3**) indicate the presence of hydrocarbon contaminants affected by biodegradation process ("mature" contamination). This result is useful to plan the ERT survey (see flowchart in **Figure 1**).

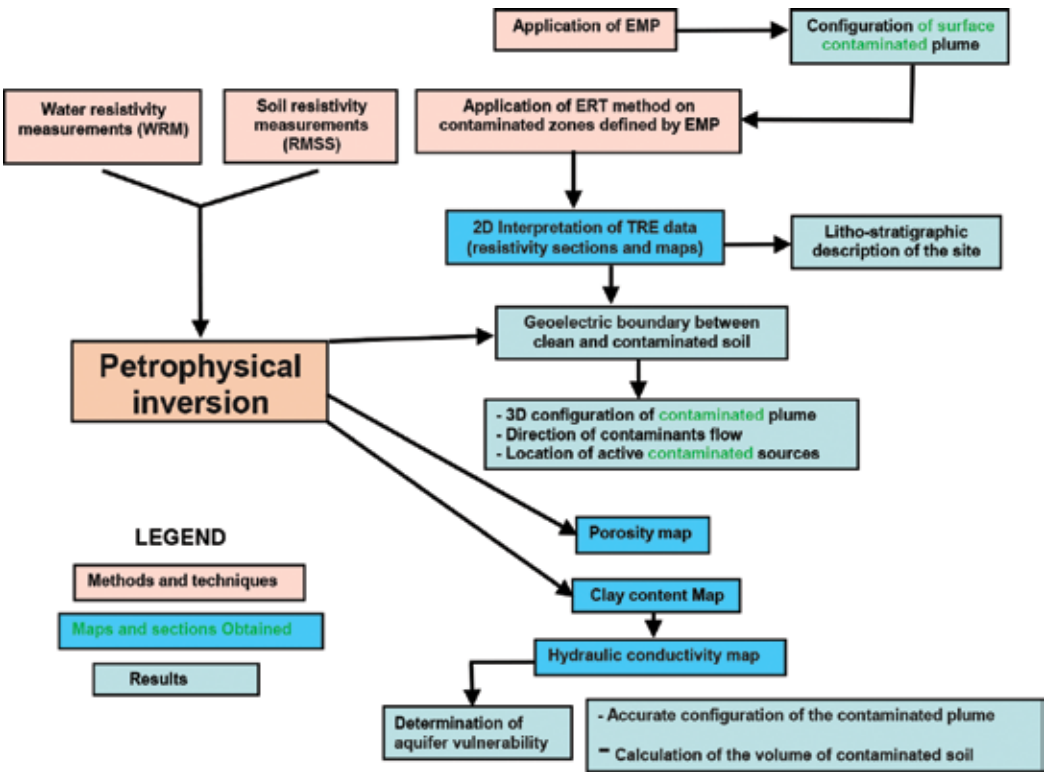

Figure 1. Flowchart of the OGEOMET for the characterization of hydrocarbon-contaminated sites.

Figure 2. EM31-MK2 ground conductivity meter in field operations [12].

http://dx.doi.org/10.5772/intechopen.73103

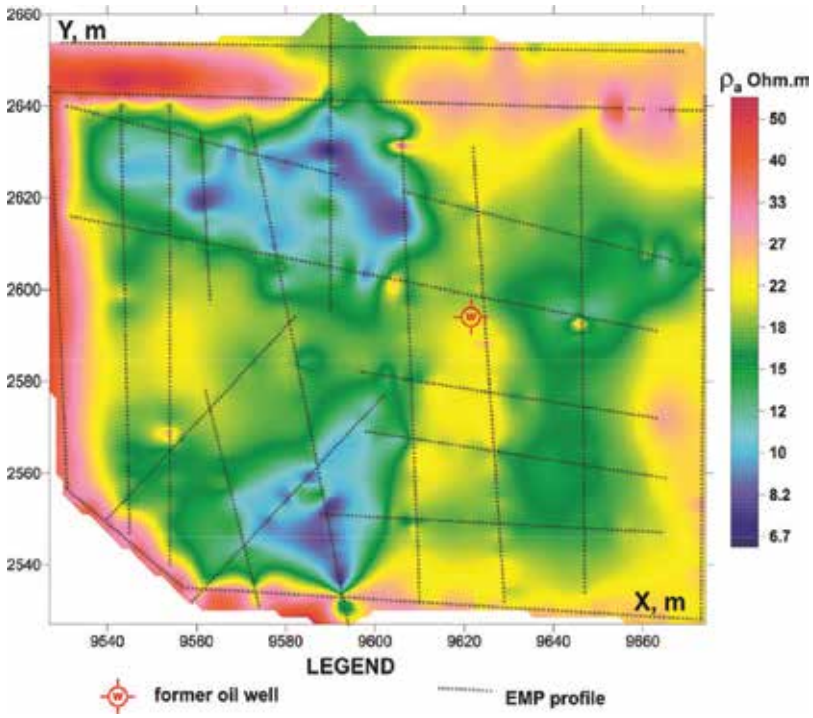

Figure 3. Resistivity map obtained by EMP in a rural site.

2.2. Water resistivity measurements (WRMs)

The procedure for WRM is simple and includes the collection of water samples (~250 ml) in previously selected sampling points (e.g., wells, lagoons, swamps, etc.) using a plastic or a glass container (do not use metal container). A portable tester (e.g., HI98130) is placed in a container, and water conductivity (mS/cm) and temperature (°C) are measured. The water temperature variations are corrected using a reference temperature of 20°C. In some sites, the number of sampling points and their spatial distribution allow the production of water resistivity map. This map gives the preliminary delimitation of main contaminated zones. For example, **Figure 4** shows the water resistivity map obtained in the same rural site where the EMP method was applied (**Figure 3**). Forty-four water samples were collected from wells and pit. The water resistivity map shows low-resistivity anomalies (blue zones in **Figure 4**) as potentially contaminated zones, corresponding to the main low-resistivity anomalies determined by the EMP method (see **Figure 3**). The decrease of the water resistivity in the contaminated zones demonstrates that the biodegradation process of hydrocarbon contaminants increases the values of TDS in pore water of the affected soil.

Frequently, a water resistivity map is not obtained due to lack of water-sampling points. In this case, clean groundwater must be collected, in at least one sampling point, for the calculation of water resistivity and salinity values, useful for the petrophysical inversion procedure and the determination of geoelectric boundary between clean and contaminated soils.

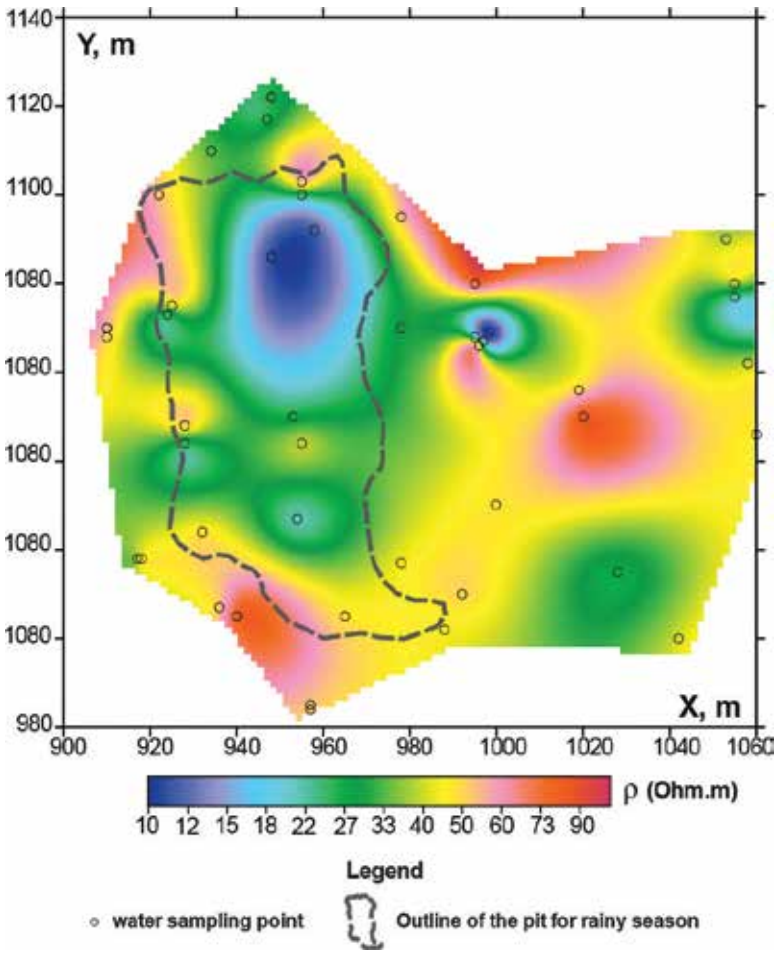

Figure 4. Water resistivity map obtained by the application of WRM in a rural hydrocarbon-contaminated site.

2.3. Resistivity measurements of soil samples (RMSSs)

The soil samples should represent different soil types of the site. For this purpose, a drilling point, outside the contaminated area, is selected, and some soil samples are collected at different depths. A laboratory procedure that gives the characteristics of soil resistivity versus pore water salinity is applied. Each soil sample is dried and homogenized and, then, divided into five similar parts (subsamples) and placed into five soil boxes. Each soil box consists of a rectangular plastic (insulated) container with four electrodes (two to inject current and two to measure voltage). Once the subsample is placed into soil box, the water of known salinity (different for each soil box) in the range between 0.1 and 70 g/l is added to completely saturate each subsample. Taking into account that the electrokinetic process requires significant time (especially for clayed sediments) to achieve an equilibrium, we perform the resistivity measurements 1 h after water deposition. The measurements are performed in the low-frequency range to avoid problem with the electrode polarization and induction effect. The resistivity

values are corrected to reference temperature (e.g., 20°C). Thus, we have five soil electrical resistivity values (one for each soil box) depending on the salinity of the pore water ($\rho_{exp}(C)$) [11]. The soil resistivity obtained as a function of the pore water salinity is used for the petrophysical inversion.

2.4. Petrophysical inversion

From WRM and RMSS, and resistivity data obtained by ERT, it is possible to determine parameters such as clay content, porosity, and cation exchange capacity (CEC), which are important in determining the geoelectric boundary between clean and contaminated soil, and the hydraulic conductivity (K), useful for the assessment of the aquifer vulnerability.

The experimental resistivity versus salinity curve ($\rho_{exp}(C)$) and electrical resistivity values calculated ($\rho_{th}(C)$) using the theoretical model developed by [10, 11] were subjected to a curve-fitting process to calculate the different geological parameters. The theoretical model considers the geometrical microstructure of the components as well as electrochemical processes occurring in the soil for a wide range of the pore-water salinity and clay content. Different parameters are used for petrophysical modeling, including the following: water salinity (including types of anions and cations with their valence, hydration number, sorption constant, and mobility), porosity, capillary radii, humidity, cementation exponent *m*, the CEC for each component of soil, including sand and clay, and the temperature of the soil. The result of the modeling is the calculated soil resistivity as a function of water salinity. We need to estimate three soil parameters: clay content, porosity, and CEC. Once local groundwater (or salinity) and soil resistivity are known, the clay content and porosity are estimated for clean soils of the study site, and the geoelectric boundary is defined. *K* was calculated based on the clay content using the empirical formula proposed by Shevnin et al. [13]

$$K = 7.2.10^{-}4^{*} C^{-2} \quad (1)$$

where K is the saturated soil hydraulic conductivity ($m^{*}day^{-1}$), and C is the clay content in relative units between 0.01 and 1.

A practical example from **Figure 5** shows the results of the petrophysical modeling for the same rural site depicted in **Figures 2** and **4**, where a soil sample was collected from a clean zone. According to priori information, the collected soil belongs to the layer with a higher clay content. Applying the procedure explained earlier, the modeled sample (dashed curve C) gives the clay content of 43%. A value of resistivity of 27 Ohm-m (salinity of 0.22 g/l) was determined for noncontaminated groundwater. Lithologies from pure sand (curve 0) to sand clay with 40% of clay (curve 40, **Figure 5**) are in the range of 14–120 Ohm-m (vertical line A). The clay content for this resistivity interval is between 4 and 40%. Taking into account that the maximum clay content for the site is 43%, then the resistivity values less than 14 Ohm-m correspond to the contaminated soil (gray rectangle B), the resistivity value of the geoelectric boundary being used on the delineation of contaminated zones in resistivity sections and maps.

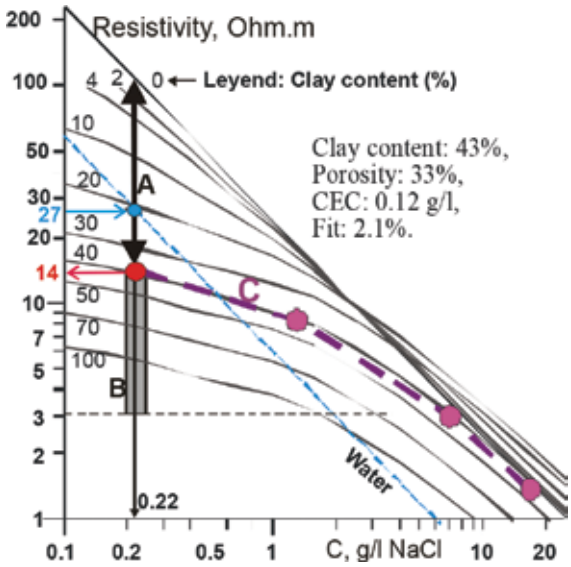

Figure 5. Petrophysical modeling of the rural contaminated site using soil, groundwater, and ERT information.

2.5. Application of the electrical resistivity tomography (ERT) method

ERT uses short spacing for measurements along profiles for two-dimensional (2D) study of inhomogeneous media, and a great number of electrodes are reconnected manually or automatically. The ERT survey has specially selected measuring and current points to obtain high resolution and low distortion caused by near-surface inhomogeneity [14]. In this method, different electrode arrays can be used (pole-dipole, dipole-dipole, and Wenner, Schlumberger).

The 2D inversion of filtered apparent resistivity data provides the high-quality cross sections of the true resistivity distribution. The application of the ERT method allows us to find the depth of contaminated zones and, finally, the 3D configuration of hydrocarbon-contaminated plume. Based on the resistivity cross sections and adding geological information, it is possible to make up lithostratigraphic sections. **Figure 6** shows the interpreted resistivity section of ERT profile 6 (see **Figure 7**) conducted at the same rural site (**Figures 2** and **4**), whose petrophysical modeling (**Figure 5**) defined a geoelectric boundary between clean and contaminated soils of 14 Ohm-m (red contour, **Figure 6**). The contaminated zones are defined in depth accurately allowing a direct soil sampling, reducing the number of soil samples needed for their quantification, and increasing the accuracy of results. For inversion of the apparent resistivity, the software RES2DINV [14] was used.

From 11 interpreted resistivity sections, it was possible to obtain a resistivity map for "target layer." The target layer, where hydrocarbon contaminants are accumulated, is located in the lower part of the vadose zone. **Figure 7** shows the resistivity map for the target layer with a depth interval of 2–4 m, defining the contaminated plumes according to the geoelectric boundary (14 Ohm-m) defined from petrophysical modeling process. Two main

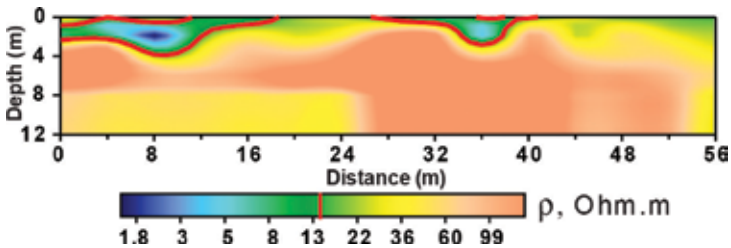

Figure 6. Geoelectric section of profile 6. Contaminated zones are delimited in depth optimizing the soil-sampling work.

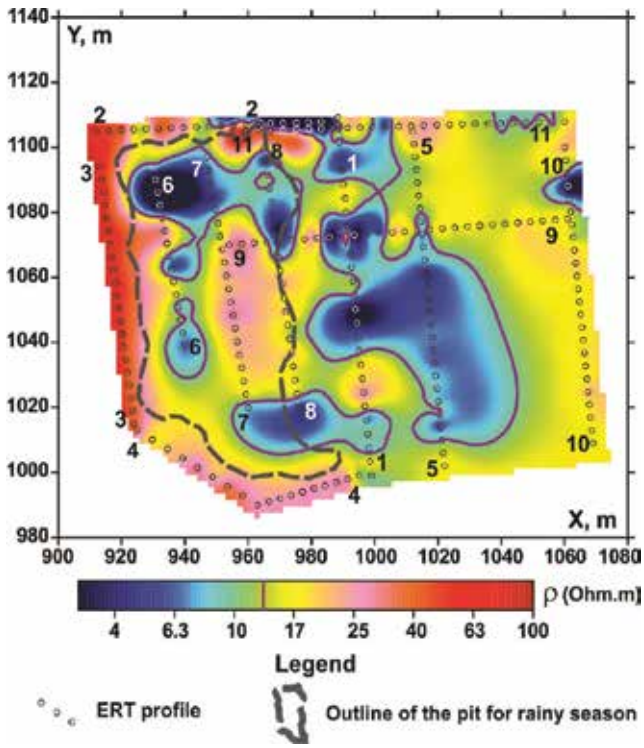

Figure 7. Resistivity map for target layer.

low-resistivity anomalies are related to high contaminated zones. The dashed line shows the pit outline (**Figure 7**).

2.6. Estimation of petrophysical parameters: determination of the volume of contaminated soil

Soil resistivity maps, determined by ERT and groundwater salinity information, were converted into petrophysical (clay content, porosity, and CEC) maps. The petrophysical parameters estimated for clean soil correspond to their true values, while values of clay content, porosity, and CEC calculated for contaminated soils do not match with their true values;

however, its high contrast (anomalous values—background) allows delineation of the contaminated zones with a high resolution. The contaminated zones are more clearly observed in petrophysical maps, with emphasis on clay content (clay content of >43%, **Figure 8**), than those in resistivity maps (**Figure 7**) for the target layer. In **Figure 8**, three main highly contaminated areas are observed in the pit zone. An additional small anomalous area is defined in the central part of the site (**Figure 8**). Using information about target layer (thicknesses from sections and areas from map), a total volume of hydrocarbon-contaminated soil of 4728 m^3 was obtained.

2.7. Determination of the aquifer vulnerability

The rural site discussed earlier did not require the analysis of vulnerability of the aquifer to hydrocarbons infiltration from the upper layers because there are no active contaminated sources and the oil spill happened over 20 years ago. Therefore, we take another rural site as an example, where 8 months after a gasoline spill caused by pipeline leakage occurred, an ERT survey was performed [5] (**Figure 9**).

A total of 174 ERT points were distributed in six profiles (**Figure 9**). A Schlumberger array with AB/2 spacing from 2 to 20 m was used. **Figure 10** shows the geoelectric section obtained

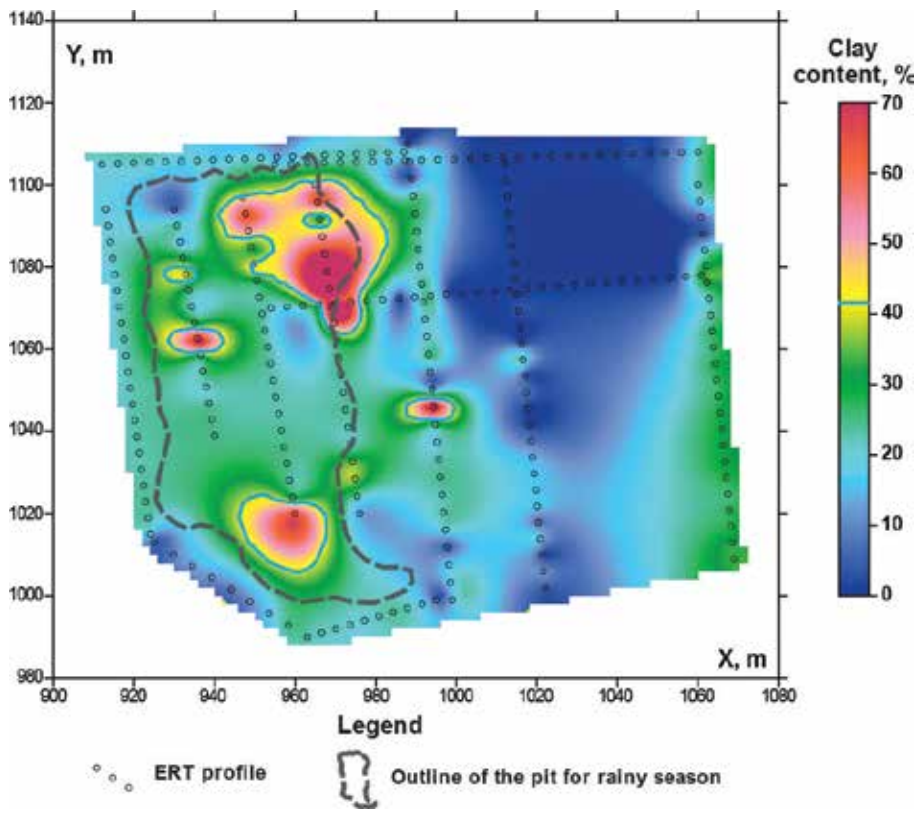

Figure 8. Clay content map for target layer of the rural site.

from ERT profile 1 (see **Figure 9**). The intermediate layer corresponds to high-resistivity sandy aquifer with a maximum clay content of 2%. The portion of the aquifer with a lower resistivity (marked by a dashed line, **Figure 9**) indicates the possible presence of matured contamination.

After determining the clay content values in each layer, the values of K can be estimated using expression (1). The clay content map for the aquitard of the site allows the estimation of a hydraulic conductivity map, which defines the areas where the aquifer is more vulnerable to infiltration of contaminants from upper layers. In **Figure 11**, four areas of the aquitard, near to spill point, with the lowest clay content (**Figure 11A**) or the highest hydraulic conductivity (**Figure 11B**) values, correspond to high aquifer vulnerability zones by infiltration (hydrogeological windows) of gasoline from the aquitard.

Using the information from different ERT sections, an aquifer resistivity map is obtained, showing the main plume associated with a detected pipe leakage point (red diamond, **Figure 12**). Note that another small contaminated zone close to another pipeline is observed in the eastern part of the site (**Figure 12**), although this claim needs to be investigated.

2.8. Estimation of migration pathways of contaminants and location of sources of contamination

Figure 13 shows an industrial-contaminated site, where the presence of mature contamination was evident. An oil-contaminated industrial site was studied using the ERT method [15]. Based on resistivity range, the configuration of the contaminated plumes and the degree of contamination were defined. The minimal anomalous resistivity values are associated with the maximum oil contamination, which is in correspondence with biodegradation process and the presence of conductive biofilm. The configuration of the surface of the maximum zone of contamination helps to locate the unknown active sources of contamination (**Figure 13**). Zoning of

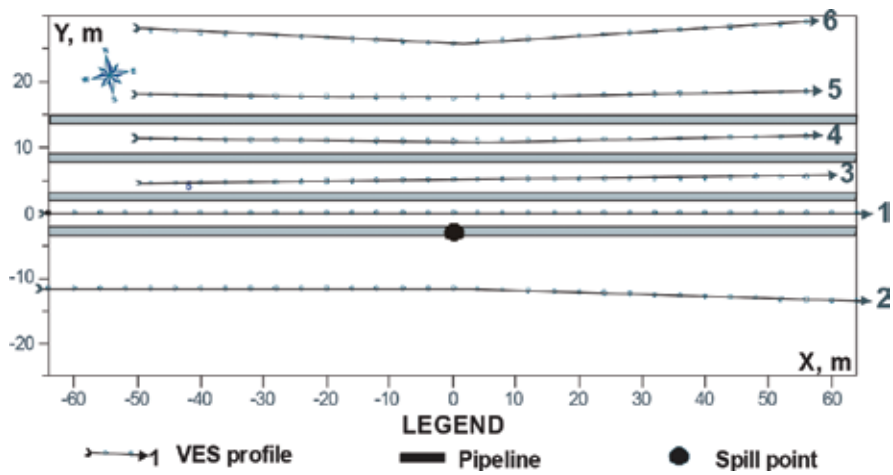

Figure 9. Scheme of the site.

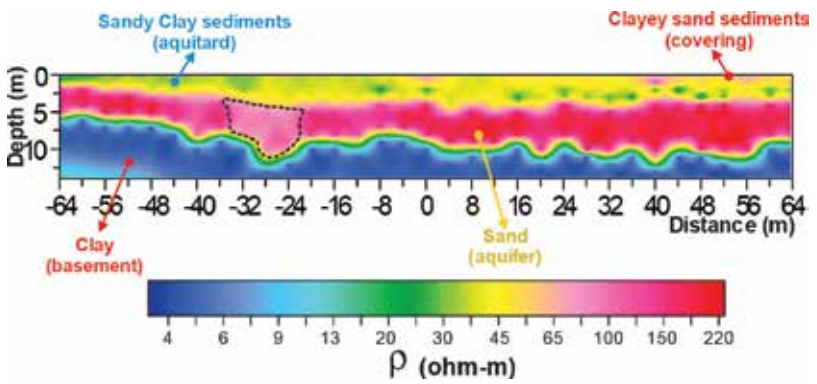

Figure 10. Resistivity section of ERT profile 1.

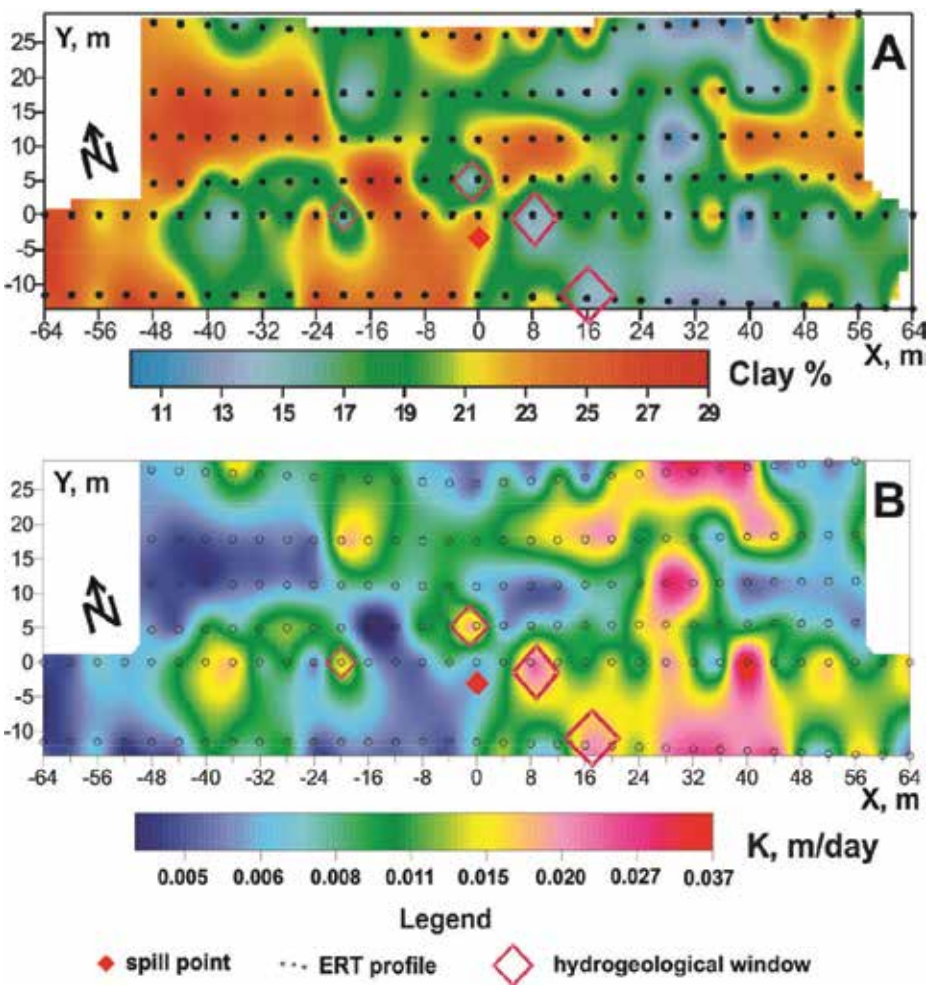

Figure 11. (A) Clay content map and (B) hydraulic conductivity map for the aquitard.

http://dx.doi.org/10.5772/intechopen.73103

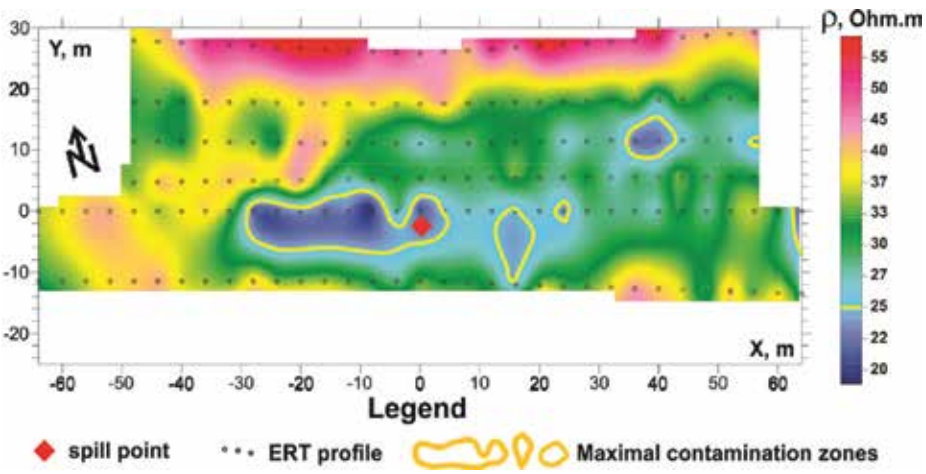

Figure 12. Resistivity map for the aquifer.

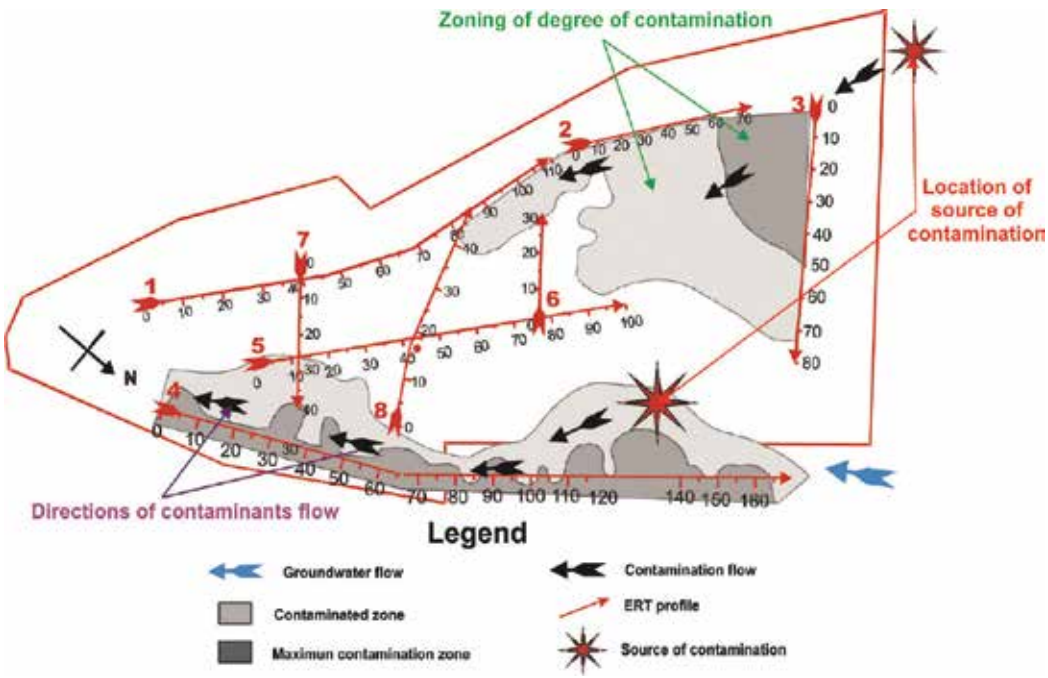

Figure 13. Determination of pathways of contaminants flow and location of sources of contamination in an industrial site.

the contaminated plume (contaminated and maximum zones of contamination) and location of sources of contamination, including information on the regional trend of groundwater flow and topographical characteristics of the site, allow the estimation of the migration pathways of contaminants in the subsurface. Two active sources of contamination, related to minor oil leakage from pipelines, were located.

3. Conclusions

The OGEOMTE effectively integrates the application of different methods and techniques such as the EMP, ERT, WRM, MRSS, and petrophysical modeling.

These methods are efficient tools for the assessment of hydrocarbons of contaminated sites. Useful results have been obtained in sites with different geological-geographical environments, including rural, urban, and industrial sites.

The application of the OGEOMET reduces the number of drillings and soil samples for chemical analysis. Based on our experience, the application of the OGEOMET can reduce the number of drills from ten to five times and the number of soil samples from 20 to 10 times.

The advantages of the application of the OGEOMET are more evident as the size and complexity of the grade of the study site increase. The whole or partial application of the OGEOMET depends on the characteristics and requirements of the study site.

Author details

Omar Delgado-Rodríguez[1]*, Vladimir Shevnin[2], Héctor Peinado-Guevara[3] and María Ladrón de Guevara-Torres[4]

*Address all correspondence to: omar.delgado@ipicyt.edu.mx

1 Division of Applied Geosciences, Potosine Institute of Scientific and Technological Research, San Luis Potosí, SLP, Mexico

2 Department of Geophysics, Moscow State University Geological Faculty, Moscow, Russia

3 Faculty of Economics and Administrative Sciences, Autonomous University of Sinaloa, Guasave, Sinaloa, Mexico

4 National Polytechnical Institute, CIIDIR-Oaxaca, Oaxaca, Mexico

References

[1] Sauck WA. A model for the resistivity structure of LNAPL plumes and their environs in sandy sediments. Applied Geophysics. 2000;**44**:151-165

[2] Abdel-Aal G, Atekwana E, Slater L, Atekwana EA. Effects of microbial processes on electrolytic and interfacial electrical properties of unconsolidated sediments. Geophysical Research Letters. 2004;**31**(12):L12505:1-4

[3] Atekwana EA, Cassidy DP, Magnuson C, Endres AL, Werkema Jr DD, Sauck WA. Changes in geoelectrical properties accompanying microbial degradation of LNAPL. Proceedings of SAGEEP (Symposium on the Application of Geophysics to Environment and Engineering Problems) 2001. pp. OCS1-OCS10. https://doi.org/10.4133/1.2922929

[4] Shevnin V, Delgado-Rodríguez O, Fernández-Linares L, Zegarra-Martinez H, Mousatov A, Ryjov AA. Geoelectrical characterization of an oil-contaminated site in Tabasco, Mexico. Geofísica Internacional. 2005;**44**(3):251-263

[5] Delgado-Rodríguez O, Shevnin V, Ochoa-Valdés J, Ryjov AA. Geoelectrical characterization of a site with hydrocarbon contamination caused by pipeline leakage. Geofísica Internacional. 2006;**45**(1):63-72

[6] Delgado-Rodríguez O, Shevnin V, Ochoa-Valdés J, Ryjov A. Using electrical techniques for planning the remediation process in a hydrocarbon contaminated site. Revista Internacional de Contaminación Ambiental. 2006;**22**(4):157-163

[7] Delgado-Rodríguez O, Flores-Hernández D, Amezcua-Allieri MA, Shevnin V, Rosas-Molina A, Marin-Córdova S. Joint interpretation of geoelectrical and volatile organic compounds data: A case study in a hydrocarbons contaminated urban site. Geofísica Internacional. 2014;**53**(2):183-198

[8] Archie GE. The electric resistivity logs as an aid in determining some reservoir characteristics. SPE-AIME Transactions. 1942;**146**:54-62

[9] Waxman MH, Smits LJM. Electrical conductivities in oil-bearing shaly sands. Journal of the Society of Petroleum Engineering. 1968;**8**:107-122

[10] Shevnin V, Mousatov A, Ryjov A, Delgado-Rodríguez O. Estimation of clay content in soil based on resistivity modeling and laboratory measurements. Geophysical Prospecting. 2007;**55**:265-275

[11] Delgado-Rodríguez O, Ladrón de Guevara-Torres M, Shevnin V, Ryjov A. Estimation of soil petrophysical parameters based on electrical resistivity values obtained from lab and in-field measurements. Geofísica Internacional. 2012;**51**(1):5-15

[12] Geonics Limited. Catalogue: Geophysical instrumentation for exploration & environment. 2012. 12 pp. Available from: http://www.geonics.com/pdfs/downloads/catalogue.pdf

[13] Shevnin V, Delgado-Rodríguez O, Mousatov A, Ryjov AA. Estimation of hydraulic conductivity on clay content in soil determined from resistivity data. Geofísica Internacional. 2006;**45**(3):195-207

[14] Loke MH, Barker RD. Rapid least-squares inversion of apparent resistivity pseudosections by a quasi-Newton method. Geophysical Prospecting. 1996;**44**:131-152

[15] Shevnin V, Delgado-Rodríguez O, Mousatov A, Nakamura-Labastida E, Mejía-Aguilar A. Oil pollution detection using resistivity sounding. Geofísica Internacional. 2003;**42**(4):613-622

Chapter 6

Characterization of Seismic Responses in Mexico City Using Hilbert-Huang Transform

Silvia Raquel García Benítez and
Leonardo Alcántara Nolasco

Additional information is available at the end of the chapter

http://dx.doi.org/10.5772/intechopen.73034

Abstract

In this investigation, we present the Hilbert-Huang transform (HHT) as an alternative technique, which has advantage over other methods for extracting useful data of seismic ground response. The HHT, integrated with the empirical mode decomposition (EMD) and the Hilbert transformation (HT), enables engineers to analyze data from nonlinear and nonstationary processes. The product of the transformation is a detailed description of time-varying frequency diagrams. The recordings of accelerations of soft-soil deposits in Mexico City are studied under this technique. Results of the analysis of accelerograms indicate that this adaptive decomposition permits the extraction motion characteristics, which cannot be effectively unraveled by other conventional data processing techniques. The findings and conclusions derived from studies such as the one presented here contribute to a better understanding of seismic response patterns.

Keywords: Hilbert-Huang transform, empirical mode decomposition, time series analysis, ground motions, fundamental frequency, peak ground acceleration

1. Introduction

The assessment of ground motions due to potential earthquakes is perhaps the most challenging problem in geotechnical earthquake engineering. Analysis of available behavioral data collected during seismic phenomena is the natural first step to approach this demand. During any seismic event, there are variations of the intensity of the ground motion with time (acceleration, velocity or displacement). After the arrival of the first seismic wave, the intensity accumulates quickly till a maximum value is sustained (for some seconds) and later diminishes gradually until it gets vanished. Additionally exists a variation of the frequency content with time with a tendency to move to lower frequencies as time progresses, what is known as "frequency dependent dispersive effect" [1].

Recognized that linear transformed domain and response spectral analysis be ill with shortcomings when applied to ground motions [2–5], this study proposes the use of the Hilbert-Huang transform (HHT) [6, 7] as an alternative for finding useful features into seismic recordings, granted its well-supported validity for dealing with nonstationary random processes [8–11]. The subject under analysis is a well-known soft-clay deposit in Mexico City, the SCT site [12–14]. The seismic response of this location is examined in order to achieve detailed information about behaviors that could not be discovered with restrictive tools. The well-defined descriptions of the time-frequency-amplitude content obtained using the HHT better describe the *nature* of the ground motions. The HHT applied to seismic phenomena results in helpful data for safer designs and improved practical earthquake engineering.

2. Hilbert-Huang transform

2.1. Overview of Hilbert-Huang transform

The HHT was proposed by Huang and coworkers [6] and consists of two parts: (1) empirical mode decomposition (EMD) and (2) Hilbert spectral analysis. Signals to be analyzed are decomposed into a finite number of intrinsic mode functions or IMFs in what is called the EMD process, the crucial part of the transformation. An IMF is described as a function satisfying the following conditions: (1) the number of extrema and zero-crossings must either equal or differ at most by one; (2) at any point, the mean value of the envelope defined by the local maxima and the envelope defined by the local minima is zero [6]. An IMF permits directly Hilbert transforms.

2.2. Hilbert spectral analysis

The Hilbert transform allows the computation of instantaneous frequencies and amplitudes and describes the signal more locally. Eq. (1) displays the Hilbert transform $\hat{y}$ which can be written for any function $x(t)$ of Lp class (the Lp *spaces* are function spaces described by a natural generalization of the p-norm for finite-dimensional vector spaces) [5]. The PV denotes Cauchy's principle value integral.

$$H[x(t)] \equiv \hat{y}(t) = \frac{1}{\pi} PV \int_{-\infty}^{\infty} \frac{x(\tau)}{t-\tau} d\tau \tag{1}$$

Huang et al. [6] and Attoh-Okine et al. [7] determined that an analytic function can be formed with the Hilbert transform pair as shown in Eq. (2).

$$z(t) = x(t) + i\hat{y}(t) = A(t)\, e^{i\theta(t)} \tag{2}$$

where

$$A(t) = \left(x^2 + \hat{y}^2\right)^{1/2}, \quad \theta(t) = \tan^{-1}\left(\frac{\hat{y}}{x}\right) \quad \text{and} \quad i = \sqrt{-1} \tag{3}$$

$A(t)$ and $\theta(t)$ are the instantaneous amplitudes and phase functions, respectively [15]. The instantaneous frequency can then be written as the time derivative of the phase, as shown in Eq. (4).

$$\omega = \frac{d\theta(t)}{dt} \tag{4}$$

Note that the analytic function $z(t)$ is the mathematical approximation to the original signal $x(t)$. Due to the fact that amplitude and frequency functions are expressed as functions of time, the Hilbert spectrum, which displays the relative amplitude or energy (square of amplitude) contributions for a certain frequency at a specific time, can be constructed as $H(\omega,t)$. **Figure 1** shows the complete block diagram of the HHT. Researchers seeking for deeper knowledge in this subject should refer to the works of [7, 16, 17].

2.3. Empirical mode decomposition

The EMD is the first stage in the HHT method. The algorithm starts to decompose almost any signal into a finite set of functions. The resulting functions are called intrinsic mode functions

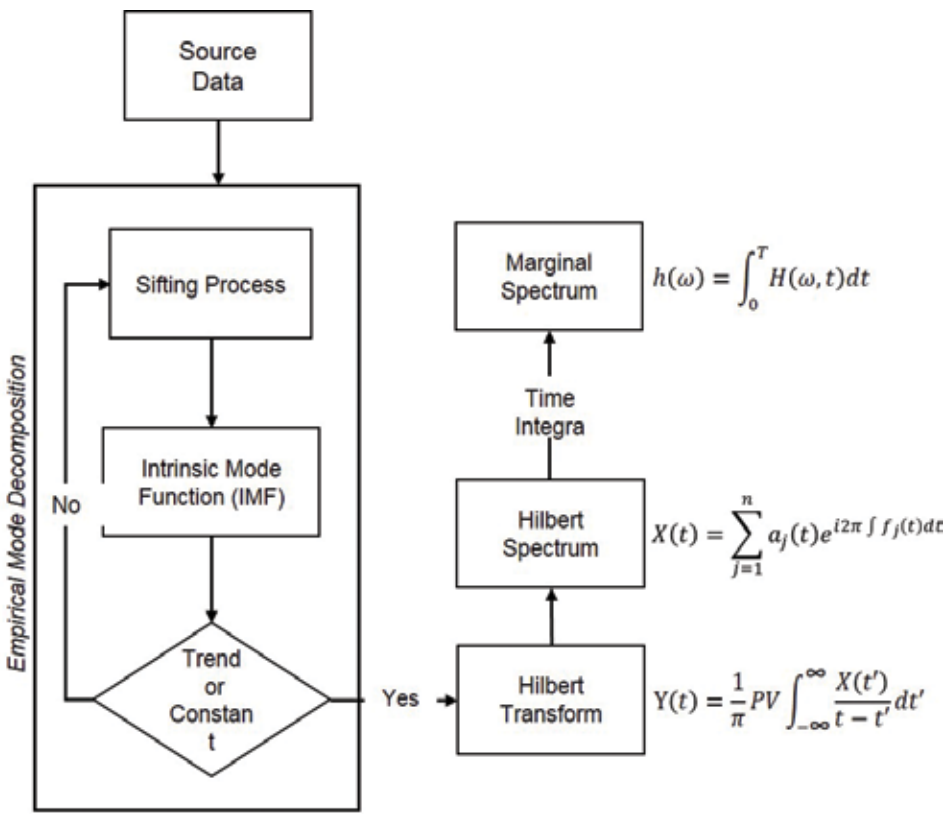

Figure 1. Hilbert-Huang transform operating diagram (modified from [18]).

(IMFs) whose Hilbert transformation gives physical instantaneous frequency values. The algorithm employs an iterative sifting process which successively subtracts the local mean from a signal, as follows:

1. Settle on the local extrema (maxima, minima) of the signal.
2. Link the maxima with an interpolation function, producing an upper envelope of the signal.
3. Link the minima with an interpolation function, producing a lower envelope of the signal.
4. Calculate the local mean as half the difference between the upper and lower envelopes.
5. Locate the local mean from the signal.
6. Iterate on the residual.

These six steps are repeated until the produced signal converges to the definition of an IMF, which is a signal with a zero mean and whose number of extrema and zero-crossings differs by at most one, considered as monocomponent functions with no riding waves [5]. Then, the IMF is subtracted from the original signal, and the sifting process is repeated on the remainder. This is iterated until the final residue is a monotonic function. The ultimate extracted IMF is the lowest frequency component of the signal, better known as the trend. The characterization of an IMF was created to guarantee that the signal gives physical frequency values when using the Hilbert transform.

Once a signal has been fully decomposed, the signal $D(t)$ can be written as the finite sum of the IMFs and a final residue, as shown in Eq. (5).

$$D(t) = R_n(t) + \sum_{j=1}^{n} IMF_j(t) \tag{5}$$

Using Eqs. (5) and (7), the analytic function can be formed as shown in Eq. (2).

$$D(t) - R_n(t) = \mathrm{Re}\left[\sum_{j=1}^{n} A_j(t)\, e^{i\left[\omega_j(t)dt\right.}\right] \tag{6}$$

Also, for reference, Eq. (6) shows the Fourier decomposition of a signal, $x(t)$.

$$D(t) = \mathrm{Re}\left[\sum_{j=1}^{n} A_j\, e^{i\omega_j t}\right] \tag{7}$$

The EMD decomposition can be considered a generalized Fourier decomposition, because it describes a signal in terms of amplitude and basis functions whose amplitudes and frequencies may fluctuate with time [5, 16]. Detailed examples of EMD can be found in [16].

3. Hilbert-Huang transformation of seismic response

3.1. Geotechnical database

To illustrate the HHT for studying seismic response of clayey soils, data recorded in the SCT site, a location in Mexico City, are analyzed. SCT is located within a densely urbanized zone,

http://dx.doi.org/10.5772/intechopen.73034

where earthquake-related damages have concentrated recurrently in the past. The data set selected for this investigation consisted of a set of 22 acceleration time series recorded during earthquakes that happened from 1985 to 2011. The characteristics of these events are enlisted in **Table 1**. The signals are of 150 s length (on average) at a measuring rate of 0.01 s. Magnitudes go from M3 to M8.1, and epicenters are from the Pacific subduction zone (in front of the Guerrero and Michoacán coasts) and normal intraplate earthquakes (located in central Mexico).

The formation is a sequence of soft clay strata interspersed with layers of harder clayey silts with sands (**Figure 2a**). The evolution of pore pressures, measured over a 12-year period (1990–2002) [19], illustrates a gradual depletion of pressures from 0.014 to 0.002 kPa/year at different depths. The water content, volumetric weight and undrained strength profiles at two different dates (1952 and 1986) are shown in **Figure 2b**. These profiles show that (1) thicknesses of the relevant clay strata have decreased as a consequence of regional subsidence; (2) water content reductions are especially significant below 15 m approximately which is consistent with the fact that pumping-induced consolidation propagates upwards from the base of the clayey soils to the surface; and (3) changes in soil density (volumetric weight) confirm that soil strata have densified as the clay masses consolidate.

Concerning the dynamic properties, the evolution on shear wave propagation velocities is presented through the field evidence given in **Figure 2d** (suspension logging tests performed

Number	Date	Focal Depth km	Magnitude	Epicentral Distance km
1	19/09/85	15	Ms=8.1	425
2	02/12/85	1	M=3	17
3	04/01/86	9	Ms=5.4	928
4	05/01/86	<5	Mc=3.5	31
5	24/10/93	19	Ms=6.6	315
6	23/05/94	23	Mc=5.6	212
7	10/12/94	20	Mc=6.3	296
8	15/07/96	20	Ms=6.5	302
9	11/01/97	16	Ms=6.9	442
10	22/05/97	59	Ms=6.0	305
11	19/07/97	5	Ms=6.3	400
12	20/04/98	66	Mb=5.9	245
13	15/06/99	69	Me=7.0	219
14	21/06/99	54	Me=6.2	267
15	30/09/99	16	Me=7.6	442
16	29/12/99	82	Mb=6.1	307
17	21/07/00	48	Me=6	145
18	09/08/00	16	Me=7.0	402
19	22/01/03	9	Ms=7.6	540
20	26/04/11	7	M=5.5	302
21	05/05/11	11	M=5.5	309

Table 1. Characteristics of seismic events.

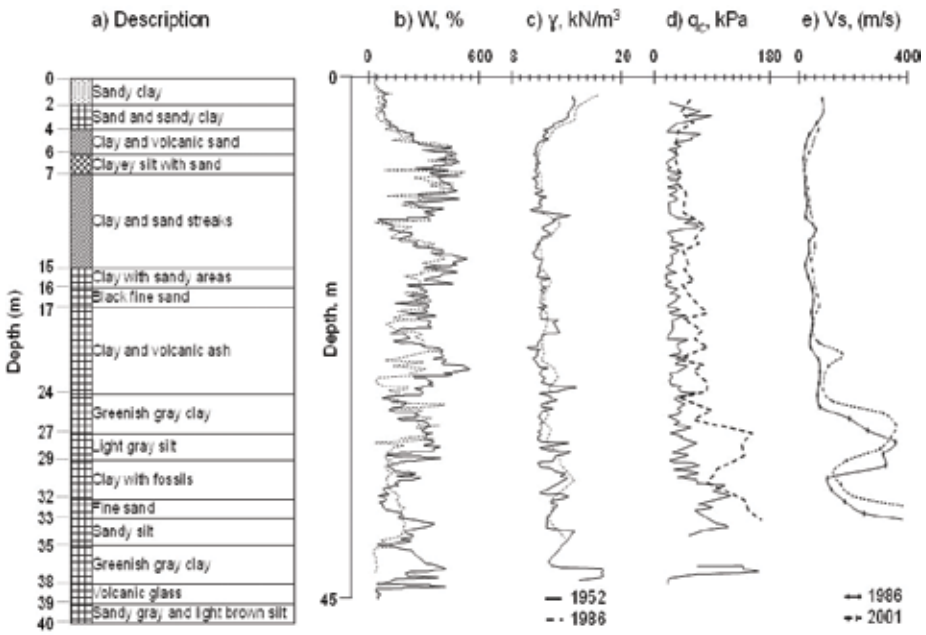

Figure 2. Stratigraphic column in SCT site, the evolution of water content W, volumetric weight ɣ, undrained strength q_c and shear wave velocity Vs profiles. (a) Description (b) W, % (c) ɣ, kN/m^3 (d) q_c, kPa (e) Vs, (m/s).

in 1986 and 2001 [20]). The expected stiffening of the clay strata over the 15 years that lapsed between dates is more evident for greater depths.

3.2. Decomposition of accelerograms

According to the procedure described above (EMD algorithm), the selected accelerograms were decomposed into their IMF components. The results are like those shown, by way of example, in **Figure 3** (IMFs obtained from the September 30, 1999 event). For this accelerogram, the algorithm yielded nine components and a residue.

To discriminate between the IMFs, they will be studied under two geotechnical-seismological parameters that are crucial for anti-seismic designs: fundamental frequency f_n and peak ground acceleration (PGA).

In Mexico City, several past earthquakes have resulted in devastating failures of built environment, which in most of the cases were attributed to strong amplification of seismic waves. For analyzing the phenomena of resonance, it is necessary to determine f_n of a soil deposit. f_n is dependent on its thickness, low strain stiffness and density. Assessment of these characteristics has been the subject of several research studies, yet inconsistencies and uncertainties associated with their estimation have not been resolved conclusively [21, 22]. Hence, many researchers tend to corroborate their calculations by using data recorded on surface during earthquake events.

http://dx.doi.org/10.5772/intechopen.73034

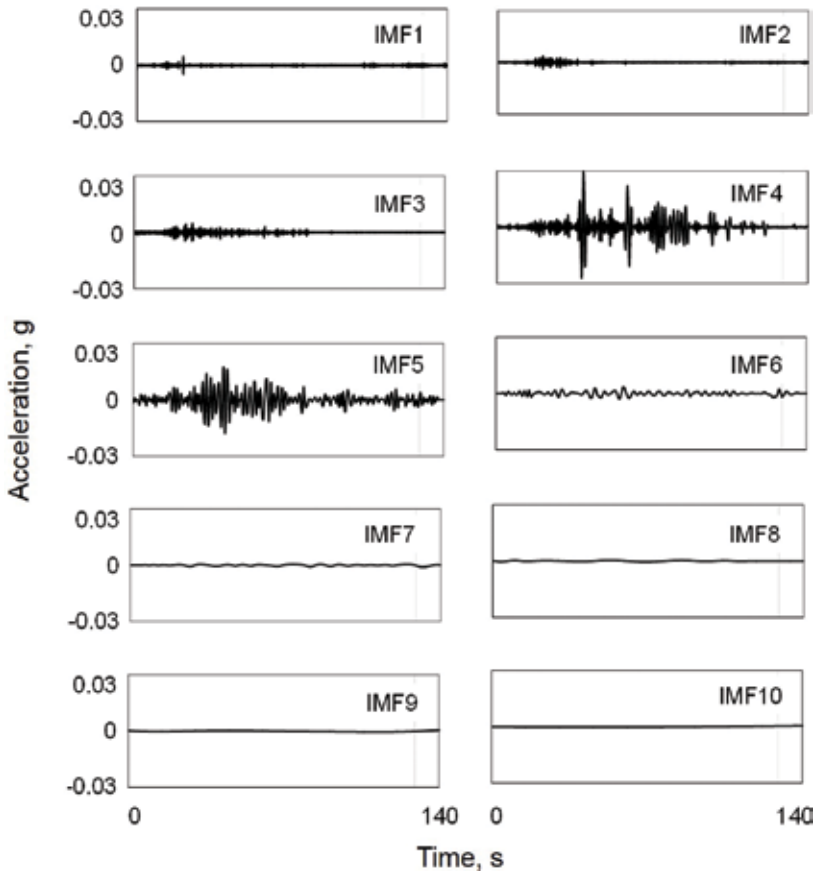

Figure 3. IMFs obtained from September 30, 1999, event.

The best tactics to establish f_n are to compute it using an abstract method and then compare this value with that shown by recorded data. Theoretically, fundamental frequency for SCT (clay deposit ≈ 40 m thick) calculated using average of shear wave velocity is $f_n = 0.5$ Hz. Using microtremors [23, 24] and multi-degree-of-freedom system (MDOF) methods [25], the computed values occur in the neighborhood of f_n ~0.47 Hz.

Attempting to relate the intrinsic oscillations with this important deposit parameter, the predominant frequency of each IMF in data set is analyzed. What follows this predominant frequency will be called f_{IMF}. In **Figure 4**, boxplots of the f_{IMF} corresponding to each mode are depicted. The first (IMF1) and last modes (IMF6 to IMF10) are not in the graph. The IMF1s have flat spectra where it is not possible to determine a predominant frequency. The last modes (from IMF6 to IMF10) have very short box sections with exceptionally low frequency values (near to zero). These modes, in terms of their fundamental frequency, are considered irrelevant, that is, they do not have effect on the analysis of the measured response.

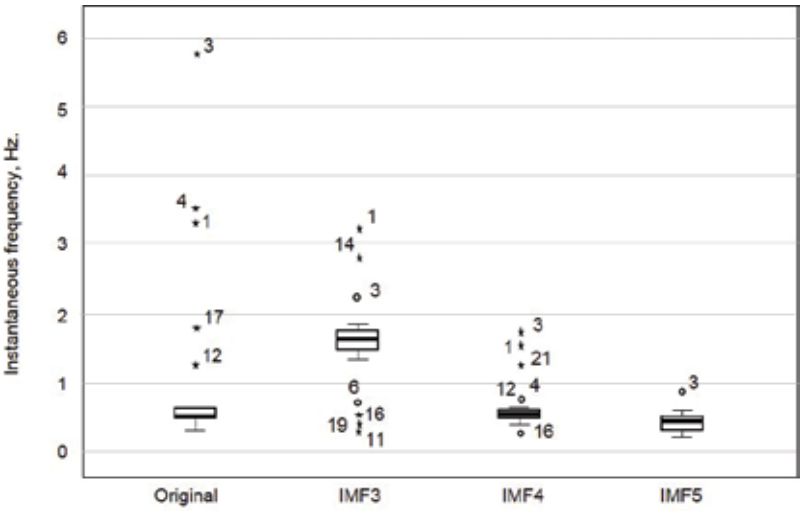

Figure 4. Boxplot of IMF, excluding the corrupting and irrelevant modes.

Despite the range of magnitudes, epicentral depths, generating mechanisms, directivity and dates, the f_{IMF} of IMF5 is closely related to the natural frequency of SCT site. The f_{IMF} of IMF5 practically does not change, and this is noticeable in the condensed box. The dispersion is minimal, and it should be noted that this graph includes minor events ($M < 4$) and the extreme earthquake of 1985 (M8.1). On the other hand, the median of the f_{IMF} of IMF3 is comparable to the second vibrate mode f_2 (using the MDOF method [23], f_2 is ~1.4 Hz). Its boxplot is taller than the IMF5 and has evident dispersion in lower and upper whiskers.

Mexico City's seismic response has changed over the years. The numerous efforts made to analyze this phenomenon showed that the response may be due to land subsidence (consequence of water extraction) [19, 20]. Since the pumping and the capacity of the clay strata to expel water are quite different at each geotechnical zone of the city, the effect on seismic response is a complex problem.

To guarantee safe structural designs, the most significant aspect to be demonstrated is the effect of the subsidence on the spectral ordinates (with respect to the current values specified for design purposes) and the relative values of the structures and site periods. With specific geotechnical and geological information, Avilés et al. [26] presented an incremental procedure to evaluate the progressive evolution of f_n over time, in order to evaluate the effects of these changes on the earthquake ground response. The adjustments expected in selected values of f_n, from 1980 to 2020, can be appreciated in **Figure 5**. What can be anticipated, as the evolution of this phenomenon, is that after the initial reference year the parameter decreases monotonically as the times span increases [27].

Observe what occurred when the values of f_n, from original data, are superimposed in the graph. The frequencies obtained from the recorded accelerograms hardly follow the trend set by [26]. Most events do not fit the specific curve for SCT ($1/f_n = 2$), and the expected drop patterns of f_n cannot be verified. However, the behavior shown by the IMF3 and IMF5 fits very well to the decrement curves obtained with the iterative model. The f_{IMF} of IMF5 fits the theoretical curve of

http://dx.doi.org/10.5772/intechopen.73034

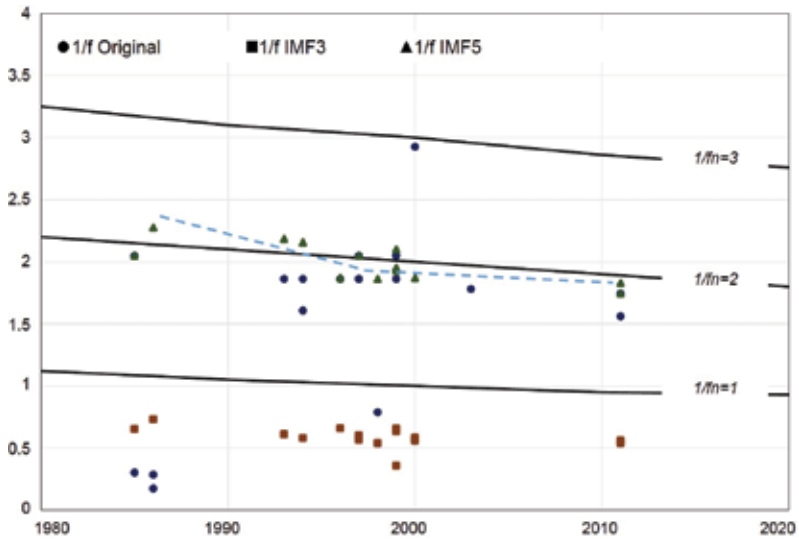

Figure 5. Evolution of f_n, continuous line results from [26]. Dashed line represents the behavioral trend of f_{IMF}-IMF5.

$1/f_n = 2.0$. This finding reinforces the hypothesis about stiffening of the clayey strata that are not possible to verify using the f_n from registered data. Actually, a deep analysis of the path shown by f_{IMF}-IMF5 could drive to two stages of the evolution: the first one with a more dramatic decrement of the $1/f_n$ since 1985 (or before) and toward the year 2000, and a second one where the frequencies change more slowly to the present day. The model's tendency that drops the values of $1/f_n$ less dramatically over time is clearly illustrated with the aligned values of f_{IMF}-IMF3.

PGA, as the maximum ground acceleration that occurred during earthquake shaking at a location [28], is used as an intensity measurement, and the design-basis-earthquake ground motion is often defined in terms of PGA [29]. Even damage to buildings and infrastructure is more closely related to ground motion, of which PGA is a measure, rather than the magnitude of the earthquake itself [30].

The boxplots of the maximum instant amplitudes, associated with each IMF, are shown in **Figure 6a**. The most extreme points (marked with the numbers 2 and 15) are two of the most intense seismic events registered in Mexico City (M > 7.0), being the extreme value the devastating 1985 Michoacán earthquake (M8.1).

Isolating the M8.1 event to properly observe the characteristics of each box (**Figure 6b**), it is evident that last modes have very small boxes. Considering this minor amplitudes and their fundamental frequencies (very close to zero), we conclude that they are irrelevant modes. Examining the relatively small box of the IMF1 maximum amplitudes, it was found that the extraordinary earthquake of 1985 is found inside the rectangle. It seems that this first oscillation does not respond to the input energy as the other modes do, so it is inferred that a mechanism, other than the ground motion itself, is the one that controls this oscillation. Based on this observation and their flat Fourier spectra, the IMF1 is labeled as a mode that "corrupts" the registered motion of the soil deposit.

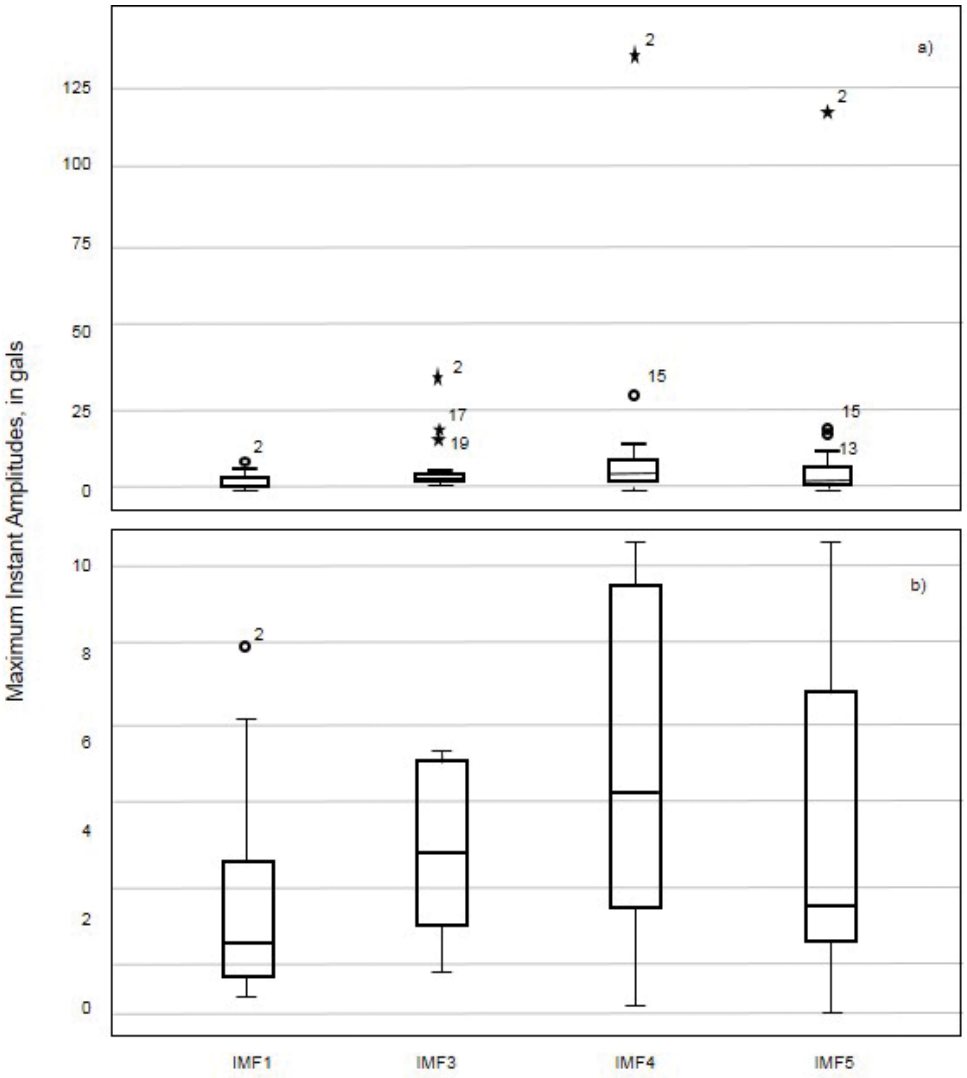

Figure 6. Boxplot of MIAs according to the IMF, (a) the whole set, including 19/09/85 Michoacán earthquake and (b) events with M ≤ 7.5.

It can be seen that the energy is concentrated mainly on fourth and fifth oscillations. These modes most react to the extreme earthquake of 1985. The dispersion is minimal, and the atypical event (M8.1) is certainly at a distance, which does not happen with the other oscillations. It appears that the recognized amplification potential of this soft-clay site [20] is mainly evident for the central modes.

The "corrupted" (IMF1) and the irrelevant modes (IMF6 to IMF10) were removed from the registered accelerograms. The response spectra of accelerations from both sets of signals, the original and the "cleaned," are calculated. Some selected responses are depicted in **Figure 7**. These are examples of responses that can be reproduced with the IMF3 or IMF5 with adequate approximation. The energy-frequency content of the original response spectra is represented

http://dx.doi.org/10.5772/intechopen.73034

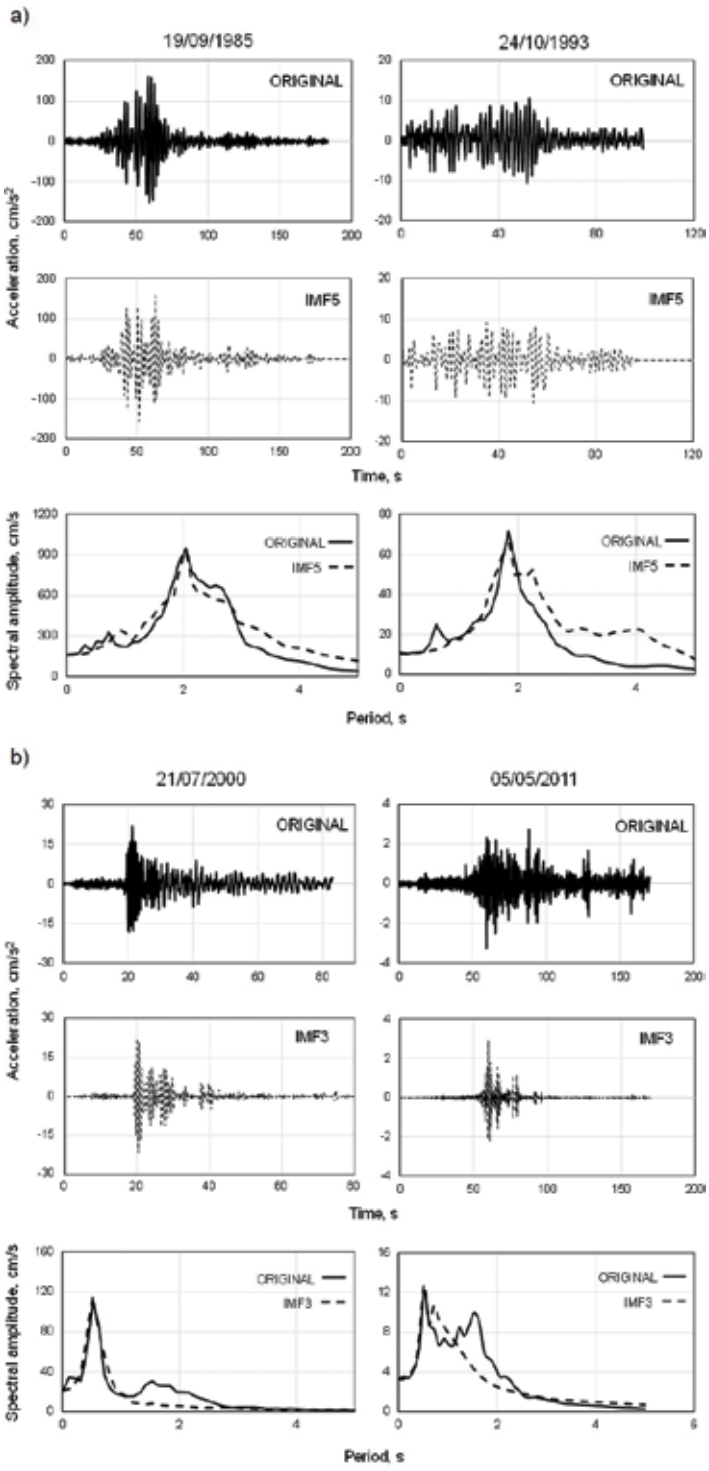

Figure 7. Examples of spectra evaluated using original signals and selected IMFs, (a) events better represented with IMF5 and (b) events better represented with IMF3.

with one intrinsic mode, the one with a MIA near to the PGA registered. It has been found that the most intense events from the Pacific subduction zone tend to be related mainly with the *fifth* mode, while for minor and intraplate events, the ground motion can be represented using only the *third* mode. Deep examinations are necessary to clarify this finding, but the advantages of EMD when analyzing complex responses are clear.

It should be emphasized that the "cleaned" signals represent simpler and easier time series, with desirable density for minimizing computational costs (when running complex ground-motion models).

3.3. Hilbert spectra of ground motions

The nonrecommended practice of using Fourier for studying nonstationary-nonlinear data is revealed as a limitative tool for these kinds of analyses since it cannot show the detailed information about the peculiarities of the energy-frequency distribution, aspect that is utilized, for example, to conclude about site effects.

From the Hilbert spectra, events in the database have direct important characteristics such as the arrival time and the duration of intense phase of the earthquakes can be detected. In addition to the well-defined zone of maximum accelerations, the huge variations of the response frequencies between the beginning (the maximum amplitude cycles) and the end of the event can be clearly detected and quantified

(see, for example, the HS events in **Figure 8**). Although most of the events found in the database have disseminated energy in the high-frequency range, this is minor compared to the highest levels recorded in the entire time series. The persistent energy resides along horizontal packets below 1 Hz. It is easy to detect the peak accelerations of each response (in addition to the concentric energy surrounding these maxima), the fundamental frequencies, and the duration of the arrival packets. The "corrupted" oscillations can be distinguished, with low frequencies and low constant amplitudes that are maintained from the beginning to the end of the record.

The difficulty of transforming signals from near-field motions (time series of short duration) to Fourier spectra is not a problem using HS (see, for example, the HS of the June 15, 1999 event). The frequency distribution clearly shows the energy content along the frequency axis (from 0.4 to 0.8 Hz), and it is quite easy to determine the resonant frequency of the site (at ≈0.55 Hz) and the associated energy density.

In **Figure 9**, three of the most intense earthquakes registered in Mexico City are shown. They are the well-known 1985 and the most recent devastating events, September 8, 2017, and September 19, 2017. While the responses to minor earthquakes have a much wider energy distribution, the content for these events is quite different. The spikes are more evident, and they can be located around the PGA. Although these Hilbert spectra have the decreasing trend in energy density as a function of frequency, as the other events, these spectra show a visible lack of energy in the low-frequency range (less than 0.2 Hz).

Consider the HS of September 19, 2017 earthquake, the one that hit the city and collapsed a large number of buildings, houses and underground facilities. It is well defined at the low-frequency range (from 0.4 to below 1 Hz) where maximum amplitudes were present, a serious situation for the high-rise structures. The peak of energy, located at a very narrow frequency

http://dx.doi.org/10.5772/intechopen.73034

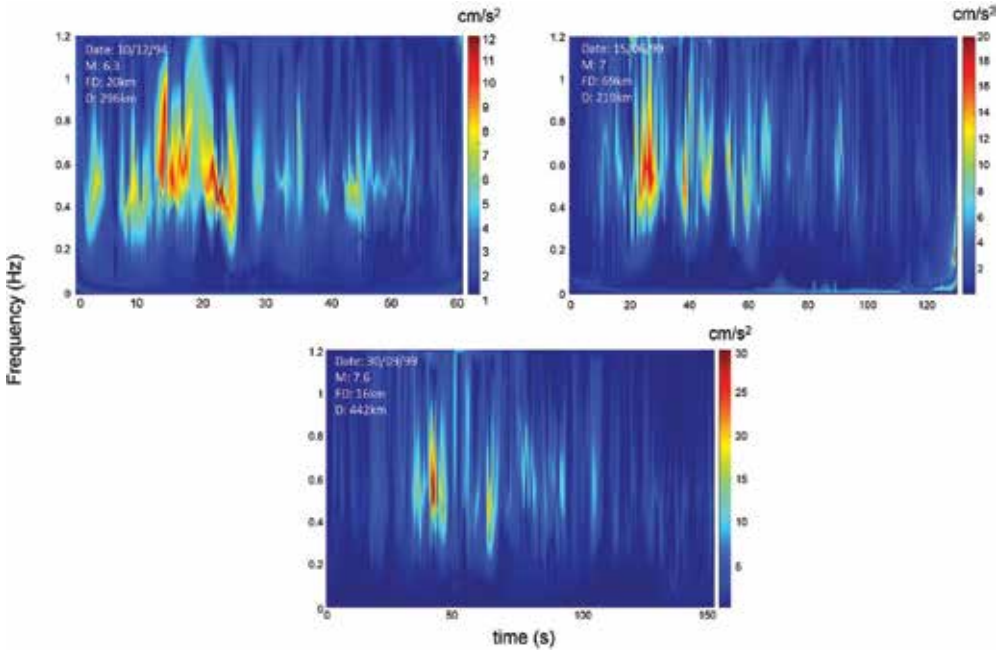

Figure 8. The HS for selected intraplate and interplate events. Significant frequency deviation during the strong motion showed that the energy is concentrated below 1 Hz.

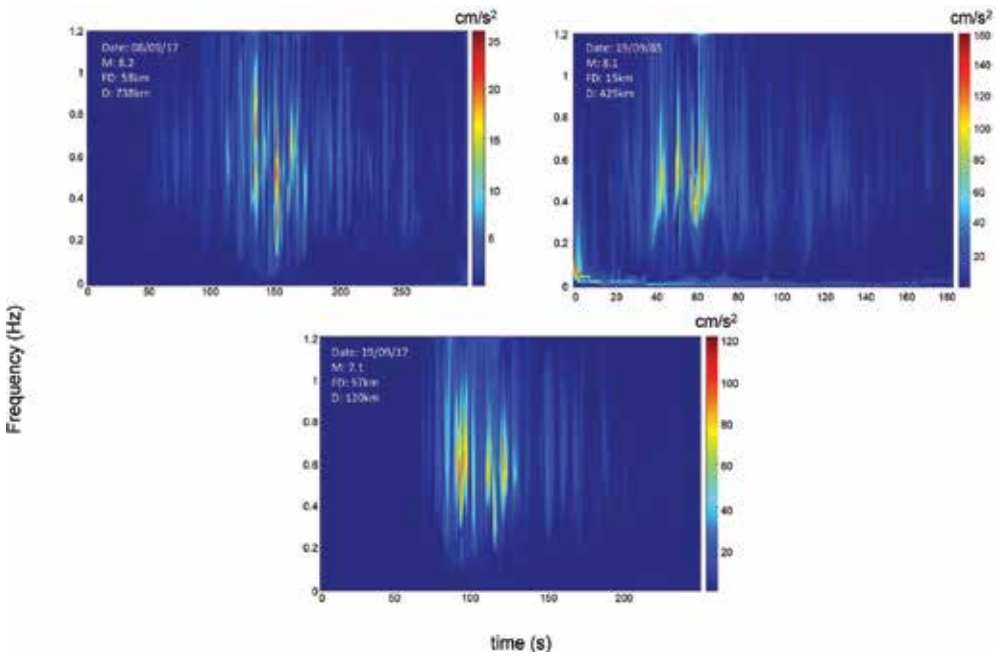

Figure 9. The historical 1985 earthquake (M8.1) and the responses registered during September 8, 2017 (M8.2) and devastating September 19, 2017 (M7.1).

range (0.5–0.8 Hz), could be responsible for the huge number of damaged buildings in a defined geotechnical area of the city. Similarly, to the spatial variation of the destruction at Mexico City during the 1985 earthquake, for this event some areas have been recognized, with special stratigraphies, which presented amplification potentials never seen before. As many investigators have concluded, any linear model could not predict this kind of ground responses.

4. Conclusions

The decomposed components, namely IMFs, contain observable, physical information about the ground motion. Owing to the fact that the intrinsic oscillations can be related to the phenomena without restrictive hypothesis, the conclusions obtained from the behavior of each mode are more *natural* than those achieved from theoretical positions faraway the system, which generates the signal.

Despite the fact that the soil properties in the SCT site have changed because of regional subsidence, the recorded accelerations do not seem to exhibit the expected stiffening effect. What is shown in this research is that the time series, which serve as a basis for showing the soils hardening, are *corrupted* by external oscillations that mask actual responses. It was recognized that IMF5 and IMF3 actually showed the decrease in rate of the frequencies postulated in theoretical models. By detecting the oscillations that do mainly correspond to the *real* ground motion, the EMD is presented as an alternative tool for finding directly the frequencies related with the highest energy concentrations.

The usefulness of these finding points to the need for further investigation in evaluating the competency of tools for analyzing the recordings and for obtaining conclusions, since they are the basis of the process of calibration of all the theoretical, geotechnical and seismological models.

The Hilbert spectral transformation permits the recognition of oscillation modes that would have been masked by Fourier spectral analysis.

Acknowledgements

The accelerogram records for this research were provided by the Unidad de Instrumentación Sísmica, Instituto de Ingeniería, UNAM.

Author details

Silvia Raquel García Benítez* and Leonardo Alcántara Nolasco

*Address all correspondence to: sgab@pumas.iingen.unam.mx

Researcher, Geotechnical Department, Instituto de Ingeniería, Universidad Nacional Autónoma de México, México City, México

References

[1] Jousset P, Neuberg J, Jolly A. Modelling low-frequency volcanic earthquakes in a viscoelastic medium with topography. Geophysical Journal International. 2004;**159**:776-802

[2] Valerio J. Spectral analysis of earthquake accelerations as realizations of a non-stationary stochastic process. In: Proceedings of 10th World Conference on Earthquake Engineering. Vol. 2. 1992. pp. 901-907. http://www.iitk.ac.in/nicee/wcee/article/10_vol2_901.pdf

[3] Cohen L. Time-Frequency Analysis. Prentice Hall: Technology & Engineering; 1995. p. 299

[4] Shumway RH, Stoffer DS. Time Series Analysis and Its Applications: With R Examples. 3rd ed. New York: Springer; 2011. p. 202. ISSN: 1431-875X, ISBN: 978-1-4419-7864-6. DOI: 10.1007/978-1-4419-7865-3

[5] Huang NE, Shen Z. Interdisciplinary mathematical sciences. Vol. 16. In: Huang NE, editor. Hilbert–Huang Transform and Its Applications. London: World Scientific 2015. p. 400. ISBN-13: 978-9814508230, ISBN-10: 9814508233

[6] Huang NE, Shen Z, Long SR. The empirical mode decomposition and the Hilbert spectrum for nonlinear and non-stationary time series analysis. Proceedings of the Royal Society of London A. 1998;**454**(1971):903-995

[7] Huang NE, Attoh-Okine N. The Hilbert-Huang Transform in Engineering. 1st ed. Boca Raton: CRC/Taylor & Francis; 2005. 328 p. ISBN: 978-0849334221

[8] Zhang R. The role of Hilbert-Huang transform in earthquake engineering. In: Proceedings of the World Multiconference Systemics, Cybernetics Informatics; Orlando. Vol. XVII. 2001

[9] Huang NE et al. A new spectral representation of earthquake data: Hilbert spectral analysis of Station TCU129, Chi-Chi, Taiwan, 21 September 1999. Bulletin of the Seismological Society of America. 2001;**91**(5):1310-1338

[10] Loh CH, Wu TC, Huang NE. Application of the Empirical mode decomposition-Hilbert spectrum method to identify near-fault ground-motion characteristics and structural responses. Bulletin of the Seismological Society of America. 2001;**91**(5):1339-1357

[11] Yang JN. System identification of linear structures based on Hilbert-Huang spectral analysis. Part 2: Complex modes. Earthquake Engineering Structural Dynamics. 2003;**32**(10):1533-1554

[12] Díaz-Rodríguez JA, Leroueil S, Alemán JD. Yielding of Mexico City clay and other natural clays. Journal of Geotechnical Engineering. 1992 Division, ASCE. **118**(7):981-995

[13] Díaz-Rodríguez JA, Lozano-Santa Cruz R, Dávila Alcocer VM, Vallejo E, Girón P. Physical, chemical, and mineralogical properties of Mexico City: A geotechnical perspective. Canadian Geotechnical Journal. 1998;**35**(4):600-610

[14] Díaz-Rodríguez A. Los suelos lacustres de la Ciudad de México. Revista Internacional de Desastres Naturales, Accidentes e Infraestructura Civil. 2006;**6**(2):111

[15] Yangkang C, Chao Z, Jiang Y, Zhaoyu J. Application of empirical mode decomposition in random noise attenuation of seismic data. Journal of Seismic Exploration. 2014;**23**:481-495

[16] Huang NE, Wu Z. A review on Hilbert-Huang transform: Method and its applications to geophysical studies. Reviews of Geophysics. 2008;**46**(2):1-23

[17] Huang NE, Shen SSP. Hilbert-Huang Transform and Its Applications. London: World Scientific; 2005. ISBN: 978-9812563767

[18] Lee MH, Shyu KK, Lee PL. Hardware implementation of EMD using DSP and FPGA for online signal processing. IEEE Transactions on Industrial Electronics. 2011;**58**(6): 2473-2481

[19] Ovando-Shelley E, Romo MP, Contreras N, Giralt A. Effects on soil properties of future settlements in downtown Mexico City due to ground water extraction. Geofísica Internacional. 2003;**42**(2):185-204

[20] Ovando-Shelley E, Ossa A, Romo MP. The sinking of Mexico City: Its effects on soil properties and seismic response. Soil Dynamics and Earthquake Engineering. 2007;**27**:333-343

[21] Pando M, Cano L, Suárez L, Ritta R, Montejo L. Comparison of site fundamental period estimates using weak-motion earthquakes and microtremors. In: The 14th World Conference on Earthquake Engineering. 2008. http://www.iitk.ac.in/nicee/wcee/article/14_02-0142.pdf

[22] Demetriu S, Trandafir R. Time-frequency representations of earthquake motion records. Analele Stiintifice ale Universitatii Ovidius Constanta. 2003;**11**(2):57-68

[23] Lermo J, Chávez-García F. Are microtremors useful in site response evaluation? Bulletin of the Seismological Society of America. 1994;**84**(5):1350-1364

[24] Ordaz M, Miranda E, Avilés J. Proposal for seismic design spectra for Mexico's Federal District. Ingeniería de Estructuras. 2003;**8**(2):189-207

[25] Bozorgnia Y, Bertero V. Earthquake Engineering: From Engineering Seismology to Performance-Based Engineering. Boca Raton: CRC Press; 2004. p. 976. ISBN: 0-8493-1439-9 (alk. paper)

[26] Avilés J, Pérez-Rocha L. Regional subsidence of Mexico City and its effects on seismic response. Soil Dynamics and Earthquake Engineering. 2010;**30**:981-989

[27] Yin JH, Graham J. Elastic visco-plastic modelling of one dimensional consolidation. Geotechnique. 1996;**46**(3):515-527

[28] Douglas J. An investigation of analysis of variance as a tool for exploring regional differences in strong ground motions. Journal of Seismology. 2004;**8**(4):485-496

[29] Noeggerath J, Geller RJ, Gusiakov VK. Fukushima: The myth of safety, the reality of geoscience. Bulletin of the Atomic Scientists. 2011;**67**:37

[30] Campbell KW, Bozorgnia Y. Updated near-source groundmotion (attenuation) relations for the horizontal and vertical components of peak ground acceleration and acceleration response spectra. Bulletin of the Seismological Society of America. 2003;**93**:314-331

Section 3

Earth Planetary System

Chapter 7

Dynamics of the Early Stage of Formation of the Earth's-Moon System

Yurie Khachay, Olga Hachay and Alexander Antipin

Additional information is available at the end of the chapter

http://dx.doi.org/10.5772/intechopen.72641

Abstract

In previous studies it was shown that the energy release during the decay of short-living radioactive elements in small bodies is sufficient for the temperature inside such a protoplanetary core to become larger than the melting temperature of iron. This ensures the realization of the process of differentiation of matter and the development of convection in the inner envelopes. At all stages of proto-Earth's formation, convective heat and mass transfer is the most important factor in the dynamics of the planet. However, the release of heat due to friction in the viscous liquid of the outer regions of the core so far has not been taken into account at all or was taken into account only in the formed envelopes of a planet of constant radius. In this chapter, we present the results of a numerical simulation of the thermal evolution of a 3D spherical segment of a protoplanet of an increasing radius, taking into account the accidental falling of bodies and particles. An algorithm for the numerical solution of the problem is given, taking into account the dissipation of tidal energy in the Earth-Moon system at the stage of planetary accumulation.

Keywords: stage of Earth-Moon forming, temperature distribution, energy of Moon tides, numerical solution of the differential system of equations

1. Introduction

It is a paradox, but there are no significant differences regarding the earliest stages of the forming of the universe and its structure. The basis of modern concepts is the law of gravitation of Einstein A [1]. Unlike Newton's law of gravitation, this potential explicitly takes into account the time dependence and the finite velocity of the gravitational interaction distribution. The initial condition for the Einstein equation is a point singularity in which the mass of the entire substance of the universe is concentrated. Friedman A [2] for the first time obtained

no stationary solutions of the gravitational equation had been published. After Hubble's experiment on installed "red shift" [3] in the spectra of stars and galaxies, and then of "relict" radiation [4], the idea of the universe expanding was established. At the same time, our universe is understood as a region, about 13.8 billion light-years in radius, filled with matter formed after the "Big Explosion."

However, new questions arise. What is beyond the boundaries of our universe? Is the Universe only one? Are there any measurable physical fields and processes that will allow us to detect real objects external to our universe? A singular point has arisen in the already existing universe, and can we then trace the development of the instability leading to the 'Big Explosion" of this singular object? Are the laws of physics established in our universe in the outer universes preserved? Clearly, this is only a small part of the issues related to the problems of cosmic physics and planetology.

It is believed now that the most justified are ideas about the formation of stars and planets in protoplanetary clouds inside spiral arms of galaxies. **Figures 1** and **2** show an example of such galaxies.

The evolution of our solar protoplanetary cloud has been studied in detail. This is a vivid example of how complex are the processes of formation of the inner shells of the Earth and its natural moon satellite are insufficiently researched. Despite significant achievements, until recently, it has not been possible to obtain a quantitative explanation of the results obtained on the basis of the analysis of W-Hf and Al-Mg isotope systems, which are interpreted as evidence of the very early separation of chemical reservoirs of the core and mantle in time less than 10 million years [5–7]. While on the basis of the results on the uranium-lead system, the formation of these structures lasted about 100 million years, that is, the separation of their chemical reservoirs occurred long before the end of the growth of the structures themselves.

Figure 1. Impacted galaxies.

http://dx.doi.org/10.5772/intechopen.72641

Figure 2. Star RS Korma ESO/G. Bono and CTIO. http://www.eso.org/public/images/potw1126a/

2. Modeling of early stage of formation of the Earth and Moon

2.1. The main physical results and mathematical formulation of the problem

Initially, a one-dimensional model was used to solve the problem of early stage of the Earth's formation [8, 9]. Adiabatic stresses and three-dimensional effects due to the location of bodies on the surface of a growing planet have not been taken into account. The main source of internal energy of the protoplanet at this stage of its formation was the release of heat due to the natural radioactive decay of long-living uranium and thorium. The contribution due to the release of heat from the impact of small particles and bodies of the protoplanetary cloud on the surface of the growing planet had been known to be very small, since most of their energy, according to Stefan's law, was released into space. As a result, sufficiently low estimates of the temperature of the inner regions of the protoplanet were obtained by the end of the process of their accumulation (**Figure 3**).

As can be seen from these results, the temperature estimates obtained turned out to be lower than the melting point of iron at a given depth. From this it follows that since the values of the iron coefficient in a solid silicate substance are very small, then for the entire age of the Earth, the separation of a predominantly iron core from a predominantly silicate mantle could not occur. In order for such separation to be realized, the molten state of the substance and the convective heat and mass transfer of the components in the melt are required.

A new model for the accumulation of terrestrial planets was proposed in the work of [11, 12], which uses modern results of isotope geochemical analyses and allowed obtaining reliable estimates of the concentration of short-living naturally radioactive isotopes and, above all, 26Al in the matter of the protoplanetary cloud. On the basis of these data, new estimates of

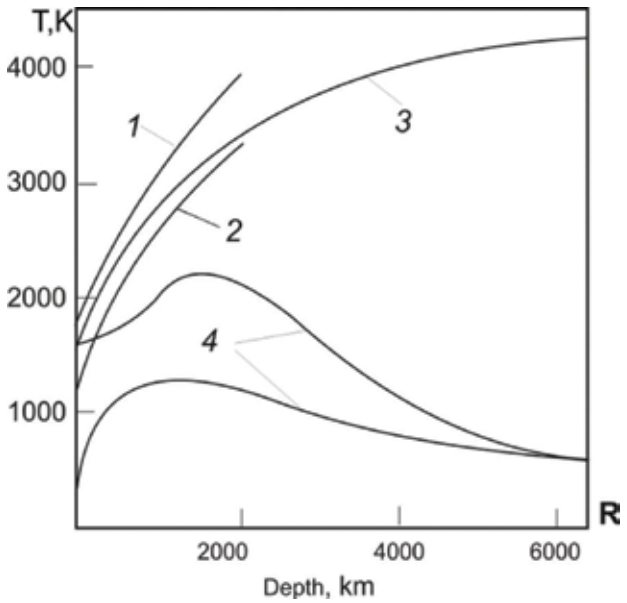

Figure 3. The Earth's temperature distribution after the end of accumulation. 1—The temperature of full mantle material melting, 2—the temperature of the solid mantle, 3—the melting iron temperature, 4—the temperature distribution into the Earth by Safronov [8] (lower curve) and the temperature distribution into the Earth by Lubimova (upper curve) [10].

the temperature distribution in the growing pre-planetary bodies of the planet in the "feeding" zone of the Earth were obtained. It was shown in the work of [11] that the energy release during the decay of short-living radioactive elements in small bodies is sufficient for the temperature inside such a protoplanetary core to become greater than the melting temperature of iron. This ensures the realization of **Table 1** which illustrates the processes of matter density differentiation and the development of convection in the inner envelopes. Originally, a one-dimensional model was used to numerically solve that problem, based on new data on

Radius of the pre-planetary body, km	**Concentration of Al_2O_3 mass. %**			
	1.0	**3.0**	**4.6**	**9.0**
	Temperature into the pre-planetary body center, K			
5	1240	1701	1734	1825
100	1676	1752	1812	1978
150	1690	1793	1876	2104
200	1701	1828	1928	2206
250	1711	1856	1972	2290
300	1718	1878	2006	2359
400	1730	1912	2059	2461

Table 1. The dependence of the temperature in the center of the pre-planetary body from the content of Al_2O_3 [12].

the content of 26Al in the protoplanetary matter of the Earth. The results are presented in **Figures 4** and **5**. To describe the growth of the mass of the protoplanet and the nearest satellite, the Safronov equation was used [8, 10]:

$$\frac{\partial m}{\partial t} = 2(1+2\theta)\, r^2\, \omega\left(1-\frac{m}{M}\right)\sigma \tag{1}$$

where m is the current mass of the growing body, M is the final mass of the planet, r is the radius of the growing protoplanet, θ is the statistical parameter that takes into account the distribution of bodies and particles by mass and velocity in the protoplanetary supply zone, σ is the surface density of the protoplanetary cloud's matter in the orbit of the growing body, and ω is the angular velocity of the orbital rotation. The change of the temperature in the inner parts of the growing planets was described by a system of equations:

$$\rho\left(\frac{\partial \vec{V}}{\partial t}+\vec{V}(\nabla\vec{V})\right) = -\nabla P+\mu\Delta\vec{V}+2\rho\vec{V}\times\vec{\Omega}-\rho\nabla W \tag{2}$$

$$\frac{\partial T}{\partial t}+\vec{V}(\nabla T) = \chi\Delta T+Q_1 \tag{3}$$

$$div\vec{V} = 0 \tag{4}$$

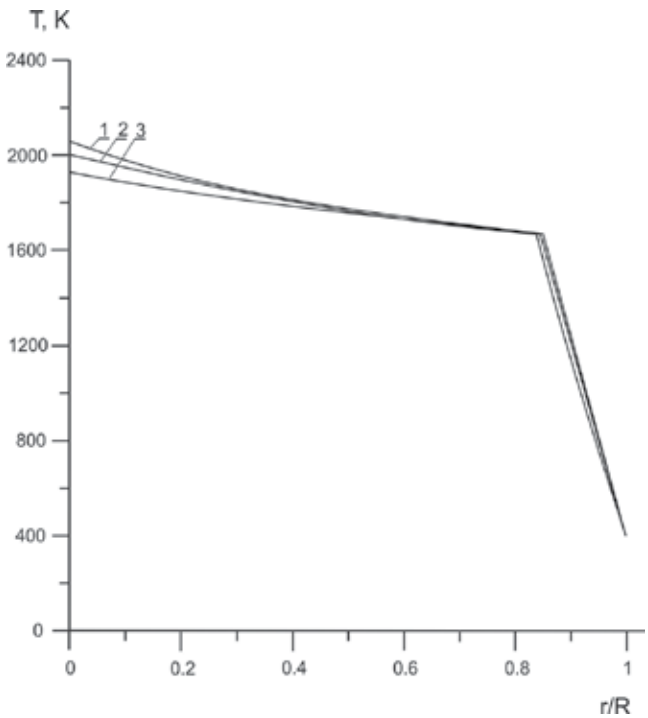

Figure 4. The distribution of the temperature in the growing pre-planetary body. Its radius is 1—400 km, 2—300 km, and 3—250 km.

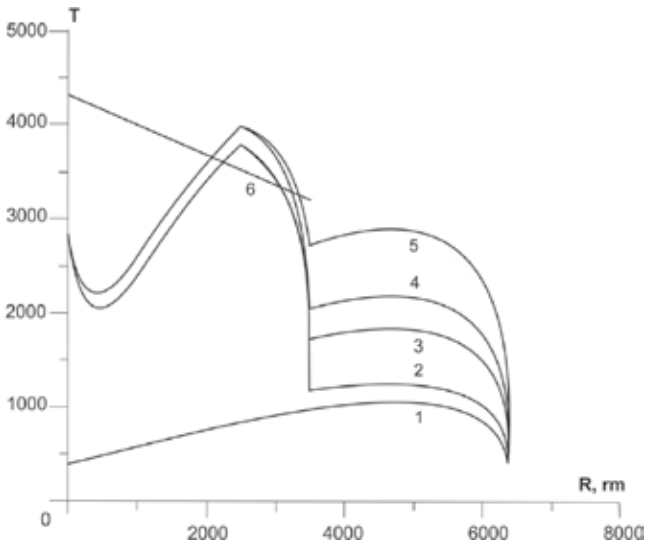

Figure 5. Possible variants of the temperature distributions to the moment, when the Earth has the size 6300 km [12]. 1—The accumulation from little particles. The generation of heat by short-living radioactive elements is not taken into account: ε = 0.001 for growing core and ε = 0.001 for mantle. 2 and 3—The generation of heat by short-living radioactive elements is taken into account: 2—ε = 0.3 for growing core and ε = 0.02 for mantle and 3—ε = 0.4 for growing core and ε = 0.01 for mantle. 4—ε = 04 for growing core and ε = 0.02 for mantle and 5—ε = 0.5 for growing core and ε = 0.05 for mantle. 6—The dependence of the core's melting temperature from pressure.

Here ρ is the density of the medium, $\vec{V}$ the volume velocity of the flow, P the pressure, μ the kinematic viscosity of the medium, $\vec{\Omega}$ the angular velocity of diurnal rotation, W the potential of the rotating body, T the medium temperature at a given point and time, Q_1 the normalized cumulative power of the release of the specific internal energy, and χ the thermal diffusivity.

Using the Boussinesq approximation for "incompressible fluid" greatly simplifies the consideration of Eqs. ((2)–(4)) [15, 16]. In the energy balance equation, adiabatic heating and energy release of radioactive sources Q_1 are taken into account here, but the contribution of energy dissipation of viscous friction was not taken into account:

$$k\rho \frac{\gamma M}{r} \frac{dr}{dt} = \varepsilon\sigma\left[T^4 - T_1^4\right] + \rho c_P\left[T - T_1\right] \frac{dr}{dt} \tag{5}$$

The system of Eqs. ((1)–(5)) in the spherical sector is solved numerically, and the conditions of periodicity are given on the lateral boundaries, while the conditions (Eq. (5)) are calculated on the outer surface of the growing radius [12].

where ρ is the density of the medium; γ is the gravitational constant; M is the mass of the growing planet; r is its radius; T and T_1 are, respectively, the surface temperature of the body and the external medium; ε is the permeability coefficient and c_p the specific heat; and k is the fraction of the conversion of the potential energy into thermal energy.

The results of the work by [12] show various options for estimating the temperature of the interior regions of the planet by the time of completing its accumulation for numerical models that take into account the difference in transmission ε from the boundary conditions (Eq. (5))

of thermal radiation, depending on its composition and density. As can be seen from the results presented in **Figure 5**, the temperature of the growing surface sharply decreases as the transparency of the atmosphere increases, due to the increase of the gravitational radius of the protoplanet and the possibility of retaining the silicate content of the cloud.

In the work of [12–14], it was shown that successively changing with the growth of the emerging Earth and the Moon, the main contribution of heat generation in the inner regions of growing bodies is provided first by radioactive sources and, after that, heated from above by the arrival of kinetic energy during a collision with the growing Earth and the Moon. At all stages of the Earth's formation, convective heat and mass transfer is the most important factor in the dynamics of the planet. For the numerical solution of the boundary value problem (Eqs. (1)–(5)), the through-count method proposed in [15, 16] was used. However the one-dimensional model of the thermal structure of the interior regions does not allow one to understand the occurrence of the largest surface structures of continents and oceans.

2.2. New results of 3D modeling of the early stage formation of the Earth-Moon system

In addition, the release of heat due to friction in the viscous melt of the inner envelopes has either not been taken into account at all or has been taken into account only in the already formed envelopes of a planet of constant radius. In this chapter, the first results of numerical modeling of the thermal evolution of the 3D spherical segment of a protoplanet of an increasing radius are considered, taking into account the accidental falling of bodies and particles. In **Figure 6**, the nonuniform temperature distribution on the surface of the growing proto-Earth at a radius of 100 km is shown.

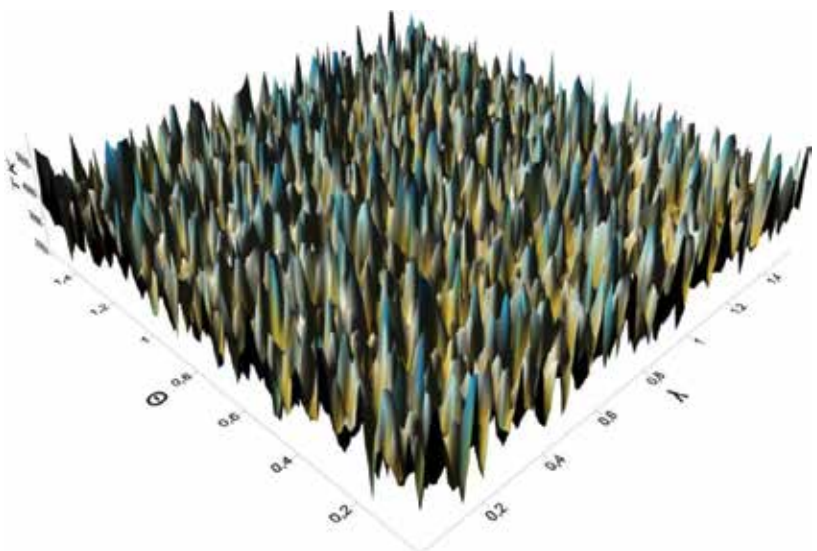

Figure 6. The variant of temperature distribution, stipulated by the random distribution of the accumulated bodies by their values and kinetic energy on the planet's surface at the radius R = 100 km, λ and θ-spherical angles in radians. After 100 km was inserted a comma.

In **Figures 7–9**, the temperature distributions in the inner areas Earth are presented in the form of cross sections of spherical sectors.

In Ref. [13] proposed an algorithm for numerical solution of the problem with allowance for the dissipation of tidal energy in the Earth-Moon system at the stage of planet accumulation. The results obtained showed that the contribution of this source of heat could at times be very significant.

In Ref. [12] showed that the energy release during the decay of short-living radioactive elements in small area, over 50 km in size, is sufficient for the temperature inside such a pre-planetary body to become larger than the melting temperature of iron. This ensures the realization of the process of matter density differentiation and the development of convection in the interior regions of the growing planet. As the Earth grew, the forming area of the outer core remained in the molten state. The use of the 3D model in solving the system of Eqs. ((2)–(4)) with the boundary condition (Eq. (5)) at the stage of formation of the Earth and the Moon made it possible to trace the occurrence and development of thermal heterogeneities in the growing internal areas of the Earth. Similar results were obtained also for the Moon. As can be seen from the results presented in **Figures 7** and **8**, formed due to a random distribution of falling bodies on the forming planet, near-surface thermal heterogeneities do not have time to homogenize and cause a complex structure of distribution of concentration and thermal heterogeneities. However, the Earth and the Moon form a tight double system. Therefore, the thermal evolution of these bodies at the accumulation stage must be analyzed together. The need to take into account the release of heat due to the attenuation of tides during the accumulation of the Earth was noted in the work of [17, 18]. For the mathematical description of the thermal evolution of proto-Earth and proto-Moon growing in the process of accumulation as a close binary system, it is necessary to take into account the evolution of the Moon's orbit due to the tidal interaction and the dissipation of viscous fluid friction energy excited by this tidal interaction.

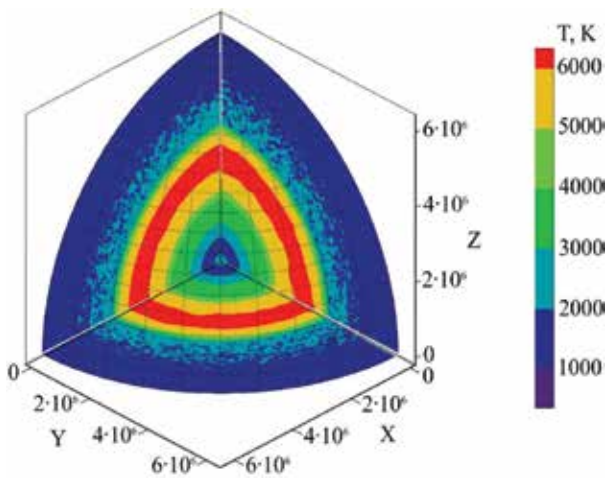

Figure 7. An example of the temperature distribution and initial thermal heterogeneities in the protoplanet up to the end of its accumulation, without taking into account the heat of tidal friction.

http://dx.doi.org/10.5772/intechopen.72641

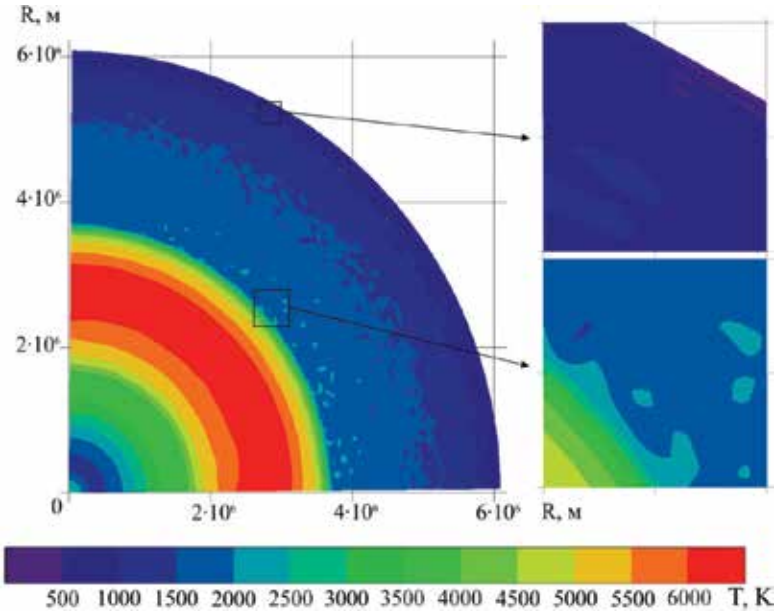

Figure 8. The temperature distribution of the Earth's interior to the end of accumulation along the section of the 3D sector (without taking into account the heat dissipation energy of tidal friction).

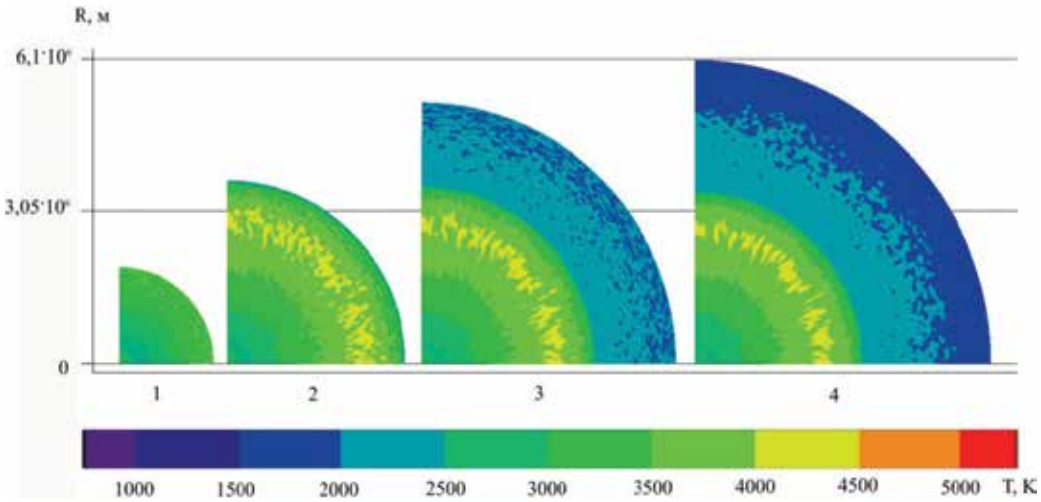

Figure 9. The temperature distribution in the inner areas of the proto-Earth for various values of the achieved radius: 1-R = 1930 km, 2-R = 3670 km, 3-R = 5220 km, and 4-R = 6680 km.

In contrast to the model, for which the Businesque approximation—an incompressible viscous fluid—is still applicable, we can no longer use the incompressibility approximation in Eqs. (2) and (4). In the model under consideration, the tidal interaction between the Sun and the planets will be neglected, which will allow us to use the results of an analysis of the close

binary system. For the Earth-Moon system, one can use the approximation for the law of conservation of momentum in the form (Eq. (6)) [17], (**Figure 10**). It does not take into account the interaction with the Sun, which ensures the solar tide:

$$I\,\Omega + \frac{M_1 \cdot m_1}{M_1 + m_1} L^2\,\omega \;=\; const \tag{6}$$

where I is the inertial moment of the growing Earth, $\Omega(t)$ is the angular velocity of its rotation about its own axis at time t, $\omega(t)$ is the angular velocity of the orbital motion of the Moon around the Earth for the same moment of time, M_1 is the mass of the proto-Earth for the time moment (t), m_1 is the proto-Moon mass at the same time moment (t), and $L(t)$ is the distance between the centers of mass of the Earth and the Moon.

For the energy of the Earth's own motion and the total energy of the Moon's orbital motion, one can use the expressions (Eq. (7)):

$$E_\Omega \;=\; I\frac{\Omega^2}{2} \quad E_\omega \;=\; -\gamma\frac{M_1(t)\,m_1(t)}{2L} \tag{7}$$

To describe the dynamics of the Earth-Moon system, it is necessary to replace Eq. (3) by Eq. (8):

$$\rho c\left(\frac{\partial T}{\partial t} + \vec{V}(\nabla T)\right) \;=\; \lambda\Delta T + Q_1 + \Phi \tag{8}$$

where Φ is the dissipative function in each of the melt regions, as can be seen from the results of the simpler model, shown in **Figures 7** and **8** for each time point. The function Φ describing the energy dissipation in a viscous fluid in a Cartesian coordinate system has the form [19, 20]:

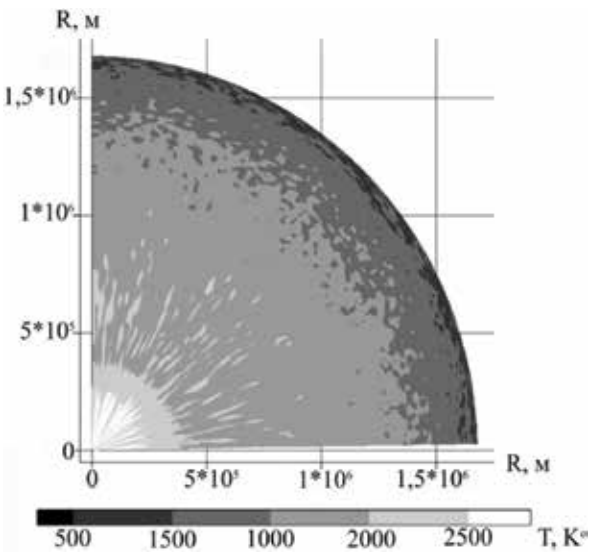

Figure 10. Temperature distribution in the interior areas of the Moon up to the completion of its accumulation.

$$\Phi = 2\mu\left[\left(\frac{\partial u_x}{\partial x}\right)^2\left(\frac{\partial u_y}{\partial y}\right)^2+\left(\frac{\partial u_z}{\partial z}\right)^2+\frac{1}{2}\left(\frac{\partial u_x}{\partial y}+\frac{\partial u_y}{\partial x}\right)^2+\frac{1}{2}\left(\frac{\partial u_y}{\partial z}+\frac{\partial u_z}{\partial y}\right)^2+\frac{1}{2}\left(\frac{\partial u_z}{\partial x}+\frac{\partial u_x}{\partial z}\right)^2\right]+\lambda\left|\frac{\partial u_x}{\partial x}+\frac{\partial u_y}{\partial y}+\frac{\partial u_z}{\partial z}\right|^2 \quad (9)$$

where μ and λ are the coefficients of the first and second viscosities: u_x, u_y, and u_z are the projections of the velocity in Cartesian coordinates.

The algorithm for solving this nonlinear system of equations is as follows. For each moment of time, using Eq. (1), new values of the Earth's and Moon's masses and the time step are found at a fixed step along the coordinate r. New boundary conditions for the proto-Earth and like for the proto-Moon are calculated (Eq. (5)). A direct problem is solved in the body of the increased radius, for which the temperature, velocity, and pressure fields are used as the initial conditions from the previous time step (Eqs. (2), (8), (4)), respectively. New distributions of the melting temperature and the function Φ in (Eq. (9)) are computed from the new temperature and pressure distribution. Since the system of equations is nonlinear, the solution is sought using the iteration method, which provides a given relative error. The number of iterations is carried out until the specified accuracy of the solution is achieved. Then the system (Eqs. (6) and (7)) is solved, and new parameters of the satellite orbit are determined. After this, the next step is taken along the spatial grid. But the solution of this nonlinear boundary value problem with the necessary number of iterations at each time step and the necessity of calculating the dissipative function (Eq. (8)) requires very large computational powers. In this case, there are very rough estimates of the viscosity dependences on temperature and pressure, which lead to computational difficulties. Therefore, we confine ourselves to an estimate that can be obtained using the phenomenological approach and using the Q-factor approximation of the interior regions of the Earth and the Moon, based on the results of [17, 18]. We use the quality factor as the fraction of the energy E dissipating into heat during one oscillation period (Eq. (10)):

$$Q^{-1} = \frac{\delta E}{2\pi E} \quad (10)$$

This function is estimated by modern seismic results on the attenuation of the Earth's natural oscillations for the model hydrostatic pressure and available estimates of the current temperature [18].

Tidal interaction redistributes the moments of momentum between the bodies forming a closed system, and its modern value is a well-known value. On the contrary, the total amount of energy in the open system Earth-Moon is not conserved. The value of the rotational energy is not conserved but partially dissipates into heat, and this part of it must be taken into account as a source term in Eq. (8).

3. Conclusions

Newton's law, with sufficient accuracy, described the gravitational interaction of material bodies on the scales of individual stars and their planetary systems. It is not applicable to describing processes in the universe as a whole. In this case, it is already necessary to use the general theory of relativity and the law of gravitational interaction of Einstein.

To simulate the conditions for the evolution of the protoplanetary solar disk, the law of gravitation in the Newton approximation is quite sufficient. The obtained numerical results of the solution of the boundary value problem in the body of the increasing radius of the system of nonlinear equations for modeling the thermal conditions for the formation of the Earth and the Moon in one-dimensional and three-dimensional models were analyzed. It is shown that effects can be revealed in the three-dimensional model of the numerical solution of the problem, which could not be detected in a spherically symmetric model, and they significantly influence on the dynamical evolution of the binary system Earth-Moon.

As the mass increases, the distance between their centers of mass and the speed of the orbital rotation of the Moon around the Earth change. From the law of conservation of angular momentum (Eq. (6)), it follows that the tidal interaction as the mass of the central body increases provides the transfer of the orbital angular momentum of the satellite to the central massive body. At the same time, part of the rotational energy was converted into thermal energy due to viscous friction. Losing the orbital moment, the satellite should approach the central body right up to the orbit of Rosh. The problem of the behavior of the satellite at the Rosh limit requires a careful mathematical study. The power of additional thermal energy and the volume of molten inclusions should increase with the growth of the Earth. Due to the continued transfer of the satellite's orbital moment to the central body, its own angular velocity continued to grow. This should lead to an increase in the orbital angular velocity of the satellite and an increase in the radius of its orbit, which is observed up to the present time.

Thus, the effect of dissipation of viscous friction most significantly manifests itself at the initial stage of the formation of the Earth. The results obtained depend on the parameters, primarily the viscosity versus temperature and pressure, the values of which are known with a high degree of uncertainty. They are to be verified from the results of further research in the areas of physical-mathematical and geological exploration.

Acknowledgements

The work was carried out with the RFBR grant No. 16-05-00540.

Author details

Yurie Khachay, Olga Hachay* and Alexander Antipin

*Address all correspondence to: olgakhachay@yandex.ru

Institute of Geophysics UB RAS, Ekaterinburg, Russian Federation

References

[1] Einstein A. Die Grundlage der allgemeinen Relativitätstheorie. Annalen der Physik. 1916;**354**(7):769-822

[2] Friedman A. Über die Krümmung des. Raumes. Zeitschrift fur Physik. 1922;**10**:377-386

[3] Hubble E. The relationship between the distance and the radial velocity of extragalactic nebulae. In: Proceedings of the USA National Academy of Sciences. 1929;**15**(3):168-173

[4] Penzias A. The origin of the Elements. 1979;**129**:581-593

[5] Jacobsen S. The Hf-W isotopic system and the origin of the Earth and Moon. Annual Review of Earth and Planetary Sciences. 2005;**33**:531-570

[6] Krot A, Amelin Y, Bland P, Ciesla F, Connelly J, et al. Origin and chronology of chondritic components: A review. Geokhimica et Cosmokhimica Acta. 2009;**73**:4963-4997

[7] Nyquist L, Kleine T, Shih C-Y, Reese Y. The distribution of short-living radioisotopes in the early solar system and the chronology of asteroid accretion, differentiation, and secondary mineralization. Geokhimica et Cosmokhimica Acta. 2009;**73**:5115-5136

[8] Safronov V. Evolution of the Protoplanetary Cloud and Formation of the Earth and the Planets. Moscow: Nauka; 1969; 168 p (in Russian)

[9] Maeva S. About the thermal history of the Earth. Izvestija AN USSR. Physika Zemli. 1967;**3**:3-17 (in Russian)

[10] Lubimova E. Thermal Earth and Moon. Moscow: Nauka; 1968. 280 p (in Russian)

[11] Anfilogov V, Khachay Y. A possible scenario of material differentiation at initial stage of the earth formation. Doclady Earth Siences. 2005;**403A**:954-947 (in Russian)

[12] Anfilogov V, Khachay Y. Some aspects of the solar system formation. Briefs of the Earth Sciences. Cham, Heidelberg, New York, Dordrecht, London: Springer; 2015. 75p

[13] Khachay Y, Hachay O, Antipin A. Heat production by the viscous dissipation of energy at the stage of accumulation of the earth. Geoinformatika. 2017;**4**:5-9

[14] Pechernikova G, Vitjasev A. Catastrophic influences of cosmic bodies. Moscow: IKZ Akadembook; 2005. pp. 251-265 (in Russian)

[15] Samarskiy A, Moiseenko B. The economic scheme of transparent account of Stefan problem. Journal of Computational Mathematics and Mathematical Physics. 1965; **5**(5):816-827 (in Russian)

[16] Tikhonov A, Lubimova E, Vlasov V. About the evolution of melting zones in the Earth's thermal history. Dokladi AN USSR. 1969;**188**(2):338-341 (in Russian)

[17] Ruskol E. Origin of the Moon. Moscow: Nauka; 1975. 188 p. (in Russian)

[18] Zharkov V, Trubitsin V. Physics of the Planetary Interior. Moscow: Nauka; 1980. 448 p. (in Russian)

[19] Landau L, Lifshitz E. Theoretical physics. Hydrodynamics. 3rd ed. Main edition of phys-math literature. Moscow: Nauka; 1986. 736 p. (in Russian)

[20] Schubert G, Turcotte D, Olson P. Mantle Convection in the Earth and Planets. Melburn, Australia, Madrid, Spain, Cape Town, South Africa: Cambridge University Press; 2001. 940 p

Section 4

Electrical Resistivity Surveying

Chapter 8

Geoelectrical Sounding and Imaging over the Central Zone of Panama

Alexis Mojica

Additional information is available at the end of the chapter

http://dx.doi.org/10.5772/intechopen.74210

Abstract

Electrical properties of rocks and geoelectrical resistivity method have been discussed in this chapter, in which the results of an electrical survey over the sedimentary terrain of the central zone of Panama (Central America) are presented. This study therefore includes (i) a petrophysical study with the aim of relating its electrical resistivity values with the volumetric water contents, (ii) an electrical resistivity imaging (2D inversion), and (iii) an electrical sounding (1D inversion) for detecting the water table and its corresponding stratigraphy and variation with time. Two datasets for these last methods have been developed with the aim of monitoring the percentage changes in model resistivity. Petrophysical tests show good fits between resistivity and volumetric water content and known parameters for rocks and soils. 1D and 2D inversions show a significant reliability with the stratigraphic information obtained from a borehole and strong changes caused by rainy season in this tropical zone.

Keywords: electrical sounding, electrical resistivity imaging, petrophysical, sedimentary rocks, geophysical inversion, time-lapse imaging

1. Introduction

In geophysical studies, resistivity method can be used in fault zone detection and stratigraphic characterization, in hydrology for tracing water transport during a given period of irrigation studies, and for archeological and agriculture purposes. Resistivity is controlled by water content, soil texture and its geochemical properties, lithology, organic matter content, and thermodynamic parameters. The electrical properties of the materials that make up part of the outermost layers of the crust can be studied either electrically or electromagnetically from the response produced by the flow of electrical current in the subsurface. Geoelectrical methods

take into account these electrical and electromagnetic aspects whose physical parameters, such as electrical current, electrical potential, and electromagnetic fields can be measured naturally or artificially. In 1830 a self-potential method based on the natural electrical response of the subsurface was used [1]. In his work, low-intensity electrical currents generated by some minerals were identified. Later, this methodology underwent certain changes in terms of using a natural source, and Schlumberger, during the second decade of the last century, decided to use artificial sources by injecting electrical current into the subsoil.

The electrical resistivity of rocks is a physical property that is characterized by very large variations in their values; most rocks and soil can be classified as highly resistive or insulating, and only metallic minerals and some of their salts can be classified as conductors. There are three ways in which electrical current can propagate through the subsurface: ohmic or electronic, electrolytic, and dielectric. The first is related to normal type of flow of charges through materials with free electrons such as metals; for electrolytic conduction, almost all soils and rocks have pores that could be saturated with water; thus, for those types of soils and rocks that have high ranges of electrical resistivity, the circulation of electrical current is carried out exclusively through electrolytic conduction due to the presence of water contained in the pores and fissures of the material. This means that the value of the electrical resistivity depends on the concentration and degree of dissociation and mobility of ions [2]. Electrolytic conduction is produced by the slow movement of the ions within the electrolyte; therefore, the rocks are electrolytic conductors where the flow of electrical charge occurs through the conduction of ions. Dielectric conduction occurs only in materials with high electrical resistivity (insulators). According to [3], in this class of materials, the electrons can experience a slight displacement with respect to their atomic nucleus in the presence of a variable external electric field.

Geoelectrical methods include a wide variety of techniques that are adapted to the objectives of the investigation, the dimensions and topography of the area of interest, and the electrical properties of the soil and rocks that make up the study area and whether these properties undergo large variations. Techniques such as self-potential, telluric and magnetotellurics, electrical resistivity (which we will deal with in more detail in this chapter), electromagnetism, and induced polarization allow a rapid measurement of the electrical properties of the soil, such as electrical resistivity, or its opposite, electrical conductivity. These noninvasive techniques essentially involve the interpretation of these physical parameters of the soil, which quantify the degree of difficulty or ease in which a certain volume of soil responds to the passing of electric charges, respectively; for more details about these methods, see [1, 3–7].

The electrical resistivity method is one of the most common geoelectrical methods for the prior evaluation of soil in civil, environmental, archeological, geological, and agricultural projects. Its noninvasive nature and the rapid data acquisition make this method an inexpensive and effective tool in the detailed evaluation of soil. Then, the determination of the geochemical and geophysical properties of soil is essential to the development of civil and agricultural engineering projects. In archeology, for example, the resistivity method constitutes an additional tool of remarkable value when evaluating in advance the presence and/or absence of buried archeological features, thus optimizing resources and time spent in the field, with significant economic impact. Conventional methods of soil analysis directly affect the soil because the samples must be taken and analyzed in a laboratory.

http://dx.doi.org/10.5772/intechopen.74210

Geoelectrical methods have been used extensively in groundwater studies and stratigraphic characterization. Several authors have carried out studies of samples in the laboratory using petrophysical relationships [8] in which the volumetric water content is obtained by the measurement of dry bulk density and the gravimetric water content, for example, see [9, 10] in leachate recirculation studies, [11, 12] for root-zone moisture interactions and watershed characterization, and [13] in rainfall simulations.

This chapter gives a short description of electrical properties of rocks, basic principles of the geoelectrical resistivity method, and a case study of sedimentary rocks of central zone of Panama (Central America) that include petrophysical soil analysis and 1D and 2D inversion methodology. This study has been developed with the aim: (i) to obtain a relationship between electrical resistivity with volumetric water content and correlation with the empirical equation of Archie's law and (ii) to define a 1D and 2D electrical models for two datasets obtained in different seasons (dry and rainy) and relate the results to the stratigraphy and in addition monitor the percentage changes of calculated resistivity values.

2. Study area and geology

The study area is located in an open test zone of the extension of the Technological University of Panama, 19 km East-Northeast of Panama City in the central zone of Isthmus of Panama, Central America; see **Figure 1(a)**. Panama has a rainy and dry seasons, with a tropical maritime

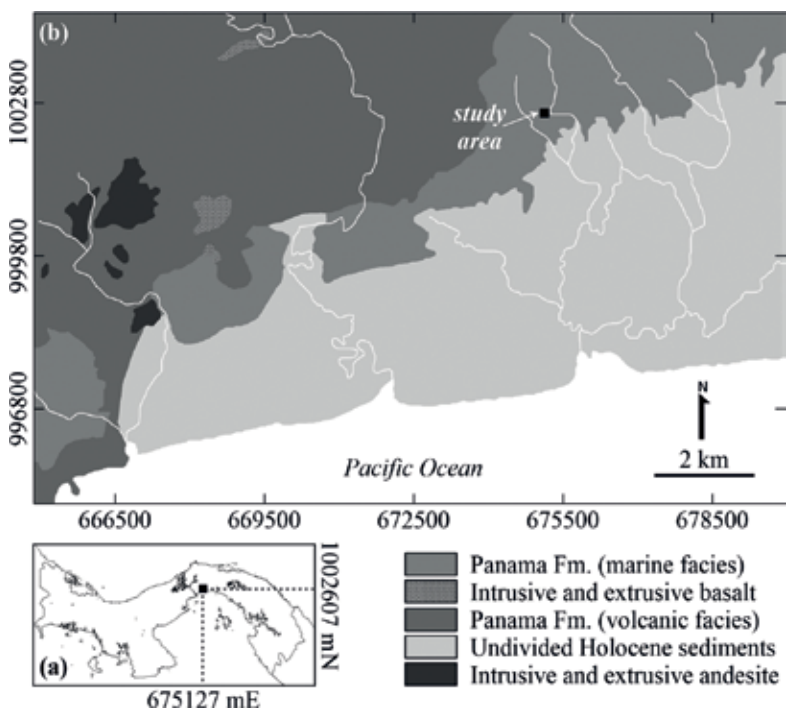

Figure 1. (a) Location map and (b) geological setting of study area and environs [18].

climate with a hot, humid, rainy season (May → December) and a short dry season (January → May). According to [14] the transition at the end of the dry season to the beginning of rainy season is linked with the disappearance of trade winds.

According to [15–18], the study area is characterized by a dense sequence of sediments and volcanic rocks. The site is influenced by the geological elements of the Panama Formation (marine facies) of early to late Oligocene; these elements consist of tuffaceous sandstone, tuffaceous siltstone, and algal and foraminiferal limestone [18]. **Figure 1(b)** shows the geological map and study area and environs.

3. Methodology

3.1. Site layout and profile

To obtain a distribution of electrical resistivity values in lateral and vertical directions, and its variations for a period of three and half months, we have defined a North-South profile of 47 m long; this profile is superimposed on a borehole drilled in 2011 with a piezometer to monitor groundwater dynamics linked with dry and wet seasons. **Figure 2(a)** and **(b)** show the area with profile, electrical sounding, and borehole positions and **Figure 2(c)** a geotechnical scheme of the borehole.

3.2. Petrophysical relationship

A total of five soil samples were collected from the site to a depth of 20 cm. To obtain a relationship between resistivity and volumetric water content, we have used the ASTM standard G57-06, where the samples are homogenized inside a box of insulating materials as shown in **Figure 3**.

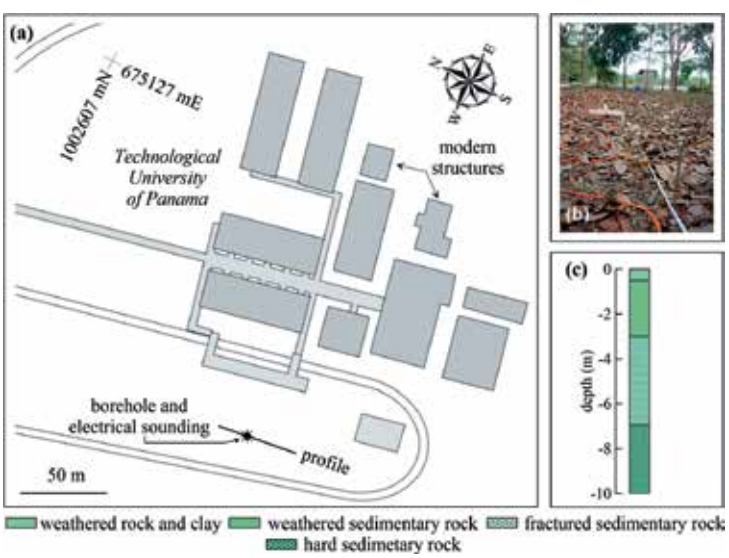

Figure 2. (a) Details of the study area with North-South profile and electrical sounding and borehole location, (b) panoramic of the field site, and (c) description of borehole log.

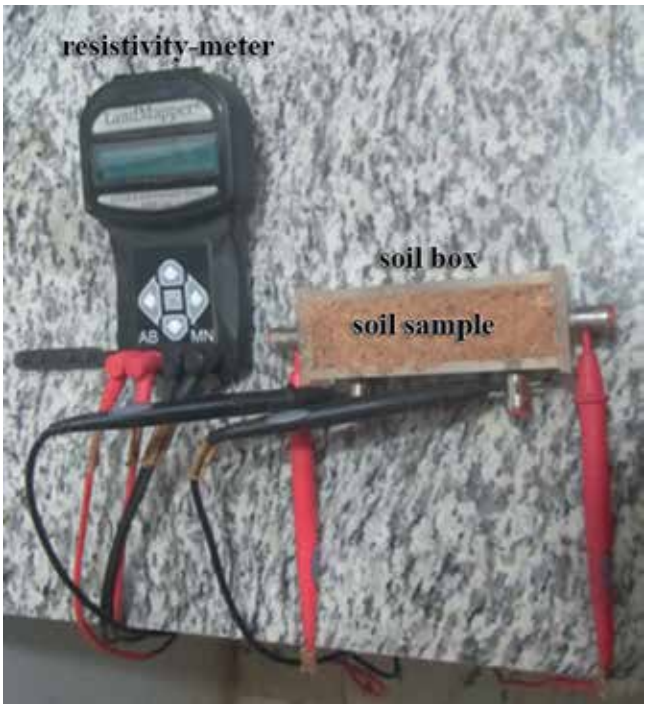

Figure 3. LandMapper of Landviser and Miller soil box used for the measurement of the electrical resistivity of each soil sample in laboratory, according to ASTM standard G57-06 (photo courtesy of 3P Soc. Ltda).

In this box, two metal plates with an equal surface (S) are placed; we connected these plates to the source of electrical current or resistivity meter; see **Figure 3**. On the surface of the soil sample, two metal pins are inserted and separated by distance (l) to measure the voltage generated when the electric current passes through this sample. The value of electrical resistivity (ϱ) of the soil sample is given by:

$$\rho = RS/l \tag{1}$$

where R is the electrical resistance (in Ω). Volumetric water content (θ) and dry bulk density were obtained by weight difference (dried at 105°C for 24 hours) and calculating the gravimetric water content. The relationship between ϱ-θ of these samples can be demonstrated and then fit it into Archie's law [8]:

$$\rho = a\rho_w \Phi^{-m} S_a^{-n} \tag{2}$$

where a is the tortuosity factor, ρ_w is the electrical resistivity of the fluid filling the pores, Φ is the porosity (volume of void-space/bulk volume of the soil), S_a is the saturation of the sample (volume of fluid/volume of void-space), and m and n correspond to the cementation and saturation exponents of the rock, respectively. Under certain special conditions, it is possible to approximate these last parameters and to obtain the volumetric water content from Φ and S_a.

3.3. Electrical sounding and 2D electrical resistivity imaging acquisition and processing

The electrical resistivity methods generate three-dimensional patterns of electric current and electric potential flows within the subsurface [19]. In the case of two electrodes inserted in the surface of a homogeneous and isotropic half soil and separated by a short distance, it is possible to see a symmetrical pattern in the equipotential lines and in the electric flow lines; this means that at any point in the vicinity of the system, the electrical potential can be affected by the current electrodes (*A* and *B*). In situ, the voltage (ΔV) between two points (*M* and *N*) due to the two electrical sources is measured, and the electrical resistivity value is given by:

$$\rho = k \Delta V / i \tag{3}$$

where *k* corresponds to geometrical factor, which only depends on electrode position and *i* the electrical current.

In the case of an inhomogeneous medium, the measurements of the electrical resistivity of the subsurface tend to change when the set of four electrodes or quadrupole is moved along a profile. Another important aspect is that the value of electrical resistivity defined in the last equation will depend on the geometrical configuration of the electrodes and not on the intensity of the electric current. Therefore, the value obtained in this equation will correspond to a kind of average values of resistivity of the subsurface, from which we get the apparent electrical resistivity (ρ_a). It is important to note that the value of the apparent electrical resistivity of the soil will be its real value only if the soil is homogeneous. In practice there are different types of quadrupole arrays whose use will depend on the objectives of the research. Each of them is characterized by different geometric constants (*k*); **Figure 4** presents the most common arrangements used in soil exploration.

For each of the linear arrays of **Figure 4**, the record of the apparent electrical resistivity value of the subsoil is taken at the center of the internal electrodes; the measurement point is located at the center of the four electrodes. These quadrupole arrays allow the development of several modalities which are closely related to the objectives of the research. In this work we used the electrical sounding and 2D electrical resistivity imaging. The first method consists of keeping the position of the potential electrodes fixed (1 m apart for this study) and moving the current electrodes by 1 m. This procedure, illustrated in **Figure 5(a)**, allows defining a tabular model of the subsurface based on the geometrical distribution of the strata that have different electrical properties.

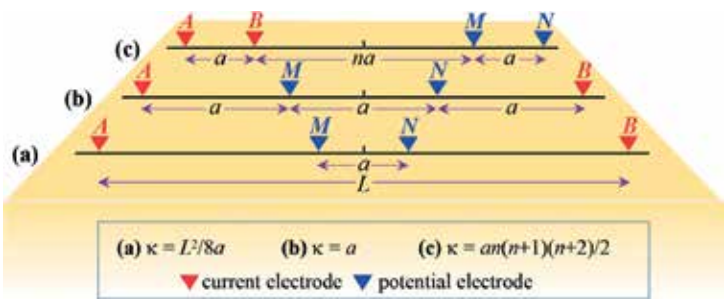

Figure 4. Some common quadrupole arrays: (a) Schlumberger, (b) Wenner, and (c) dipole–dipole and geometric constant.

http://dx.doi.org/10.5772/intechopen.74210

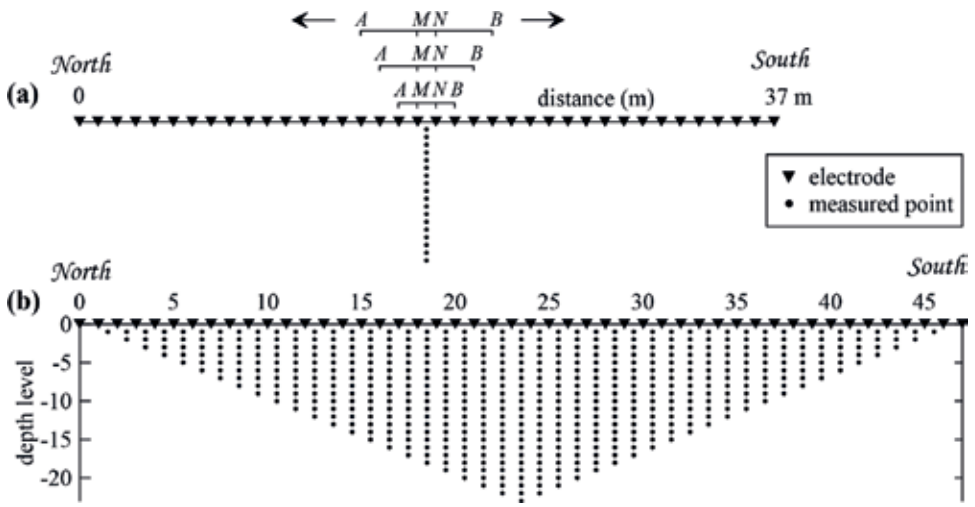

Figure 5. Distribution of apparent electrical resistivity data points for (a) the electrical sounding with a Schlumberger array and (b) a pseudo-section for imaging analysis with a Wenner-Schlumberger array.

The apparent resistivity value corresponding to each distance AB/2 is plotted logarithmically, resulting in a curvilinear tendency and, subsequently, with the resolution of the 1D inverse problem. This dataset is fitted to a curve that obeys the number of layers with their respective values of calculated electrical resistivity and thickness. The aim of inverse problem is to reconstruct a model from apparent electrical resistivity values. Two resistivity datasets were collected using a Schlumberger electrode configuration on the 16th of February, 2012, and 31st of May, 2012.

The second method consists of obtaining a high-resolution 2D image of the distribution of the electrical resistivity both laterally and vertically. The process consists of obtaining a set of apparent electrical resistivity values through a finite number of electrodes aligned along a profile with a constant distance between them (1 m for this study). The data can be obtained by varying the distances between the pairs of transmitter-receiver electrodes by multiples of a value with a computer-controlled multielectrode system. **Figure 5(b)** shows the electrode location along the profile and the measured points.

Measurements (for electrical sounding and 2D electrical resistivity imaging) were performed with a Syscal R1 Switch-48 (IRIS Instruments), in a simple mode for the first and a multielectrode mode for the second. In respect of the acquisition setting, the maximum value allowed standard deviation of the measurement was fixed at 1%; minimum and maximum number of stacks per measurement and the current time per cycle were fixed at 3 and 6 and 500 ms, respectively. To obtain a realistic 2D image of electrical resistivity distribution in the soil, we used a cell-based inversion method; this method subdivided the subsurface into a number of rectangular cells whose positions and sizes can be fixed [20]. The aim is to use an inversion algorithm to calculate the electrical resistivity of the cells that provides a model response that agrees with the apparent electrical resistivity values obtained in the field. In this study we used the regularized least-square optimization method [20–22]. This optimization method has two different constraints: the smoothness-constrained method [21] and the robust method [23]; the first is used when the subsurface exhibits a smooth variation in resistivity distribution and the second in regions that are piecewise constant and separated by sharp boundaries [20, 24].

As in the electrical sounding, two resistivity datasets were collected using a Wenner-Schlumberger array for the electrical resistivity imaging on the 16th of February, 2012, and 31st of May, 2012.

3.4. Time-lapse inversion

To monitor the changes in subsurface resistivity values during the period defined in the study area, we used the Res2Dinv inversion software (Geotomo); the time-lapse dataset can be interpreted through the time-lapse method proposed by [25]. In this software, the initial dataset for the inversion model is used as a reference model in the inversion of the later time-lapse datasets [26]. For our first dataset, we used the robust method; regarding another inversion parameter, we used an initial damping factor of 0.15, minimum damping factor = 0.030, and a simultaneous inversion.

4. Results and interpretation

4.1. Resistivity: volumetric water content derived from soil samples

Figure 6 presents a plot of electrical resistivity versus the volumetric water content of the soil samples obtained in the surveyed area. The fit was done using a power function with a good coefficient of determination, R^2 of 0.950; high values of resistivity of this type of soil (weathered rock) can be linked to 26% of volumetric water content, while the low values of electrical resistivity of the samples are related to 49% of water content.

4.2. Electrical sounding

Figure 7(a) represents the two datasets obtained with a Schlumberger array in the given periods; subsequently, with the resolution of the inverse problem 1D, these datasets were fitted to a curve (for each one) that obeys the number of layers with their respective values

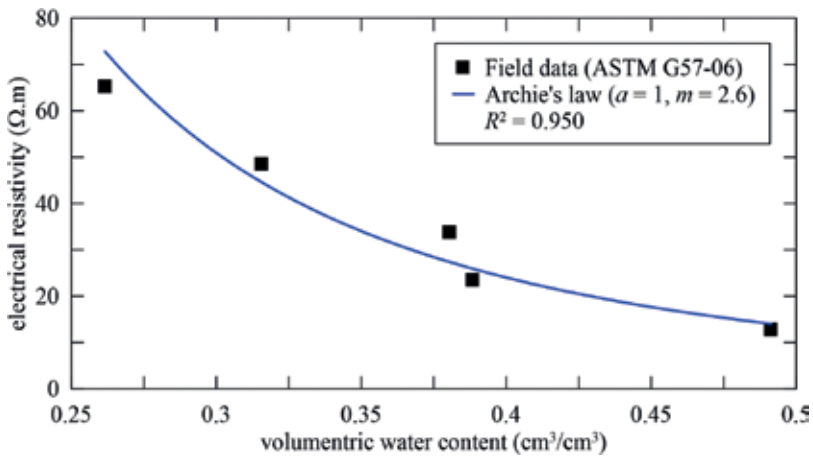

Figure 6. Relationship between the electrical resistivity and the volumetric water content obtained in the surveyed area.

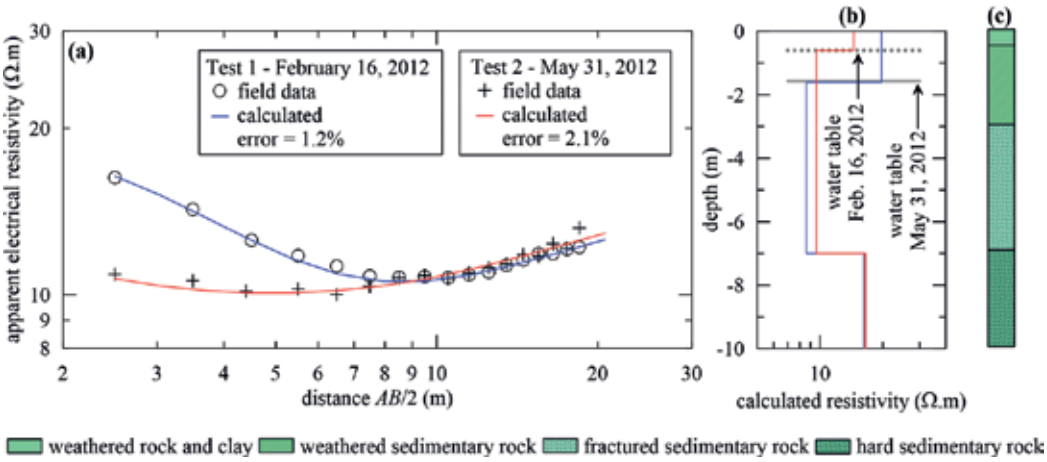

Figure 7. (a) Logarithmic representation of the two datasets as a function of distance AB/2, (b) tabular earth model obtained from the inversion, and (c) borehole performed on site.

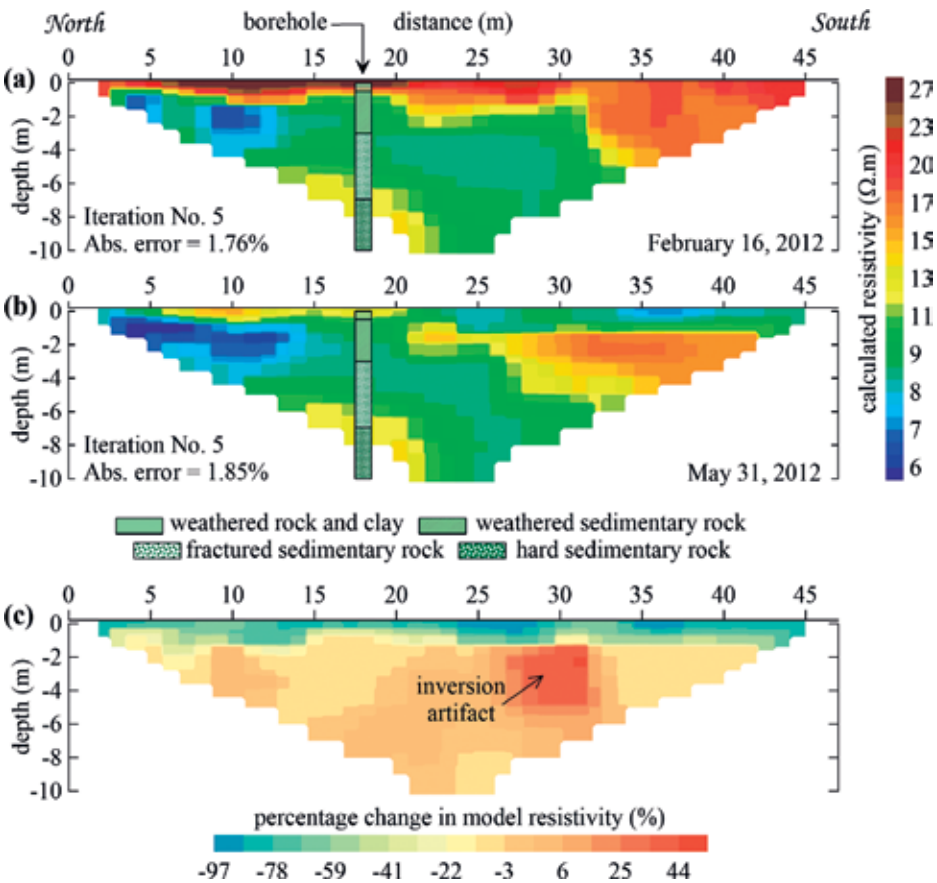

Figure 8. Electrical resistivity tomography obtained for a (a) reference test – February 16, 2012 – and (b) second test, May 31, 2102. (c) Percentage changes in model resistivity obtained in this study.

of calculated electrical resistivity and thickness. After solving the inverse problem for each dataset, the errors obtained were not greater than 2.1%. **Figure 7(b)** shows a three-layer model for each test.

In both cases, the resolution of the inverse problem suggests the existence of a first layer of 14.5–19.7 Ω.m and a variation of thickness from 0.6 m to 1.6; this effect is linked to the change from dry to rainy season. Water-table elevation obtained from a piezometer has shown variation between 1.57 and 0.61 m for each date, followed by a second layer of 8.9 and 9.6 Ω.m and 5.4 and 6.4 m thick for each season, respectively. Finally, there is a last layer with 16.2 and 16.5 Ω.m; the results of this last layer do not show significant changes in their electrical properties and thicknesses. In accordance with the borehole at the site, the two first layers are linked to weathered and fractured sedimentary rock, while the last layer reported for both analyses is linked to hard sedimentary rock.

4.3. Electrical resistivity imaging and time-lapse results

Figure 8(a) and **(b)** show the results of inverse problem solution; in these electrical tomographies, it is possible to identify a first horizon related to weathered rocks and clay (13–27 Ω.m) with tones in brown, red, and yellow. The changes in calculated resistivity values are related to the beginning of rainy season; saturation of surface horizons can produce a decrease in calculated resistivity value. At depth, it is possible to identify a low resistivity (6–13 Ω.m) horizon from the result of **Figure 8(a)**. However, these low values are also revealed at shallow depth; see **Figure 8(b)**. About **Figure 8(c)**, high negative percentage changes are linked to increase of water content in subsoil produced by rains which occurred on May 31, 2012. At depth, the percentage changes are close to 0. Positive percentage changes in model resistivity are related to inversion artifacts. It is possible that these unrealistic changes can be linked to the removal electrode after the first test or inversion scheme used in this analysis.

5. Conclusions

The results of this study show the value of petrophysical relationship of soil samples in understanding the potential function between the electrical properties of rocks and its volumetric water content. These functions can help to understand the evolution of vadose zone moisture in response to seasonal changes in the tropics. Electrical sounding and electrical resistivity imaging are useful tools not only for monitoring changes in the physical properties of this kind of soils but also for associating the different types of soils and rocks with its electrical properties. We have seen the association of these results with the borehole at the site. The strong negative percentage variation in calculated resistivity values presented in the surveyed area shows the important seasonal changes occurring in the tropics, where these negative values are related to the superficial infiltration produced by the rainfall during the transitional season (dry → rainy). The positive percentage changes in model resistivity can be associated with artifacts, linked to inversion method used or due to the removal of the electrodes after each test.

Acknowledgements

I am grateful to the Technological University of Panama and National Research System of SENACYT for all their support. I would like to thank the reviewers for their constructive observations.

Conflict of interest

Author discloses no potential conflicts of interest.

Author details

Alexis Mojica[1,2]*

*Address all correspondence to: alexis.mojica@utp.ac.pa

1 Research Laboratory in Engineering and Applied Sciences, CEI, Technological University of Panama, Panama

2 Tocumen Extension and National Research System, SENACYT, Panama

References

[1] Parasnis DS. Principles of Applied Geophysics. 5th ed. London: Chapman & Hall; 1997. 429 p

[2] Nover G. Electrical properties of crustal and mantle rocks – A review of laboratory measurements and their explanation. Surveys in Geophysics. 2005;**26**:593-651. DOI: 10.1007/s10712-005-1759-6

[3] Telford WM, Geldart LP, Sheriff RE. Applied Geophysics. 2nd ed. New York: Cambridge University Press; 1990. 770 p. DOI: 10.1017/CBO9781139167932

[4] Vogelsang D. Environmental Geophysics. A Practical Guide. 1st ed. Germany: Springer-Verlag; 1995. 173 p

[5] Reynolds JM. An Introduction to Applied and Environmental Geophysics. 2nd ed. Chichester: Wiley; 2011. 710 p

[6] Mussett AE, Khan MA. Looking into the Earth. An Introduction to Geological Geophysics. 1st ed. New York: Cambridge University Press; 2000. 470 p. DOI: 10.1017/CBO9780511810305

[7] Lowrie W. Fundamentals of Geophysics. 2nd ed. New York: Cambridge University Press; 2007. 390 p. DOI: 10.1017/CBO9780511807107

[8] Archie GE. The electric resistivity log as an aid in determining some reservoir characteristics. Transactions of AIME. 1942;**146**:54-62. DOI: 10.2118/942054-G

[9] Grellier S, Bouyé JM, Guérin R, Robain H, Skhiri N. Electrical Resistivity Tomography (ERT) applied to moisture measurements in bioreactor: principles, in situ measurements and results. In: International Workshop Hydro-Physico-Mechanics of Landfills; Grenoble. France. March 21-22, 2005. 5 p

[10] Grellier S, Guérin R, Robain H, Bobachev A, Vermeersch F, Tabbagh A. Monitoring of leachate recirculation in a bioreactor landfill by 2-D electrical resistivity imaging. Journal of Environmental & Engineering Geophysics. 2008;**13**:351-359. DOI: 10.2113/JEEG13.4.351

[11] Jayawickreme D, Van Dam RL, Hyndman DW. Subsurface imaging of vegetation, climate, and root-zone moisture interactions. Geophysical Research Letters. 2008;**35**:5. DOI: 1029/2008GL034 690

[12] Miller CR, Routh PS, Brosten TR, McNamara JP. Application of time-lapse ERT imaging to watershed characterization. Geophysics. 2008;**73**:G7-G17. DOI: 10.1190/1.2907156

[13] Carey AM, Paige GB, Carr BJ, Dogan M. Forward modeling to investigate inversion artifacts resulting from time-lapse electrical resistivity tomography during rainfall simulations. Journal of Applied Geophysics. 2007;**145**:39-49. DOI: 10.1016/J.JAPPGEO.2017.08.002

[14] Mojica A, Díaz I, Ho CA, Ogden F, Pinzón R, Fábrega J, Vega D, Hendrickx J. Study of seasonal rainfall infiltration via time-lapse surface electrical resistivity tomography: Case study of Gamboa Area, Panama Canal Watershed. Air, Soil and Water Research. 2013;**6**:131-139. DOI: 10.4137/ASWR.S12306

[15] Jones SM. Geology of Gatun Lake and vicinity. Geological Society of America Bulletin. 1950;**61**:893-920

[16] Terry RA. A geological reconnaissance of Panama California Academy of Sciences. 1956; **23**:1-91

[17] Woodring WP. Geology and paleontology of Canal Zone and adjoining parts of Panama. Washington: United States Department of the Interior; 1973

[18] Stewart RH, Stewart JL, Woodring WP. Geologic Map of Panama Canal and Vicinity, Republic of Panama. Washington, DC: Department of the Interior, United States Geological Survey; 1980

[19] Allred BJ, Groom D, Ehsani MR, Daniels J. Resistivity methods. In: Allred BJ, Daniels JJ, Ehsani MR, editors. Handbook of Agricultural Geophysics. 1st ed. Florida: Taylor & Francis Group; 2008. pp. 85-108

[20] Loke MH, Acworth I, Dahlin T. A comparison of smooth and blocky inversion methods in 2D electrical imaging surveys. Exploration Geophysics. 2003;**34**:182-187. DOI: 10.1071/EG03182

[21] deGroot-Hedlin C, Constable S. Occam's inversion to generate smooth, two-dimensional models from magnetotelluric data. Geophysics. 1990;**55**:1613-1624. DOI: 10.1190/1.1442813

[22] Loke MH, Barker RD. Practical techniques for 3D resistivity surveys and data inversion. Geophysical Prospecting. 1996;**44**:499-523. DOI: 10.1111/j.1365-2478.1996.tb00162.x

[23] Claerbout JF, Muir F. Robust modeling with erratic data. Geophysics. 1973;**38**:826-844. DOI: 10.1190/1.1440378

[24] Ellis RG, Oldenburg DW. Applied geophysical inversion. Geophysical Journal International. 1994;**116**:5-11. DOI: 10.1111/j.1365-246X.1994.tb02122.x

[25] Loke MH. Time-lapse resistivity imaging inversion. In: Proceedings of the of the 5th meeting of the environmental and engineering geophysical society European section. Em1, Budapest; September 1999. DOI: 10.4133/1.2922877

[26] Loke MH. Electrical imaging surveys for environmental and engineering studies. A practical guide to 2-D and 3-D surveys. Penang, Malaysia. 2010. 151 p

Edited by Anthony Okiwelu

This book is focused on different aspects of geophysical research, particularly on modern approach in subsurface imaging, tectonics, geohazard, seismicity, and Earth planetary system. Syntheses of results from regional and local studies combined with new techniques of geophysical data acquisition and interpretation from diverse geological provinces are presented. Some of the chapter explained clearly the geophysical technic that can image local sources in urban and rural settings in Israel. An example of studies on basement tectonics and fault reactivation in North America using integrated geophysical methods is also presented. Two modes of seismicity, one involving rotational seismology and another based on seismic response in Mexico using Hilbert-Huang transform (HHT) as an alternative technique for extracting data that will be useful for the assessment of potential earthquake, are discussed in other sets of chapters. The integration of geoelectric methods in another chapter demonstrated delimitation of the resistivity anomalies caused by different types of hydrocarbon contaminants and rocks in rural, industrial, and urban sites. The results of electrical resistivity method to define 1D and 2D electrical models from two datasets acquired in dry and rainy seasons in Panama (Central America) were used to show the relationship between electrical resistivity and volumetric water content. Petrophysical analyses show good fits between resistivity and volumetric water content and known parameters for rocks and soils. The study on Earth planetary system noted that at all stages of the Earth's formation, convective heat and mass transfer are the most important factors in the dynamics of the planet. The chapter on magnetics shows how remanent magnetization and self-demagnetization complicate the inversion and interpretation of magnetic anomaly with examples from iron deposit in South Australia.

Published in London, UK

IntechOpen

ISBN 978-1-83881-273-7